

Marquette University

e-Publications@Marquette

---

Master's Theses (2009 -)

Dissertations, Theses, and Professional  
Projects

---

## Multiscale Analysis of Soil-Strap Interactions in Mechanically Stabilized Earth Retaining Walls

Max Willingham  
*Marquette University*

Follow this and additional works at: [https://epublications.marquette.edu/theses\\_open](https://epublications.marquette.edu/theses_open)



Part of the [Engineering Commons](#)

---

### Recommended Citation

Willingham, Max, "Multiscale Analysis of Soil-Strap Interactions in Mechanically Stabilized Earth Retaining Walls" (2020). *Master's Theses (2009 -)*. 580.

[https://epublications.marquette.edu/theses\\_open/580](https://epublications.marquette.edu/theses_open/580)

MULTISCALE ANALYSIS OF SOIL-STRAP INTERACTIONS IN MECHANICALLY  
STABILIZED EARTH RETAINING WALLS

by

Maxwell Willingham, B.S.M.E.

A Thesis submitted to the Faculty of the Graduate School,  
Marquette University,  
in Partial Fulfillment of the Requirements for  
the Degree of Master of Science

Milwaukee, Wisconsin

March 2020

ABSTRACT  
MULTISCALE ANALYSIS OF SOIL-STRAP INTERACTIONS IN MECHANICALLY  
STABILIZED EARTH RETAINING WALLS

Maxwell Willingham, B.S.M.E.

Marquette University, 2020

A numerical pullout test was built using the discrete element method (DEM) to model and capture the pullout response of steel reinforcements and soil in mechanically stabilized earth (MSE) walls. Through numerical modeling, microscale phenomena showing aggregate behavior in response to the reinforcement can be used to gain insight into the macroscale structure. The general setup of the simulation is a steel specimen encased in a rectangular apparatus filled with particles. A normal pressure is applied to the top layer of particles while the strap is slowly removed from the box until it reaches a prescribed displacement.

The simulation was created using YADE, an open-source DEM software, which allows for rapid scene construction via scripting. The numerical model uses an iterative approach to step through time while resolving contacts at each step and translating those contacts into forces to ultimately provide updated positions for each body at every time step. For this research, a non-cohesive, elastic-frictional Cundall-Strack contact model was employed to resolve interactions on an individual body basis. Test parameters were largely based on the experimental setup of pullout tests performed by Weldu. Particle packings for the pullout simulation were calibrated to the aggregate used in Weldu's experiments by setting up a simple triaxial compression simulation within YADE to derive the correct microscale particle friction angle such that it produced the proper macroscale behavior.

Using the numerical model, three sets of experiments from Weldu's research were reproduced with particle uniformity coefficients of 1, 2, and 3. Simulations sets were run at various normal pressures and included 400,860 particles at the upper end. The numerical tests resulted in an encouraging degree of correlation to the laboratory experiments, with pullout residuals being as close as 2% different and an average of 14% different. In addition, this thesis discusses some of the microscale data extracted from the simulations, such as force chains and rolling characteristics, and how numerical simulations could be used in the future to help guide pullout testing and MSE wall design.

## ACKNOWLEDGEMENTS

Maxwell Willingham, B.S.M.E.

First, I would like to thank my family for their love and encouragement throughout my life and through my education. Their support has helped keep me motivated and inspired to never look back on this long journey.

I would like to thank my close friends for all the memorable days which helped make the time at Marquette unforgettable. This experience would not have been possible without the support of my friends alongside me every step of the way.

I would like to thank Dr. Jonathan Fleischmann for providing me with the incredible opportunity to continue to study and work alongside of him. His enthusiasm for engineering and life is contagious and pushed me continue developing as a researcher and engineer.

I would like to thank Dr. Philip Voglewede for his incredible support throughout my academic career as an advisor and invaluable mentor. His motivation kept me focused and determined to see my journey at Marquette through to the finish line.

I would like to thank Dr. Klaus Thoeni for his technical expertise in numerical methods and YADE. His advice and collaboration helped make the end simulations possible.

Lastly, I would like to thank Marquette University and all of the faculty and staff that impacted my education and for such a remarkable experience.

## TABLE OF CONTENTS

ACKNOWLEDGEMENTS .....	i
LIST OF TABLES .....	iv
LIST OF FIGURES .....	v
LIST OF ABBREVIATIONS .....	viii
1. INTRODUCTION.....	1
1.1 Background of Mechanically Stabilized Earth Retaining Walls .....	1
1.2 Problem Summary and Motivation.....	4
1.3 Research Objectives and Methodology .....	11
1.4 Thesis Organization.....	14
2. LITERATURE REVIEW .....	16
2.1 Experimental Pullout Tests .....	16
2.2 DEM Development .....	19
2.3 YADE Development and Uses .....	21
3. NUMERICAL BACKGROUND .....	23
3.1 Introduction to the Discrete Element Method .....	23
3.2 DEM Contact Model .....	24
3.3 Simulation Construction in YADE.....	28
3.4 Numerical Stability .....	32
3.5 Contact Tracking and Testing in YADE.....	35
4. DEVELOPMENT OF NUMERICAL PULLOUT SIMULATION.....	39
4.1 Overview of Test Setup.....	39
4.2 Virtual Pullout Box .....	40
4.3 Pullout Reinforcement Creation .....	41
4.4 Application of Normal Load .....	44
4.5 Pullout Particle Generation and Characteristics.....	45
4.5.1 Particle Creation Script.....	45
4.5.2 Particle Sample Packings and Properties .....	46

4.6	Calibration of Particle Samples .....	49
4.7	Load Correction .....	53
4.8	Numerical Pullout Test Procedure.....	55
5.	NUMERICAL PULLOUT TEST RESULTS AND DISCUSSION .....	58
5.1	Test Results with a Uniformity Coefficient of One .....	58
5.2	Test Results with a Uniformity Coefficient of Two .....	60
5.3	Test Results with a Uniformity Coefficient of Three.....	62
5.4	Comparison to Physical Tests .....	64
5.5	Sources of Error and Examination of Differences Between Methods.....	68
5.6	Extraction of Additional Microscale Data .....	71
6.	CONCLUSIONS, LEARNINGS, AND FUTURE WORK.....	75
6.1	Conclusions and Learnings .....	75
6.2	Future Work.....	78
	BIBLIOGRAPHY.....	80
	APPENDIX.....	84
	Appendix A. Notes on Rolling Resistance and Friction Angle.....	84
	Appendix B: Material and Pullout Tests for Airsoft BB Pellets .....	87
	Appendix C. Particle Distribution Generator.....	99
	Appendix D. Miscellaneous Simulation Results and Notes.....	100
	Appendix E. Notes on Computer Core Usage and Parallel Processing.....	108

## LIST OF TABLES

Table 1.1: Series of coarse sieve sizes per ASTM E11-17 [5].....	8
Table 1.2: Computer specifications.....	13
Table 2.1: Summary of experimental pullout test setups in other literature .....	18
Table 4.1: Pullout apparatus properties and dimensions .....	40
Table 4.2: Reinforcement dimensions and properties .....	43
Table 4.3: Load plate dimensions and properties .....	45
Table 4.4: Particle sample characteristics for $C_u = 1$ .....	48
Table 4.5: Particle sample characteristics for $C_u = 2$ .....	48
Table 4.6: Particle sample characteristics for $C_u = 3$ .....	49
Table 4.7: General particle properties .....	49
Table 5.1: Overall simulation parameters .....	58
Table 5.2: Percent difference in residuals between simulation and physical pullout tests .....	66
Table A.1: General pullout parameters for pullout tests conducted by Marquette’s EMSTL lab .	95

## LIST OF FIGURES

Figure 1.1: Cross section of an MSE wall.....	2
Figure 1.2: Slip plane of a soil specimen under a vertical load .....	3
Figure 1.3: Force diagram of reinforcement straps in an MSE wall with a vertical load applied ...	4
Figure 1.4: MSE wall collapse [40].....	5
Figure 1.5: Pullout test diagram .....	7
Figure 1.6: Example particle size distribution plot for well and poorly graded aggregates .....	9
Figure 1.7: Example particle size distribution plot for single-sized aggregates with uniformity coefficients near 1.0 .....	10
Figure 3.1: Simplified DEM simulation process for each step .....	23
Figure 3.2: (a) Particle-particle interaction and (b) depiction of overlap and contact forces between two particles. Reproduced from [15].....	26
Figure 3.3: Detailed simulation loop for single time step in YADE.....	30
Figure 3.4: Sphere on plate contact tracking sample simulation setup .....	35
Figure 3.5: (a) Plot of particle's total lateral displacement versus (b) the particle's circumferential displacement with a particle friction angle of $0^\circ$ .....	36
Figure 3.6: (a) Plot of particle's total lateral displacement versus (b) the particle's circumferential displacement with a particle friction angle of $10^\circ$ .....	37
Figure 3.7: (a) Plot of particle's total lateral displacement versus (b) the particle's circumferential displacement with a particle friction angle of $90^\circ$ .....	37
Figure 4.1: (a) Series of 3 node elements, (b) cylindrical elements that are created to tie the nodes together, and (c) PFacet elements optionally created to fill in the triangular connections .....	42
Figure 4.2: (a) Deformable grid created from nodes and cylindrical elements, (b) deformable plate created from a connected series of PFacet elements.....	42
Figure 4.3: (a) Simulation strap with ribs and overall dimensions, and (b) dimensioning of ribs shown as a function of the overall length or thickness of the strap .....	43
Figure 4.4: Gradation curve for samples tested .....	47
Figure 4.5: (a) Gradation curve for numerical simulation samples and (b) gradation curve for samples tested in [38].....	48

Figure 4.6: (a) Loose particle packing at initial stage of triaxial simulation, (b) particle sample after initial consolidation phase, (c) simulation after target porosity has been met and reconsolidation occurs, and (d) the final state of the particle packing after imposed strain rate ...	51
Figure 4.7: Mohr's Circle resulting from triaxial simulation results .....	53
Figure 4.8: Simulation setup prior to settling .....	56
Figure 4.9: (a) Simulation after settling and strap pullout completes, and (b) zoomed in image of strap after being pulled out 80 mm.....	57
Figure 5.1: Numerical pullout test visualization for $C_u = 1$ .....	59
Figure 5.2: Plot of pullout force versus strap displacement for $C_u = 1$ .....	60
Figure 5.3: Numerical pullout test visualization for $C_u = 2$ .....	61
Figure 5.4: Plot of pullout force versus strap displacement for $C_u = 2$ .....	62
Figure 5.5: Numerical pullout test visualization for $C_u = 3$ .....	63
Figure 5.6: Plot of pullout force versus strap displacement for $C_u = 3$ .....	64
Figure 5.7: (a) Simulation pullout test results with $C_u = 1$ , and (b) physical pullout test results with $C_u = 1.4$ from [38] .....	65
Figure 5.8: (a) Simulation pullout test results with $C_u = 2$ , and (b) physical pullout test results with $C_u = 2$ from [38] .....	65
Figure 5.9: (a) Simulation pullout test results with $C_u = 3$ , and (b) physical pullout test results with $C_u = 3$ from [38] .....	66
Figure 5.10: Residual force versus applied pressure (Taken from the data presented in Figure 5.7) .....	68
Figure 5.11: Change in residual force versus change in applied pressure (Data used from Figure 5.7).....	70
Figure 5.12: Particle rotation during a pullout test. Image created using ParaView [2, 8].....	72
Figure 5.13: Force chains between particles during a pullout test. Image created using ParaView [2, 8] .....	73
Figure A.1: Rotational displacement versus linear displacement of a particle during contact tracking simulations .....	86
Figure A.2: FTIR spectrum from flattened pellet specimen .....	88
Figure A.3: FTIR spectrum from flattened pellet specimen post vaporization .....	88

Figure A.4: FTIR spectrum from pellet residue post vaporization .....	89
Figure A.5: SEM-18-2-4-5; High magnification (x500) of BB pellet specimen.....	90
Figure A.6: SEM-18-2-4-6; High magnification (x1000) of BB pellet specimen.....	90
Figure A.7: EDS spectrums capture from examination of the pellet microstructure .....	91
Figure A.8: Plot of the macroscopic friction angle, $\phi$ , versus the microscopic friction angle, $\phi_{\mu}$ , Taken directly from Figure 6.26 in [16].....	94
Figure A.9: Pullout results from physical tests with a smooth strap.....	96
Figure A.10: Pullout results from physical tests with a ribbed strap .....	96
Figure A.11: Early attempt at pullout simulation with 4x scaled up BBs and strap .....	98
Figure A.12: Plot of pullout force versus displacement while varying particle sizes .....	101
Figure A.13: Varying coefficient of rolling friction, $\eta_{roll}$ , during a pullout test.....	102
Figure A.14: Varying rolling stiffness, $\alpha_{kr}$ , during a pullout test .....	103
Figure A.15: Pullout force vs displacement when strap size was set to 1.5m x 0.10m x 0.008m (LxWxT).....	105
Figure A.16: Pullout force vs displacement when strap size was set to 1.5m x 0.15m x 0.012m (LxWxT).....	105
Figure A.17: Pullout force vs displacement when strap size was set to 1.5m x 0.2m x 0.016m (LxWxT).....	106
Figure A.18: Residual force vs applied pressure for Figures A.15-A.17.....	107
Figure A.19: Simulation time elapsed vs core usage for a 30,000-particle pullout simulation ...	108

## LIST OF ABBREVIATIONS

AABB	Axis-Aligned Bounding Box
AASHTO	American Association of State Highway and Transportation Officials
ASD	Allowable Stress Design
ASTM	American Society for Testing and Materials
DEM	Discrete Element Method
EDS	Energy-Dispersive Spectroscopy
EMSTL	Engineering Materials Structural Testing Lab
FE	Finite Element
FEM	Finite Element Method
FTIR	Fourier Transform Infrared Spectroscopy
LC	Load Correction
LRFD	Load Resistance Factors for Design
MSE	Mechanically Stabilized Earth
RVE	Representative Volume Element
SDEC	Spherical Discrete Element Code
SEM	Scanning Electron Microscope
YADE	Yet Another Dynamic Engine

## 1. INTRODUCTION

### 1.1 Background of Mechanically Stabilized Earth Retaining Walls

Every year in the United States approximately 10 million square feet of mechanically stabilized earth (MSE) retaining walls are constructed [10]. MSE walls are commonly used in highway projects, bridge abutments, and other applications as a cost-effective way of strengthening and stabilizing slopes. The United States alone contains over 60,000 MSE walls throughout our highway systems [4]. In general, an MSE wall consists of granular backfill that is layered between reinforcement material such as steel strips or geosynthetic grids which is then finished with facing panels. Figure 1.1 shows a simple cross section of an MSE wall.

The reinforcement generally acts over two areas: an active zone and a reinforcement zone. The active zone, also known as the Rankine zone, is the region of the backfill that exerts horizontal pressure on the facing panels. The portion of the strips in the Rankine zone,  $l_r$ , provides no contribution to the failure resistance of the MSE wall. As indicated in Figure 1.1., the length of the Rankine zone varies with depth, being maximized near the surface of the backfill. The reinforcement zone is the zone of interaction between the soil and reinforcement strips where frictional restraint is mobilized between the strips and backfill. The effective length of the strips,  $l_e$ , must be sufficient to provide adequate resistance to the pull-out action of the facing panels. For select granular backfills, the effective length is independent of the depth below the surface of the backfill.

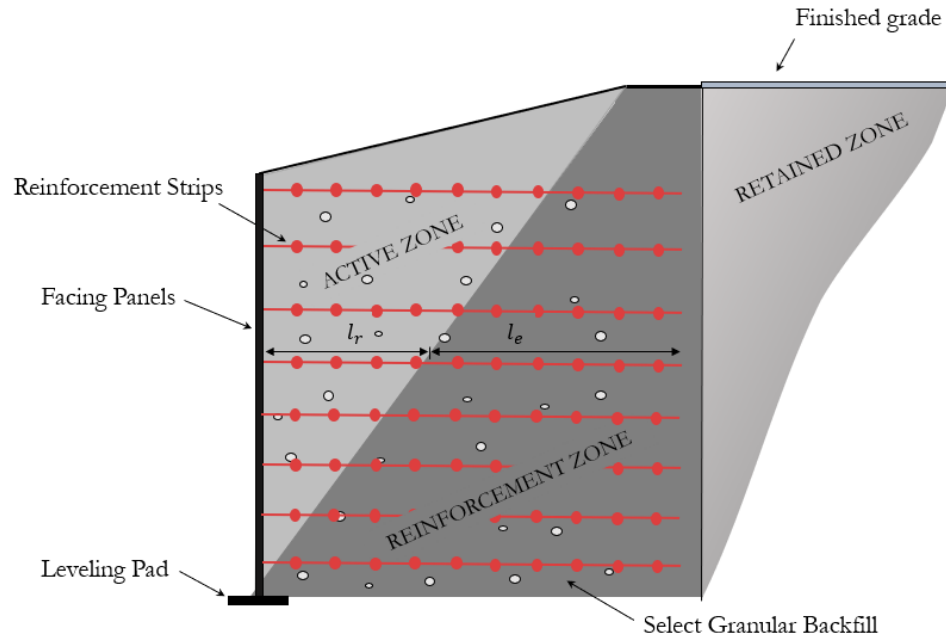


Figure 1.1: Cross section of an MSE wall

MSE walls work to resist one of the most common modes of failure in soils: shear. This type of failure occurs as a result of the shear stress exceeding the shear strength in the material. Consider Figure 1.2 which shows a soil specimen experiencing a vertical load,  $P$ , that is broken into a normal and tangential component,  $P_n$  and  $P_t$  respectively, along a potential slip plane. The normal component acts perpendicular to the denoted slip plane thereby imparting additional shear strength by making the specimen more resistant to sliding. However, the tangential component acts parallel, increasing the force applied along the slip plane, imparting additional shear stress. If at any time the shear stress were to exceed the shear strength, the specimen would fail.

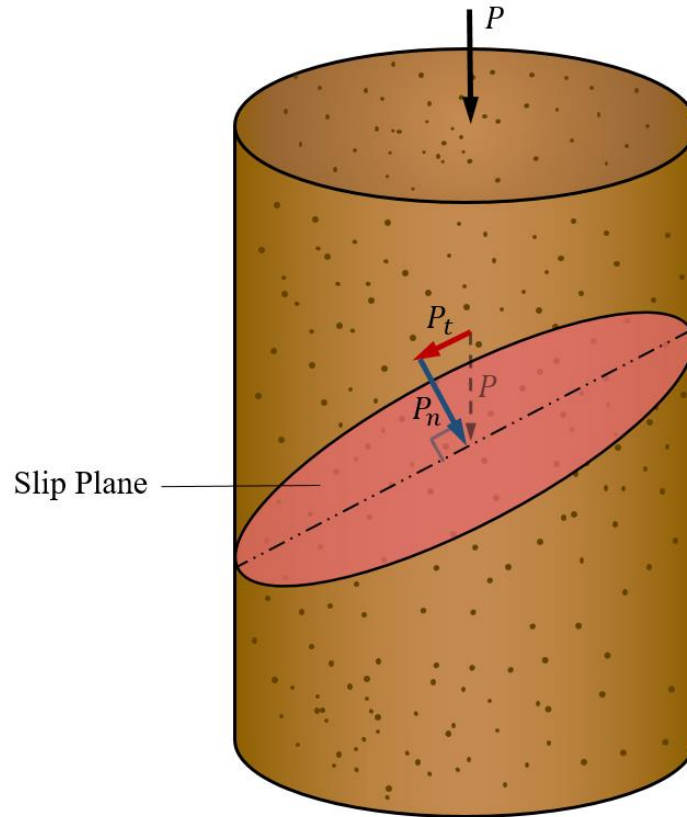


Figure 1.2: Slip plane of a soil specimen under a vertical load

When an MSE wall is constructed, the vertical load puts the reinforcing material in tension and, in turn, the tensional forces from the reinforcement cause a confining pressure through the structure which makes the soil resistant to collapsing by increasing the overall shear strength. This effect is opposite of that which is seen in Figure 1.2 as the additional forces help fortify rather than weaken the structure against sliding. Each layer of reinforcement applies a compressive load which, when broken into normal and tangential components, improves the structure's strength against shearing. This structure is shown in Figure 1.3. Due to their additional support and overall simplicity, MSE walls have become one of the most common ways in society of retaining soil and stabilizing slopes.

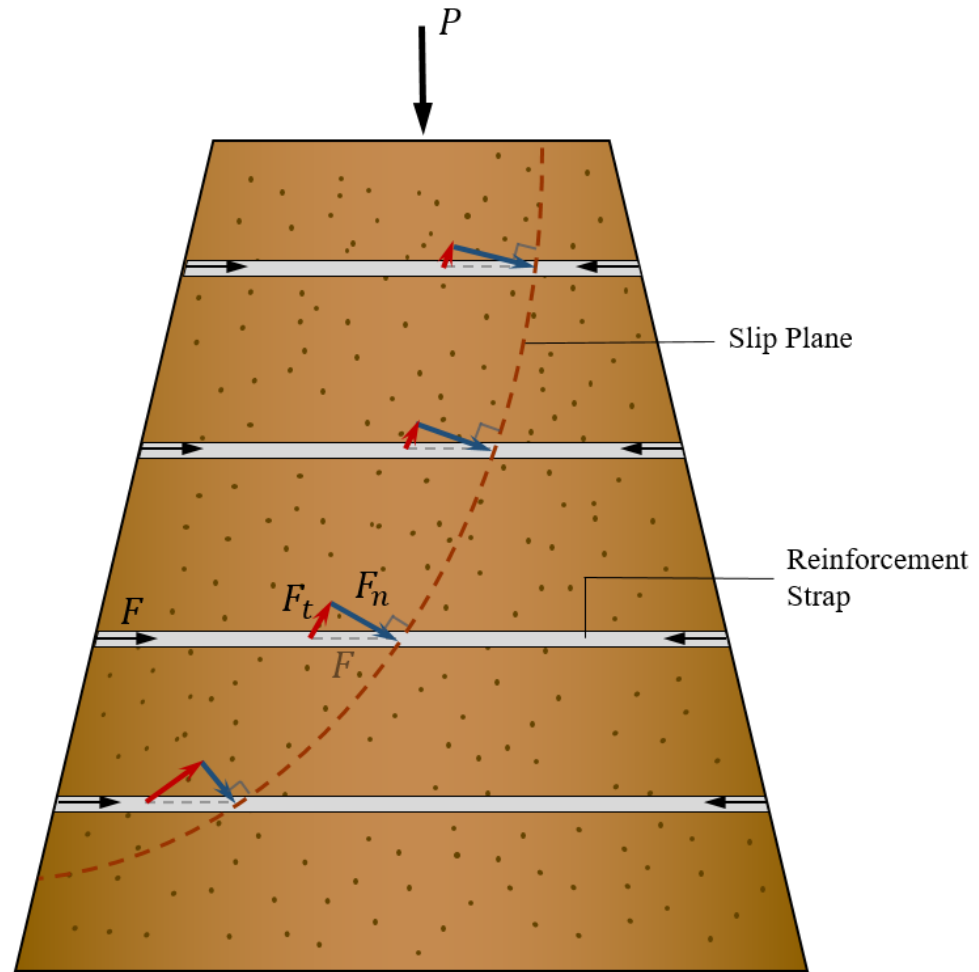


Figure 1.3: Force diagram of reinforcement straps in an MSE wall with a vertical load applied

## 1.2 Problem Summary and Motivation

MSE walls may appear simple in their nature but are inherently complex with wide varieties of design challenges that cannot often be generalized. Wendland, who has more than 20 years of geotechnical engineering experience, points out some of the crucial design factors that result in MSE wall failures in his article “When Retaining Walls Fail” [40]. Throughout his career he led investigations into retaining wall failures and noted that roughly 90% of soil problems are, in reality, water related and that the majority of retaining walls fail during periods of heavy rain. Wendland goes on to state that this soil problem could be for a variety of reasons such as soil samples being gathered during a dry season resulting in false strength estimates, varying porosity

of backfill materials leading to unrepresentative lab results, and backfill softening over time due to water exposure just to name a few [40]. In addition, many times proper lab tests with the backfill are forgone in lieu of using default, generalized design factors. Often, these retaining structures are constructed as if following a generic recipe due their specious simplicity. In turn, many walls are overdesigned and end up costing more than is necessary, or the walls are not designed properly and end up failing as shown in Figure 1.4.



Figure 1.4: MSE wall collapse [40]

The design processes for MSE walls inherently have large amounts of uncertainty due to a lack of understanding of the granular micromechanics and phenomena acting within the walls. Currently, these uncertainties are primarily accounted for using two different design approaches:

1. Allowable Stress Design (ASD)
2. Load Resistance Factors for Design (LRFD)

The ASD method is mostly outdated but compensates for uncertainty in the applied loads and material resistance together by exaggerating the factor of safety required for the imbedded

reinforcement straps. The LRFD approach has replaced ASD in recent years and instead acknowledges uncertainties in both the applied loads,  $Q_i$ , and the material's ultimate resistance,  $R_n$ , individually. Uncertainties in the material are compensated for by a resistance factor,  $\phi_n$ , which is usually less than one and predetermined by AASHTO standards. Similarly, uncertainties in the loads are accounted for by load factors,  $\gamma_i$ , which are typically greater than one and are also predetermined for various types of loads. Additionally, loads are altered by modifiers,  $\eta_i$ , which are based on ductility, redundancy, and operation importance of loads [1]. Ultimately when considering a design under the LRFD approach, the pullout resistance factor,  $F^*$ , must be greater than the sum of the adjusted loads which can be expressed by Equation (1.1):

$$\sum \eta_i \gamma_i Q_i \leq \phi_n R_n = F^* \quad (1.1)$$

Currently, a pullout resistance factor is determined by performing pullout tests. In these tests a reinforcement strap is embedded between two layers of aggregate inside of a rigid container. Optionally, a normal pressure is often applied to the top layer of aggregate to simulate the pressure on a strap at varying depths. The reinforcement strap is then pulled out of a slit on one face of the box and pullout force can be measured as function of the strap displacement. A simple diagram of this test can be seen in Figure 1.5. The pullout resistance is then defined as the ultimate force generated during the test and the pullout resistance factor can be found by Equation (1.2).

$$F^* = \frac{P_r}{\sigma_v L_e C \alpha} \quad (1.2)$$

In this equation,  $P_r$  is defined as the pullout resistance,  $\sigma_v$  is the normal stress being applied at the reinforcement level,  $L_e$  is the length of reinforcement contacted by the aggregate,  $C$  is the reinforcement surface area geometry factor (equal to 2 for straps), and  $\alpha$  is the scale correction factor which is equal to 1 for steel.

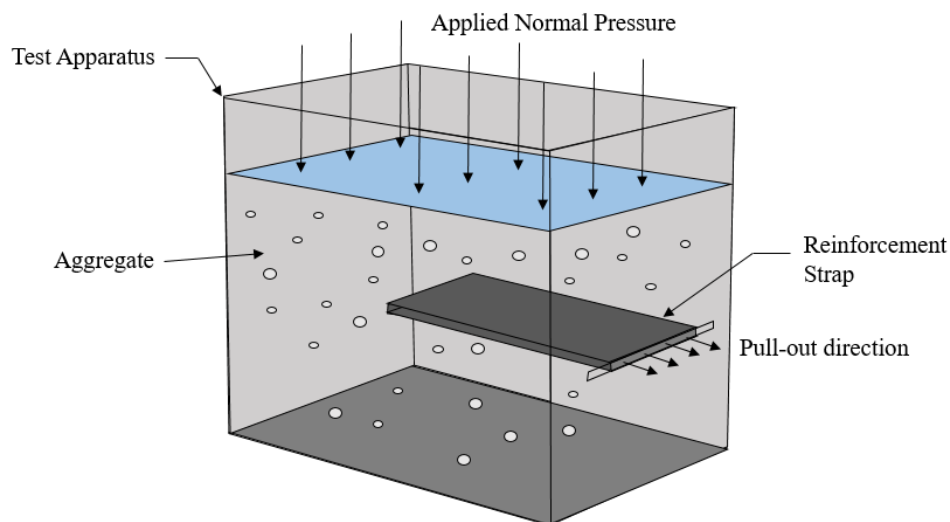


Figure 1.5: Pullout test diagram

Ideally, to ensure the most reliable wall design, pullout tests should be conducted for each project using samples of the intended backfill and reinforcement. Due to the difficult nature of setting up well-controlled pullout tests and other project constraints it is common to use a predetermined pullout resistance factor from the AASHTO [1]. Default resistance factors are determined based on a combination of the uniformity coefficient,  $C_u$ , and the internal friction angle of the backfill,  $\phi$ . The coefficient of uniformity is a value commonly used in geotechnical engineering to characterize the variation in aggregate particle sizes.  $C_u$  is a dimensionless ratio computed as shown in Equation (1.3) where  $D_{60}$  and  $D_{10}$  are defined as the particle sizes, or sieve sizes for which 60% and 10% of the aggregate particles, by weight, would pass.

$$C_u = \frac{D_{60}}{D_{10}} \quad (1.3)$$

In practical applications,  $D_{60}$  and  $D_{10}$  are graphically determined from a particle gradation curve that is developed from results of a sieve analysis. A standard sieve series is typically used for gradation analysis, whereby the openings in each successive sieve are reduced by a factor of approximately 2. Table 1.1 shows an example sieve series per ASTM E11-17 [5]. For well-graded aggregates with a wide range of particle sizes,  $C_u$ , values of 4 or more are common. For poorly graded aggregates, where most or all of the aggregate particles are of the same size,  $C_u$  values range from about 4 to near unity. Figure 1.6 illustrates the process of determining  $D_{60}$  and  $D_{10}$  with example well graded and poorly graded aggregates.

Table 1.1: Series of coarse sieve sizes per ASTM E11-17 [5]

Sieve Size	Nominal Opening (mm)
3 in.	75
1-1/2 in.	37.50
3/4 in.	19
3/8 in.	9.50
#4	4.75
#10	2.00
#16	1.18
#40	0.425
#100	0.150
#200	0.075

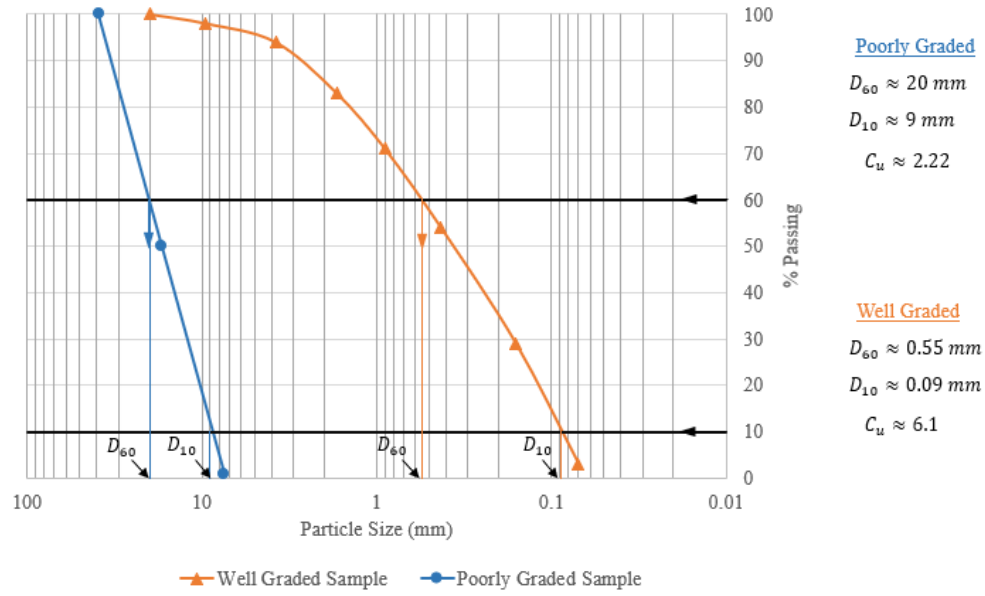


Figure 1.6: Example particle size distribution plot for well and poorly graded aggregates

It is important to note that for backfill aggregates with a single particle size, 100% of the particles would pass through any sieve with openings larger than that particle size and 0% would pass through any sieve with openings smaller than that particle size. Figure 1.7 illustrates example gradation curves for two single-sized aggregates, each with uniform particle sizes but with different numerical sizes of particles. As shown, the different sets of  $D_{60}$  and  $D_{10}$  values each produce a  $C_u$  value near 1.0, but because the gradation curves are never purely vertical, an actual value of 1.0 can never be computed.

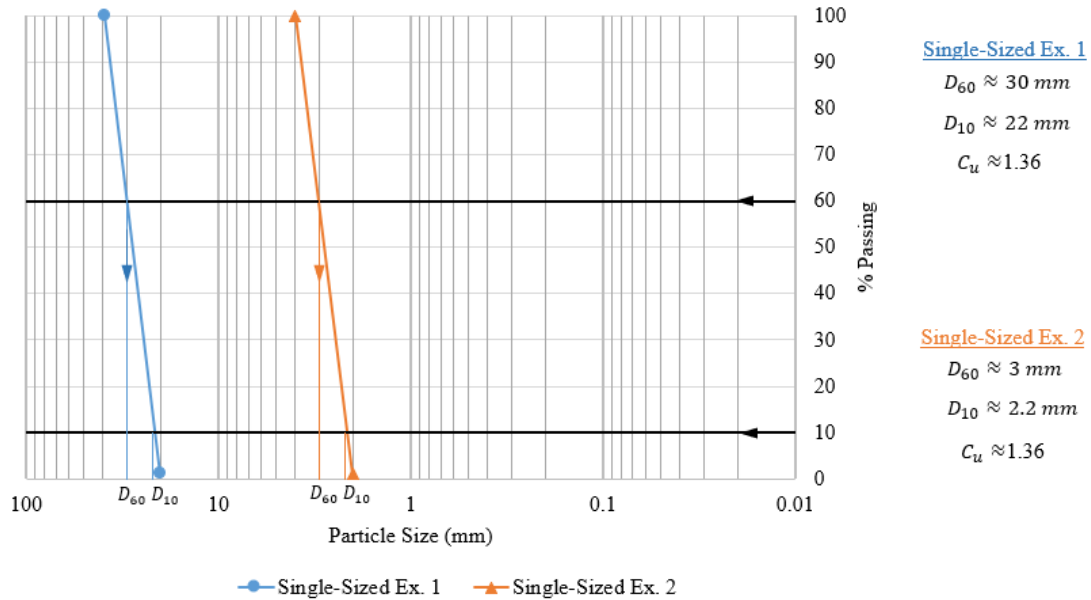


Figure 1.7: Example particle size distribution plot for single-sized aggregates with uniformity coefficients near 1.0

In common design applications, the select backfill materials are free-draining to avoid hydro-static pressure build-up behind the wall, resulting in small  $C_u$  values. In the event that the uniformity coefficient is unknown, a value of 4 is assumed which is the lowest value with AASHTO specified resistance factors [1]. If the uniformity coefficient is known to be below a value of 4 pullout testing would be required to determine the actual resistance factors. Therefore, there is a much greater uncertainty in utilizing default resistance factors compared to physically testing the specific backfill against the reinforcement. The coefficient of uniformity is of particular importance in this research as the numerical simulations that were created are designed relative to experimental pullout tests with uniformity coefficients of less than four.

This research aims to reduce the uncertainty in designing MSE walls by modeling virtual pullout tests. If proven to be accurate, numerical tests would have substantial benefits compared to laboratory tests. One of the greatest offerings of a numerical model is the ability to setup and perform tests quickly without the use of physical resources. In addition, a computer model is

easily duplicated or modified whereas a laboratory pullout test is difficult to replicate precisely. In a virtual model, aggregate packs can be created with the same packing density, porosity, and uniformity for every test whereas a laboratory test will always have some degree of variability. For this reason, while a uniformity coefficient of one is unachievable in practice, a numerical simulation can generate a perfectly uniform aggregate packing if desired. However, possibly the most substantial benefit of a numerical model is the ability to collect and understand microscale data between the reinforcement strap and granular backfill. Detailed information regarding granular phenomena such as force chains and particle rotation will help minimize the uncertainties inherent in MSE wall design by providing new insights that, once understood and evaluated, can be appended into standard codes and practices for future applications.

### 1.3 Research Objectives and Methodology

At the highest level, the goal of this research is to develop a numerical pullout test model utilizing the Discrete Element Method that can accurately reproduce results from laboratory pullout tests. Additional objectives of the research are as follows:

1. Create a robust pullout test simulation that can be calibrated quickly, run more efficiently than current laboratory tests, and allow for easy manipulation of test parameters.
2. Develop a simple triaxial compression simulation that can be used as a method of calibrating particle samples.
3. Test the ability to model different particle size distributions and varying uniformity coefficients with results being compared to those found through physical tests performed by other researchers.
4. Utilize the simulations to access microscale data that is unobtainable in lab testing such as force chains and particle rotations.

Primarily, this research will use of the open-source DEM framework of YADE [33], Yet Another Dynamic Engine, for the development of the numerical models. The computational aspects of the discrete element method are written in C++ which account for details such as collision detection and contact laws. Independent scripts written in Python are used to construct the virtual environments, control simulations, and post process data. All of the code provided by YADE can be manipulated and modified to suit the user's need. Simulations will be run on a computer with specifications as defined in Table 1.2. The enhanced processing power of this computer allows for improved simulation times when compared to mainstream computers. In addition, a virtual computer run through Oracle VM VirtualBox is used on the computer for physically running YADE while post processing visualization of information like force chains is done on the computer with ParaView, an open-source visualization and data analysis tool [8].

Table 1.2: Computer specifications

Identifier	Basic Information	Additional Information	Quantity
<b>Architecture</b>	Quantum TXR430-512R	<ul style="list-style-type: none"> <li>• Tower / 4U Convertible Chassis</li> <li>• Supports 2x E5-2600 v3 Processors</li> <li>• DDR4 Memory</li> <li>• Supports Up To 3x 5.25IN Bays</li> <li>• 8x 3.5IN Hot-Swap HDD Bays</li> <li>• Up To 4x Double-Width GPU</li> <li>• Up To 1TB DDR4 Memory</li> <li>• Dual Gigabit Ethernet LAN</li> <li>• 2000W Redundant Power Supplies</li> </ul>	1
<b>Processor</b>	Intel Xeon E5-2687W v3	10C, 3.1 GHz 25M, Support DDR4-2133	2
<b>Memory</b>	32GB DDR4	2133MHz LR ECC LRDIMM	8
<b>Primary Storage</b>	512GB 2.5 SATA III	Internal Solid State Drive (SSD) ** OS DRIVE **	1
<b>Secondary Storage</b>	1.8 TB SAS	12Gb/s 2.5IN Internal Hard Drive ** RAID10 **	8
<b>RAID Controller</b>	LSI 9300 MegaRAID SAS 9361-8i (LSI00417) PCI	<ul style="list-style-type: none"> <li>• Express 3.0x8 Low Profile SATA/SAS</li> <li>• 1 GB Cache</li> <li>• High Performance Eight-Port 12 Gb/s RAID Controller</li> </ul>	1
<b>RAID Cache</b>	LSI LSICVM02	(LSI00418) CacheVault Accessory Kit for 9361 Series)	
<b>GPU</b>	Nvidia Tesla K80	24 GB GDDR5 384-bit PCI Express 3.0 - Passive Cooling	3
<b>GPU Cooling</b>	Passive Cooling	Passive GPU Kit for 4U 4GP USystem	1
<b>Ethernet</b>	Intel X540T2 – 1 Gbps	Ethernet Converged Network Adapter 100Mbps/1Gbps/10Gbps PCI Express 2.1 x8; 2 x RJ45	1
<b>Power</b>	PC Smart UPS X 3000VA	Rack/Tower LCD100-127V	1
<b>Internal Cabling</b>		0.6m Internal Cable SFF8643 to x4 SATA HDD (mini SASHD to SATA data port)	2
		2.5" to 3.5" SATA/SAS6Gb SSD Hard Drive Converter / Adapter / Bracket	9
<b>Additional Components</b>		4U / Tower Conversion Kit / Rail Kit	1
		Windows 8.1 Professional 64Bit	1
		Samsung S24D300H 24IN LCD Monitor	1

Numerical simulations for the pullout tests use parameters and information corresponding to physical pullout tests presented in [38]. The research detailed in [38] conducts tests on relatively uniform aggregates, which is an ideal starting point for the numerical models. Relatively uniform aggregates reduce the complexity of the particle samples that need to be generated in the computer model, since relatively few particle sizes are needed. Samples that are numerically generated are calibrated in a simple triaxial simulation that is validated against triaxial testing performed in [38].

## 1.4 Thesis Organization

This study is presented in six chapters and is followed by an appendix with some additional insights. Each of these sections is summarized below:

Chapter 1 presents a background and motivation for the research being performed. In addition, it lists out the goals and methods that were used throughout.

Chapter 2 briefly reviews some relevant studies and literature that have been done on topics in relation to this research. This includes a dive into several physical pullout tests that have been conducted for a variety of applications, a brief explanation of the development of the Discrete Element Method, and more specifically some uses of YADE, the open-source project used to develop the numerical simulations here.

Chapter 3 outlines in more specifics the Discrete Element Method by discussing some of the generic formulations and how it works. Much of the focus of this chapter is how DEM is handled inside of YADE as some other applications or software may be setup differently.

Chapter 4 goes into the details and setup of the study which involves a discussion of how the numerical simulation was created in order to duplicate the tests and results presented in [38]. In addition, this chapter goes over how the test runs when pieced together.

Chapter 5 presents the results of the simulated tests individually and comparatively to the physical tests performed in [38]. Along with the results, there is some discussion of additional data collected from the simulations and possible sources of error.

Chapter 6 summarizes all the work that was done and offers potential future topics that can be researched as additional branches of this study.

Appendix A offers some insights and notes collected regarding rolling resistance throughout the research. This characteristic was explored early on in the research but ultimately was incomplete and serves as an area of future exploration.

Appendix B shows some of the early work in this research which involved setting up and performing physical pullout tests with airsoft BB pellets for baseline simulations. A lot of materials testing was performed to try to characterize the BB pellets in a numerical simulation, but this did not end up being the primary path of the research.

Appendix C is a more detailed discussion into how the particle packings were generated for the simulation. A spreadsheet was used to obtain initial guesses regarding the quantity of particles necessary in each size, the spacing, the size of the box, etc.

Appendix D highlights some miscellaneous results collected while developing the final pullout setup used in this research. These results offer some interesting insights into topics that could potentially be further explored.

Appendix E concludes the paper with some comments on computation time, parallel processing with YADE, and general details regarding simulation workflow.

## 2. LITERATURE REVIEW

With the adoption of MSE walls, pullout testing has become one of the primary methods of investigating and understanding the interactions that take place inside of these structures. The wide range of uses and applications of MSE walls has sparked many studies with a focus on capturing new knowledge to continue developing better design practices. The primary focus of this chapter is to explore some of the studies that have been performed around pullout testing to gain a detailed understanding of the learnings and results that have been collected through the years.

There has also been a growing interest in numerical simulations being used to study and characterize physical phenomenon. One specific way these simulations are performed is through the use of DEM which has been a rapidly expanding field over the last half century. The secondary objective of this chapter is to take a deeper look at some of the work that has been done developing and using the DEM approach to help capture and model real-world situations.

### 2.1 Experimental Pullout Tests

The bulk of the research presented in this thesis references a study performed by Weldu [38] in which he studied the effects of aggregate uniformity during pullout tests. A specific emphasis was placed on how the pullout resistance changed when the aggregates were nearly uniform in size. Aggregate packings were tested with a uniformity coefficient as low as 1.4 and as high as 14. The tests performed resulted in the conclusion that all aggregate samples had similar trends in pullout resistance, but the packings with a higher coefficient of uniformity tended to have a higher overall resistance. In addition, it was observed that the uniformity of the particles had a larger effect on the pullout force at lower normal pressures. The tests being performed with an aggregate packing of roughly the same size made this study ideal to duplicate.

Beyond Weldu, there have been a large variety of studies performed regarding pullout tests. One important area of study has been based around the type of reinforcement used for reinforced soil. Gurung and Iwao [19] performed some work into investigating pullout responses for inextensible (steel) and extensible (geogrid) reinforcements which was followed up later by more detailed studies in each topic. Mohiuddin [28] studied pullout effects of seven geosynthetic reinforcement structures while Lawson, et al. [25] reviewed twenty-two different pullout tests that were done using metallic reinforcement straps and grids. Comparing all these studies and drawing conclusions is extremely difficult due to the setup varying greatly with regards to aggregate type, apparatus size, reinforcement dimensions, normal stress application method, etc. Details of several additional test setups are summarized below in Table 2.1, which helps to show the differences in some of the studies:

Table 2.1: Summary of experimental pullout test setups in other literature

<b>Reference:</b>	<b>Chang et al. (1977) [12]</b>
Aggregate:	Gravelly, poorly graded, sand
Reinforcement:	Steel strap; 1370 mm x 60 mm x 3 mm (Length x Width x Thickness)
Apparatus:	1372 mm x 91.4 mm x 457 mm (Length x Width x Height)
Normal Stress:	Hydraulic jack; 69 kPa
Pullout Method:	Hydraulic jack; Strain rate: 0.05 mm/min
<b>Reference:</b>	<b>Suits et al. (2005) [34]</b>
Aggregate:	Clean and silty sand
Reinforcement:	Steel strap; 750 mm x 50 mm x 3 mm (Length x Width x Thickness)
Apparatus:	1000 mm x 400 mm x 500 mm (Length x Width x Height)
Normal Stress:	Airbag; 30, 100, and 200 kPa
Pullout Method:	Hydraulic Ram; Strain rate: 1 mm/min, 10 mm/min
<b>Reference:</b>	<b>Rathje et al. (2006) [30]</b>
Aggregate:	Crushed concrete; recycled asphalt pavement
Reinforcement:	Ribbed steel strap; 450 mm x 50 mm x 4 mm (Length x Width x Thickness)
Apparatus:	500 mm x 500 mm x 337.5 mm (Length x Width x Height)
Normal Stress:	Airbag; 10-130 kPa
Pullout Method:	Pneumatic piston; Strain rate: 1 mm/min
<b>Reference:</b>	<b>Lawson et al. (2013) [25]</b>
Aggregate:	Gravelly aggregate ( $C_u=12-180$ ) and sandy aggregate ( $C_u=4.4-7.0$ )
Reinforcement:	Ribbed steel strap; 1200, 1800, 2400, 3600 mm x 50 mm x 4 mm (Length x Width x Thickness)
Apparatus:	3700 mm x 3700 mm x 1220 mm (Length x Width x Height)
Normal Stress:	Hydraulic jack; 26-270 kPa
Pullout Method:	Hydraulic jack; Strain rate: 1.25-6 mm/min
<b>Reference:</b>	<b>Weldu et al. (2016) [39]</b>
Aggregate:	Crushed limestone ( $C_u=1.4-14$ )
Reinforcement:	Ribbed steel strap; 1500 mm x 50 mm x 4 mm (Length x Width x Thickness)
Apparatus:	1500 mm x 600 mm x 600 mm (Length x Width x Height)
Normal Stress:	Airbag; 25, 41, 69, 103, 138 kPa
Pullout Method:	Hydraulic jack; Strain rate: 10-15 mm/min

Some of the largest differences between these studies were the aggregates being tested and the dimensions of the setups. A lot of these studies were built around a specific project or area of focus rather than investigating pullout tests in a general sense. For example,

Jayawickrama et al. was focused on the Texas region and therefore the aggregate used and test setup were dictated by the project and region. Rathje et al. similarly investigated crushed concrete and recycled asphalt pavement to determine the feasibility of using those aggregates in an MSE wall backfill application. Most of the conclusions presented in these studies therefore pertain specifically to the project and aggregates in question.

## 2.2 DEM Development

DEM has become a very popular tool in performing numerical, particle-based studies and modeling due to its flexibility in manipulating test setups, ease of iterating, and ability to extract any data from any point during a test. Throughout the years, DEM packages have become increasingly more common wherein major developments in the field have been implemented and compressed into easy-to-use interfaces. Cundall and Strack [13] are credited in developing one of the more common constitutive models used throughout DEM. In their research, DEM was developed wherein particle displacements and contact forces were calculated using a combination of Newton's second law and a force-displacement law. These two laws would yield the motion of the particle based on forces it experienced and the contact forces generated as a result of the particle's movement. A small time step was necessary with this approach as it limited force and displacement propagation to only neighboring particles. Under the assumption of a sufficiently small time step, acceleration and velocity of a particle could be considered constant which meant forces were resolved based on the contact experienced with neighboring particles.

Schwartz and Weinstein [31] performed a study wherein they proposed using the Coulomb yield criteria to characterize granular aggregates. The research showed that this criterion could in fact be used to derive necessary modeling information such as cohesion, stress profile, loads, and more when done under closed die compaction. Extending this knowledge meant that numerical simulations may be used to accurately predict and model the behavior of granular substances when in compression.

Another major development for DEM came in the form of applying rolling resistance from a study performed by Iwashita and Oda [22]. This area of study was also expanded on by Ai et al. [3] in 2010. The rolling resistance was defined by some key parameters, two of which were the coefficient of rolling friction and the rolling stiffness. Depending on the DEM software, rolling resistance may be implemented differently but for the use of YADE it is an elastic-plastic spring-dashpot model as described in Ai et al. In the model proposed by Ai, a rolling resistance moment is the resultant of multiplying the coefficient of rolling friction by the rolling radius and normal force. A rolling angle may also be determined with this model by dividing the rolling resistance moment by the rolling stiffness.

One additional development on the topic of DEM was presented by Guo and Zhao [18] in 2014 where they presented on an approach to coupling DEM simulations with FEM in granular distributions. This study effectively showed a method of multiscale modeling numerical simulations which has the potential to implement the best features of each method and merge the two. For example, DEM has a costly computation time by needing to resolve every contact at each time step but that can be helped with the addition of FEM aspects. Defining macroscale parameters based on the DEM microscale information would allow for modeling RVEs (representative volume elements) in regions of less interest in the simulations. Therefore, particles would still be modeled in key areas of focus but further away the DEM assembly would be attached and transition into the FEM mesh, or RVEs, that act according to bulk responses. This type of modeling could drastically reduce computation time for simulations that require hundreds of thousands of particles or more while still allowing for extraction of microscale behaviors. While this type of multiscale modeling has yet to be thoroughly implemented and explored in 3D it still presents the opportunity to create larger, more complex simulations and presents a lot of potential uses and benefits in numerical modeling.

### 2.3 YADE Development and Uses

While many DEM packages exist, YADE stands out as one of a few free, open-source software applications that makes use of the particle-based numerical method. Prior to YADE, Donze et al. [14] created SDEC, the Spherical Discrete Element Code, in 1990 which was built on the foundations of DEM. As the name implies, it utilized spherical rigid elements which he used in his research to study rock blasting and the fracture mechanisms associated with the topic. Later, in 2004, SDEC was reformulated into what is now known as YADE [33] and still includes the most up-to-date version of SDEC. In rewriting this code, the computational code was built using C++ but users of the software are able to construct simulations rapidly and provide inputs via Python scripting. Since the introduction of YADE it has been used in hundreds of studies.

One of the more common uses of YADE is simulating and testing aggregates under triaxial compression which is very frequently done in civil engineering applications. For example, Kozicki et al. [24] studied the behavior of sand under drained triaxial tests with the help of YADE to build their simulations which were then compared to physical tests. Similarly, Wang and Li [37] in 2014 examined the response of granular media using a series of triaxial compressions tests in which a modified DEM approach was implemented with the use of YADE. Most recently, in 2017, Mitra [27] published a study wherein blocky, ceramic materials were simulated under uniaxial and triaxial compression tests to understand the behavior of the aggregate better. Helping with all these studies and this research is the fact that YADE has developed a useful triaxial test utility which can be used as a strong foundation in building simulations that are trying to understand the behaviors of granular media.

While not as common as modeling triaxial tests, some work has been done to model reinforced soil pullout tests. Tran [36] in 2014 performed a study where FEM and DEM framework were used together in the modeling of a pullout system using a geosynthetic grid. The grid used was created using part of the FE package offered by YADE and consisted of 8-node brick elements. The particles were modeled as sand but had to be scaled up to keep computational

cost and simulation time realistic. Interfacing elements were implemented to capture the interactions between the FEM and DEM bodies. The research demonstrated that this FE-DE approach could effectively be used to model the behavior between geogrids and soils in reinforced earth.

Going a step further, Effeindzourou et al. [15] used YADE to model deformable structures using DEM. The foundation of the deformable structures was produced by linking a series of elements together. Presented in this paper is the idea of connecting a cylindrical element between two spherical elements which can be extrapolated to form a series of interconnected cylindrical members which effectively forms a grid. The paper introduces a new type of element known as a PFacet which is a triangular element composed of three spheres (nodes) and three links (cylinders) [15]. One of the applications discussed regarding the use of these deformable structures was pullout tests. Sample pullout tests were created by Thoeni [15] where a geosynthetic grid was created using linkages of cylindrical elements and was then followed by a deformable, solid membrane that was constructed with PFacet elements. The research showed the effectiveness and multiple uses of deformable structures inside of DEM applications. The construction method of the pullout tests done for Effeindzourou's study [15] was also tested and briefly implemented in simulations created for this research which is discussed in Section 4.3.

Beyond just these applications, YADE has been used to study a wide range of topics. For example, Shiu [32] used YADE to model and understand the behavior of missile impacts on concrete slabs, Thoeni [35] performed a study with YADE investigating trajectories of rockfall when drapery systems are used, and Bourrier [11] constructed DEM simulations to understand plant roots and their effect on reinforcing soils.

### 3. NUMERICAL BACKGROUND

#### 3.1 Introduction to the Discrete Element Method

The Discrete Element Method (DEM) is a numerical approach that treats contacts and interactions on an individual particle basis which can be used to help predict soil behavior and granular flow among many applications. In general, particles are modeled as spheres which are rigid and locally deformable. Numerical models that make use of DEM run in a cyclical fashion which start by detecting contacts. When a collision is detected a new interaction is created with stiffness properties that are predefined or are determined as a result of particle properties. For an interaction, a constitutive contact law is used to compute the force which is applied to the particles involved in the collision. Depending on the constitutive law selected and the DEM software package used, damping is necessary and commonly incorporated to dissipate energy from unrealistic particle behaviors. From there, particle accelerations can be found by way of Newton's second law with velocities and displacements following accordingly from Newtonian mechanics. At that point, particle positions are updated, the numerical model is incremented to the next step, and forces are reset. Figure 3.1 summarizes a general DEM cycle within simulations.

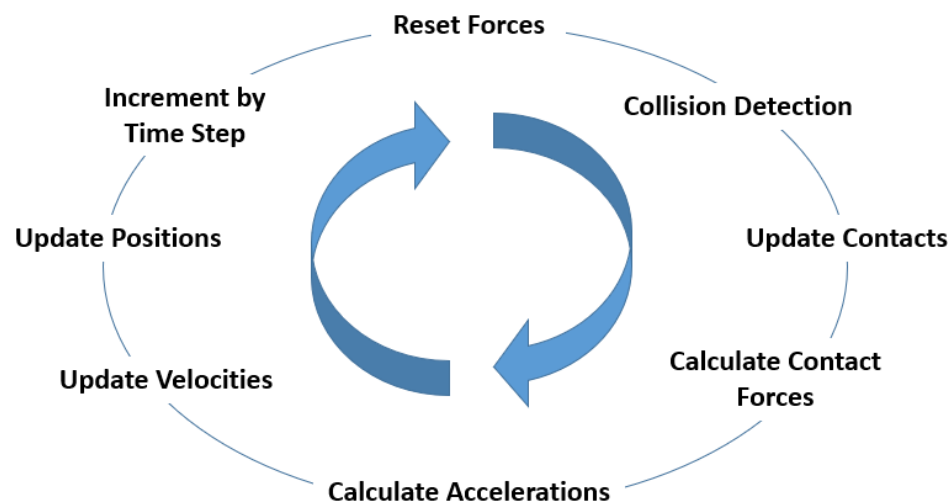


Figure 3.1: Simplified DEM simulation process for each step

DEM functions under the key assumption that a time step can be selected that is small enough such that forces and displacements cannot propagate beyond a particle's immediate neighbors. This detail means that at any given time step resulting forces of particles are determined exclusively by the other particles that are in direct contact. As the time steps are extremely small, velocities and accelerations can be treated as constant [13]. DEM software packages operate under this key assumption, but most utilize adaptive time stepping between iterations. Section 3.4 goes into more detail on the subject of time step within YADE.

DEM is an approach that models particle interactions on the microscale which can then be extrapolated to predict behaviors of the material on the macroscale.

### 3.2 DEM Contact Model

In the last century there have been a variety of constitutive laws that have been presented and implemented into DEM packages. One of the most commonly used models was developed by Cundall and Strack and is built on the foundation of a linear spring and damper which handle the elastic behavior of the model and the energy dissipation [13, 21]. The contact law they described makes use of an additional three critical parameters: friction coefficient, normal stiffness, and tangential stiffness. One of the unique distinctions of the Cundall-Strack solution is that there are no tensile forces [27].

The Hertz-Mindlin model [20, 26] is also commonly used as it can model both quasistatic and dynamic problems whereas the Cundall-Strack solution is limited to problems that are static and quasistatic. A non-linear elastic model, the Hertz-Mindlin solution utilizes rolling resistance and non-linear viscous damping to help combat non-quasistatic problems [33].

The open source platform of YADE provides a spectrum of DEM models that can be adopted and used in a numerical simulation however the general formulation of how the contacts are handled remains the same. A contact model is used during a collision to relate relative

displacements and rotations to the contact force,  $F$ . As a means of detecting contacts, each particle is surrounded by an axis-aligned bounding box (AABB) as seen in Figure 3.2. The initial contact algorithm used in YADE is known as sweep and prune [9]. In this method a quick pass is performed over all particle pairs which identifies potential contacts through the presence of overlap between two AABBs. Any particle pairs that do not have overlapping boundary boxes are considered not in contact and dismissed which greatly helps reduce computational costs. Upon completion of the sweep and prune, a more refined constitutive law is implemented to revisit any particle pairings that were identified as having overlapping boundary boxes. At this point, pairs are evaluated in greater detail for physical overlap between the actual spherical bodies. If an overlap exists between the two bodies a new contact is established. This overlap is identified as the normal displacement,  $u_n$ , which is shown in Figure 3.2. From each contact normal and tangential contact forces,  $F_n$  and  $F_t$ , emerge for which are calculated according to the chosen constitutive law, which for this thesis is the non-cohesive, elastic-frictional Cundall-Strack contact model. The contact forces are defined in Equations (3.1) and (3.2) where  $k_n$  and  $k_t$  are the normal and tangential contact stiffness.

$$F_n = k_n u_n \quad (3.1)$$

$$F_t = -k_t u_t \quad (3.2)$$

In the case of Figure 3.2, two particles in contact, the normal and tangential stiffness can be calculated by Equations (3.3) and (3.4) with  $E_i$  denoting Young's modulus,  $R_i$  as the radius, and  $\nu_i$  as Poisson's ratio for each respective particle [15].

$$k_n = \frac{2E_1 R_1 E_2 R_2}{E_1 R_1 + E_2 R_2} \quad (3.3)$$

$$k_t = \frac{2E_1 R_1 v_1 E_2 R_2 v_2}{E_1 R_1 v_1 + E_2 R_2 v_2} \quad (3.4)$$

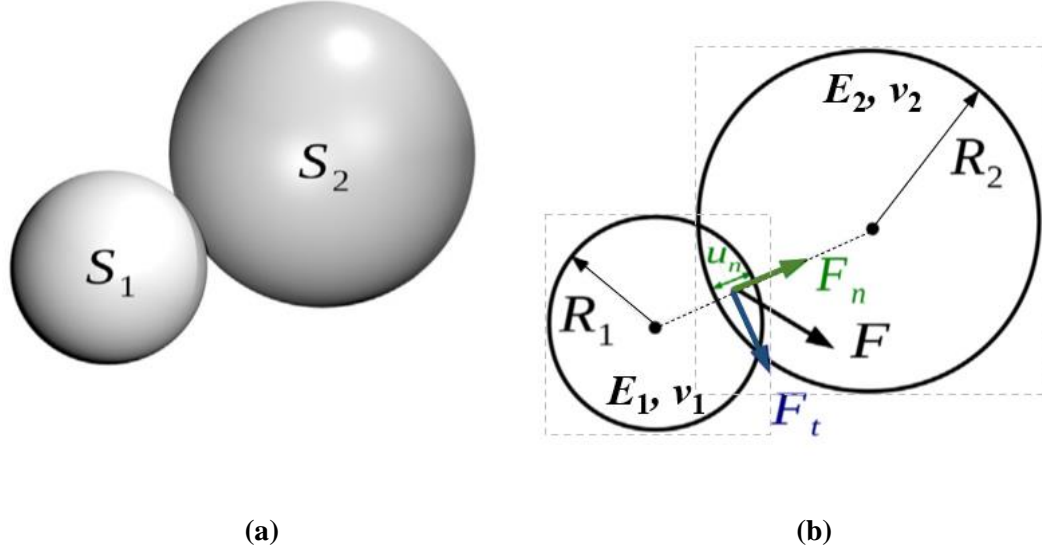


Figure 3.2: (a) Particle-particle interaction and (b) depiction of overlap and contact forces between two particles. Reproduced from [14].

The twisting and bending moments,  $M_t$  and  $M_b$ , which develop from the contacting particles can be derived through the relative rotations of the particles and are defined in Equations (3.5) and (3.6).

$$M_t = k_t \Omega_{12}^t \quad (3.5)$$

$$M_b = k_b \Omega_{12}^b \quad (3.6)$$

In these equations,  $k_t$  and  $k_b$  express the contact stiffness relative to the twisting and bending moments respectively. In addition, the notation of  $\Omega_{12}$  is used to represent a rotational vector of the relative motion between contacting particles one and two. Therefore,  $\Omega_{12}^t$  and  $\Omega_{12}^b$

are the twisting and bending components of the relative rotation associated between the contact pair [15].

Per the constitutive contact model, a non-viscous damping force is added to particles in contact to dissipate kinetic energy. The damping force from a particle in contact,  $F_d$ , is defined in Equation (3.7) where  $\zeta$  is the damping ratio,  $F_r$  is the total residual force resulting from all contacts experienced by the particle,  $v$  is the velocity of the particle, and  $\bar{v}$  is the unit vector defining the direction of the velocity [18].

$$F_d = -\frac{\zeta F_r v}{\bar{v}} \quad (3.7)$$

Within YADE, deformable structures can be created and managed by taking into consideration elastic limits and conditions expressed in Equations (3.8)-(3.11) where  $A$  is the reference surface area, tensile and shear strengths are expressed by  $\sigma_n^t$  and  $\sigma_s^t$  respectively, and  $\varphi$  is the internal friction angle which is taken as the minimum friction angle between the two contacting particles. This angle of internal friction is a quantity that describes an aggregate's ability to resist shear due to the frictional resistance between the particles. In addition,  $I_b$  and  $I_t$  are the bending and twisting moments of inertia and the radius of contact is expressed by  $R$  and is the minimum radius of the particles in question [15].

$$\|F_n\| \leq \sigma_n^t A \quad (3.8)$$

$$\|F_s\| \leq F_n \tan \varphi + \sigma_s^t A \quad (3.9)$$

$$M_t \leq \frac{\sigma_n^t I_b}{R} \quad (3.10)$$

$$M_b \leq \frac{\sigma_s^t I_t}{R} \quad (3.11)$$

These formulations make up the general foundation of the contact model that is implemented in YADE and used throughout this research.

### 3.3 Simulation Construction in YADE

Simulations inside of YADE are built using object containers where one can store bodies, shapes, materials, and states for the entire scene. A shape, material, and specific state can all easily be defined using built-in commands and stored in their own respective containers. These properties are then called when creating a body. In this way, any characteristic of a body can be easily manipulated by simply changing the properties assigned to it. It is worth noting that bodies can manually be constructed and defined but this can limit their compatibility with YADE functions.

Each standard simulation in YADE incorporates four basic engines that drive the entire scene. The first of these engines simply resets all the forces at the beginning of each time step while the second engine performs a quick pass over all bodies to detect approximate collisions. Interactions are created and handled by the third engine if an exact collision is detected between any of the pairs that were identified in the second stage. Finally, the Newton integrator engine applies the contact forces, determines the accelerations, velocities, and updated positions of all the bodies. In addition, damping is finally incorporated in the Newton integrator engine as an artificial, numerical damping coefficient (default value of 0.2) which is used to dissipate energy caused by unrealistic behaviors in particles [33].

Outside of collisions a user may choose to invoke other forces, impose boundary conditions, or manipulate the scene in any way to suit the simulation. However, these additional loads and constraints should be set up and occur prior to the Newton integrator, else they will not be effective and will be reset at the beginning of the next step.

YADE has a variety of tools implemented that make it easy to handle constraints, forces, and motion. Constraints are easily set up by calling out the ID of a body and blocking any of the six degrees of freedom: translation and rotation in all three (x, y, and z) directions. Motion control is handled in a similar way where the ID of the body is called out and the state can be changed such as imposing a velocity. It is important to note that while the position of a body can be imposed, it is not recommended. YADE documentation notes that the foundations for their collision detection and contact law algorithms are based on velocities and using position to impose motion may result in errors [33].

Forces may also be introduced into the simulation by the user; however, this is done using functions that can be called from YADE's force container. As an example, some of the basic functions allow a user to add a force for a single time step, apply displacements and rotations on bodies, apply torques, and insert permanent forces into the simulation.

A more detailed simulation loop is shown in Figure 3.3 below that outlines the general structure for a time step in YADE.

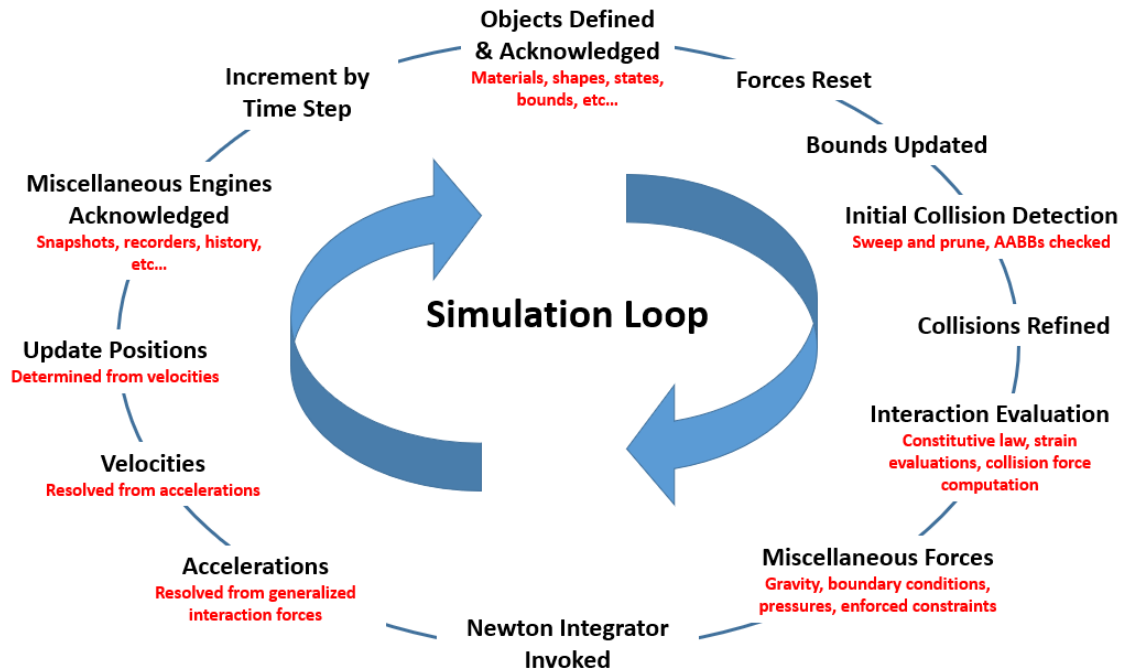


Figure 3.3: Detailed simulation loop for single time step in YADE

During the first check for collision YADE requires bound functors to be called upon. For each body that collision is requested on there must be a bound functor calling out that shape. For example, if interactions between spherical bodies are desired then there must be a functor that creates AABBs around spheres. Additional functors can be present in the simulation even without the shape as there is no penalty; however, if a functor is not present for a specific shape in the simulation then collision will effectively be turned off for bodies of that shape.

In addition, the third primary engine that handles the actual collisions must have geometry functors called upon that identify which shapes can collide. If two spheres are meant to contact, then there must be a functor telling the simulation to search for sphere-on-sphere collisions. A missing shape combination will allow bodies with those shapes to interpenetrate one another.

Under this same engine, physics functors must be selected that incorporate the non-geometrical properties of the interactions such as material, stiffness, friction, cohesion, etc. To

avoid errors in the behavior of the simulation it is critical that a proper physics functor is selected to reference the material combinations present in the simulation. Unlike the previous two functors, if a material pair is not referenced the simulation will terminate with an error as it will be unable to interpret the interaction behavior.

The final primary input that is required before the Newton integrator occurs is the selection of the constitutive law. YADE has a variety of these laws that can be used, but whichever is selected should be compatible with the geometries and material properties defined prior.

Beyond the standard scene construction, YADE also has a variety of features that can help a user control the simulation. For periodically tracking variables or running functions, an engine known as PyRunner can be added into the engine container. PyRunner enables a user to call and run YADE utilities or custom functions throughout the simulation. Using this tool, the iteration number, virtual time, or real simulation time can be used as the frequency at which the command will run. For example, PyRunner can be set up to print the total kinetic energy of the system every thousand iterations, every ten seconds of virtual time, or every ten seconds of real run time.

In addition, it may also be useful to import plot modules and view controls. The plot module gives access to creating graphs, tracking specified variables, and exporting data. Toggling different view controls in YADE will affect the visualization of the scene that is being constructed. This visualization can help serve as a check to a user where they can quickly verify parts of the simulation are behaving as intended. A snapshot engine can be used in conjunction with the view controls to take screenshots at specified time increments.

Simulations can be set up to run a predetermined number of steps before exiting or other stop conditions can be created. If necessary, checkpoints can be used to save the state of the simulation at a specific time and then can be started from that point in the future. This feature can

be useful if you want to vary different parameters of the system that may not be affected by the initial portion of the simulation.

### 3.4 Numerical Stability

When running DEM simulations one of the most vital features to consider is numerical stability. If a simulation is unstable it will typically terminate unexpectedly or explode which may be a result of poor timestep selection. When selecting a timestep it is critical not to make it too large even though it may improve simulation times. Large timesteps can cause interactions to be completely missed or can cause large interference between bodies. When two bodies overlap significantly, bodies very commonly accelerate wildly and erupt causing unexpected results in the scene. However, making the time step incredibly small will result in significant increases to the simulation time and, thus, it is crucial to make use of a critical timestep which is, in theory, the largest increment that can be imposed for a stable simulation.

In YADE this timestep can be expressed simply by Equation (3.12) where  $\Delta t_{cr}$  is the critical time step and  $\omega_{max}$  is the maximum eigenfrequency in the simulation.

$$\Delta t_{cr} = \frac{2}{\omega_{max}} \quad (3.12)$$

Defining the eigenfrequency in a simulation can be complex but consider a one-dimensional, single spring-mass system governed by Equation (3.13) where  $m$  is the mass of the system,  $k$  is the stiffness, and  $x$  is the displacement from equilibrium.

$$m\ddot{x} + kx = 0 \quad (3.13)$$

Under the example of a one-dimensional, spring-mass system, the harmonic oscillation can be expressed as a function of time according to Equation (3.14)

$$x(t) = A * \cos (\phi + \omega_{1D}t) \quad (3.14)$$

with  $A$  as the amplitude and  $\phi$  as the phase angle. In this scenario only one eigenfrequency is present due to the fact that there is only one mass which is shown in Equation (3.15).

$$\omega_{1D} = \omega_{max,1D} = \sqrt{\frac{k}{m}} \quad (3.15)$$

Substituting (3.15) into (3.12) yields Equation (3.16),

$$\Delta t_{cr,1D} = \frac{2}{\omega_{max,1D}} = 2\sqrt{\frac{m}{k}} \quad (3.16)$$

which is the critical time step for the single spring-mass system. The overall critical time step for a general mass-spring system is taken as the minimum critical time resulting from the system to be conservative. This timestep is expressed in Equation (3.17).

$$\Delta t_{cr} = \min \Delta t_{cr,sys} \quad (3.17)$$

Extrapolating this information to YADE's DEM engine requires accounting for the stiffnesses between each interaction. In determining the maximum eigenfrequency for the

simulation within YADE, a stiffness matrix,  $K_{ij}$ , can be defined on an individual particle basis by summing the contributions from all impacting collisions as expressed in Equation (3.18).

$$K_{ij} = \sum_m (k_{n,m} - k_{t,m}) n_i n_j + k_{t,m} \quad (3.18)$$

Each contact contains normal and tangential stiffnesses,  $k_{n,m}$  and  $k_{t,m}$  which are oriented relative to unit vector  $n_m$  (broken into  $i$  and  $j$  components in Equation (3.18)). In conjunction, Equations (3.17) and (3.18) result in a critical time step for a simulation using YADE. Note that that subscript  $m$  denotes the interactions each particle is involved with.

Provided that there is contact, the simulation should arrive at a reasonable time step under this formulation. However, if there is no contact the eigenfrequency will be zero which will result in an infinite time step. To solve this numerical singularity, YADE obtains a critical time step utilizing the defined microscopic particle properties to estimate a stiffness. In the previous definition, stiffnesses from both particles in an interaction are used to determine a relationship; however, that is neglected in this formulation. In addition, the number of contacts a particle experiences are also neglected.

Using continuum mechanics and explicit integration, YADE uses the formulation shown in Equation (3.19)

$$\Delta t'_{cr} = \min R_i \sqrt{\frac{\rho_i}{E_i}} \quad (3.19)$$

to estimate the time step. That is, the minimum radius particle,  $R_i$ , multiplied by the square root of that particle's density,  $\rho_i$ , divided by its stiffness,  $E_i$ . Under this formula, the elastic wave cannot be further than the minimum distance of the integration points which is set equal to the smallest radius particle [7].

As this formulation is an estimate, users may choose a safety coefficient of less than one for the simulation which is multiplied by the time step. This safety coefficient introduces an extra level of security into ensuring stability throughout the simulation. A small coefficient of say 0.1 will most likely result in a slow, but stable simulation as opposed to a value of 0.9 which would speed the process along but may cause instabilities. It is worth noting that the YADE documentation generally recommends a value of 0.3 for a reliable simulation.

### 3.5 Contact Tracking and Testing in YADE

Before developing a full simulation for YADE it was necessary to test that the functionality was working properly. Similar to the work done in [15], a simple simulation was created to ensure contacts, gravity, and rolling were all functioning as intended. The geometry setup for the simulation was a simple spherical particle sitting 0.03 meters above a fixed plate. The particle, of diameter 0.024 meters, was positioned 0.25 meters from the end of the plate which was one meter long. When started, the simulation would apply gravity at  $9.81 \text{ m/s}^2$  downward in the vertical direction allowing the sphere to drop until contact was made between the two bodies. The simulation setup and dimensions can be seen in Figure 3.4.

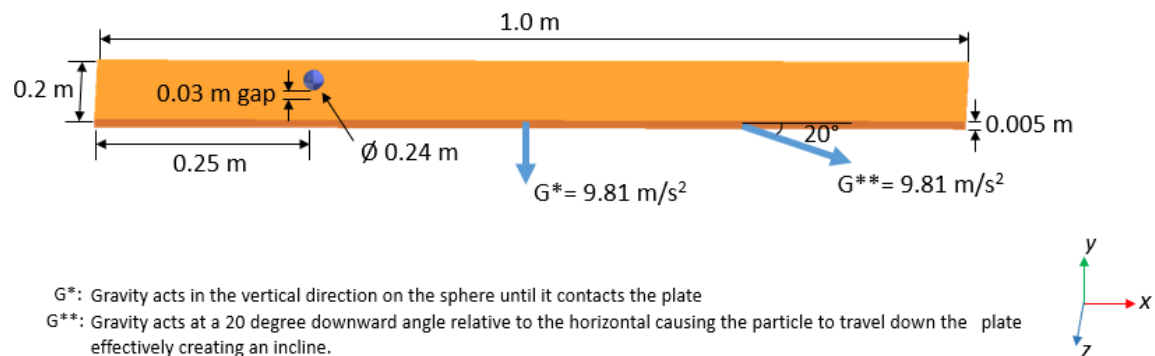


Figure 3.4: Sphere on plate contact tracking sample simulation setup

After contact, gravity would then be shifted by an angle of 20 degrees to simulate a sloped surface. The sphere would then rotate and/or slide down the plate depending on the defined material properties. To check the behavior of the sphere on the plate the simulation was run multiple times varying the particle friction angle.

While the sphere was moving along the plate, the circumferential displacement was output along with the total lateral displacement. As expected, when the friction angle was zero, the surfaces were perfectly smooth and all the displacement was translational. When the particle friction angle was changed to 10 degrees, the particle exhibited some circumferential displacement but was not equal to the total lateral displacement therefore implying the particle was beginning to roll in addition to sliding. Finally, when the friction angle was raised dramatically to a value of 90 degrees, the particle had near identical circumferential displacement as translational showing that the particle was purely rolling. Figures 3.5, 3.6, and 3.7 show plots of these observations. Also checked, the particle's change in displacement increased at each requested time output signifying acceleration direction was also working as intended. Therefore, contact and simple forces were working accurately within the framework of YADE as indicated by these contact tracking simulations.

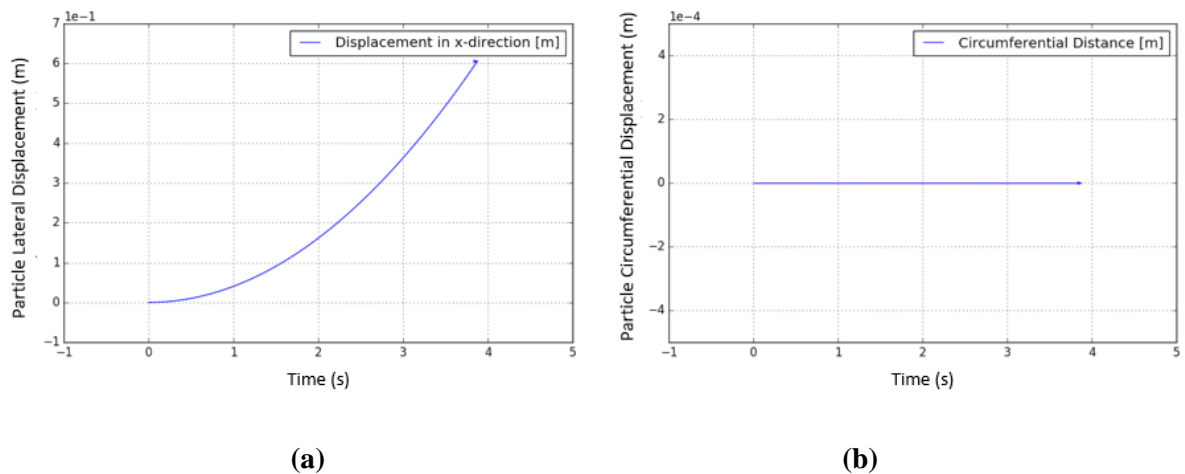


Figure 3.5: (a) Plot of particle's total lateral displacement versus (b) the particle's circumferential displacement with a particle friction angle of  $0^\circ$

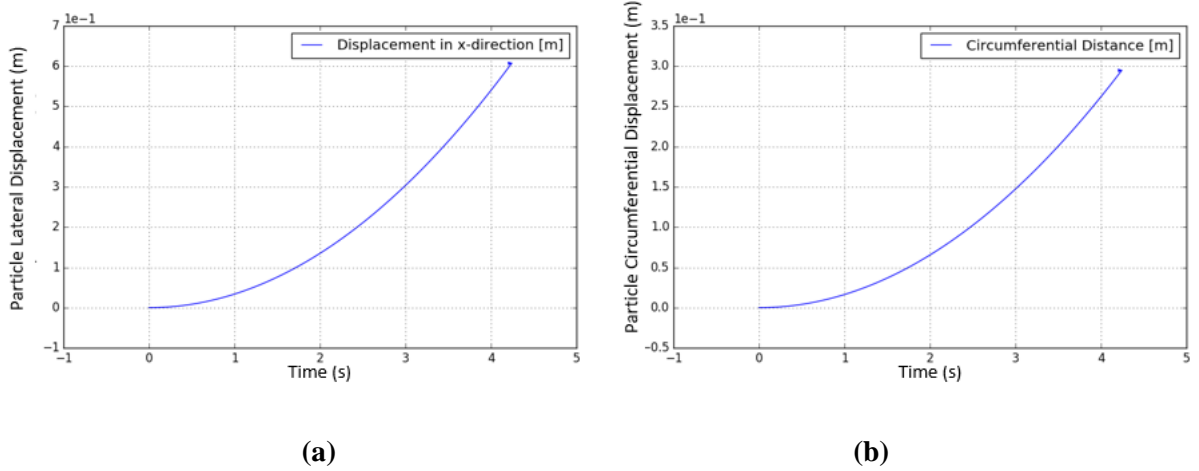


Figure 3.6: (a) Plot of particle's total lateral displacement versus (b) the particle's circumferential displacement with a particle friction angle of  $10^\circ$

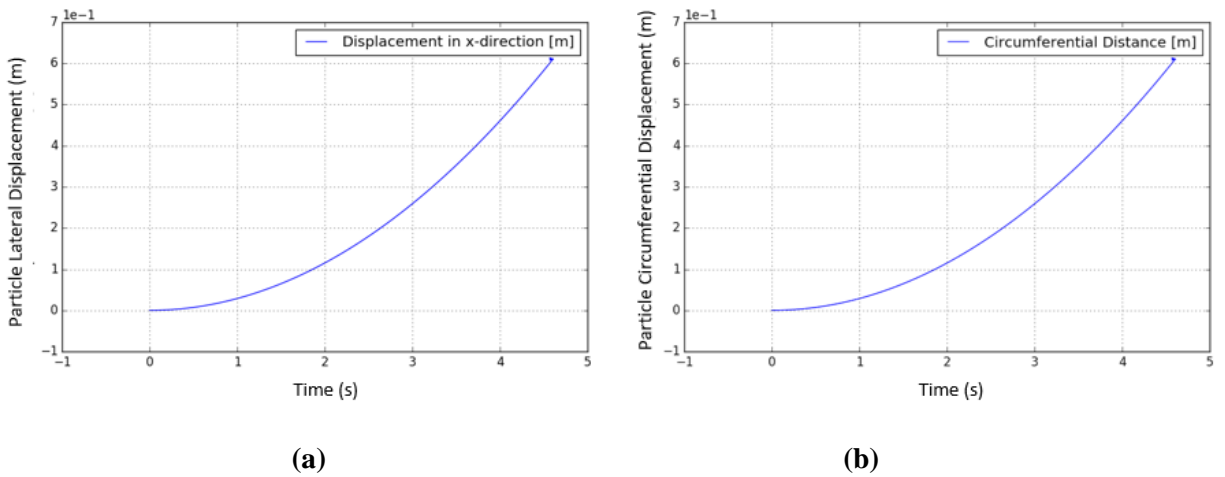


Figure 3.7: (a) Plot of particle's total lateral displacement versus (b) the particle's circumferential displacement with a particle friction angle of  $90^\circ$

For the primary simulations performed in this study, rolling resistance was not used, but it was tested and experimented with during the contact tracking simulations. A range of models were run varying the rolling resistance while holding the particle friction angle constant. As expected, when using the rolling resistance parameters properly the sphere showed less rotational

displacement than when rolling resistance was not used. However, for the purposes of this research, rolling resistance was not a key parameter being tested and properly quantifying the parameters was not feasible and therefore turned off for the final pullout simulations. Further research could be done on using and validating the proper values of rolling resistance to increase correlation to the physical test results. Additional information regarding rolling resistance and how it was explored early in the research can be found in Appendix A.

## 4. DEVELOPMENT OF NUMERICAL PULLOUT SIMULATION

### 4.1 Overview of Test Setup

In order to test the validity of running a DEM-based pullout simulation, the test was set up with the goal of duplicating the lab results presented in [38]. In [38], the pullout resistance of steel reinforcement is tested in primarily poorly graded aggregates, which makes the study an ideal starting point for correlating a numerical model.

In this chapter a more detailed explanation is laid out regarding the functionality of the script and the actual setup of each aspect of the tests. As stated previously, pullout simulation parameters were set up in such a way that it duplicated various aspects of the tests performed in [38] but could be easily manipulated for any reinforcement material, reinforcement geometry, or particle distribution.

One important distinction is that the particle sizes, strap dimensions, and the length of the box were scaled up by a factor of two to keep computation times low as the particle sample sizes could have easily reached into the millions without some form of scaling. Simulations were set up to replicate the lab tests in [38] that were performed at uniformity coefficients of 1.4, 2, and 3. The only minor difference here being that a uniformity coefficient of 1.0 was used in the simulations as opposed to 1.4 because it was actually possible to ensure all particles were the same size.

For a uniformity coefficient of 1.0 the normal pressures of 25 kPa, 41 kPa, 69 kPa, 103 kPa, and 138 kPa were applied to duplicate the lab tests. Under a uniformity coefficient of 2.0, the confining pressures of 25 kPa, 41 kPa, and 69 kPa were matched but 103 kPa and 138 kPa were ran in the simulations as well. Finally, simulations at a uniformity coefficient of 3.0 were run with pressures of 25 kPa, 41 kPa, and 69 kPa to match the tests from [38].

## 4.2 Virtual Pullout Box

The primary test apparatus in the simulation space was a simple box built by connecting six walls. The walls were completely rigid, fixed in space, and could be manipulated to any size. For the purposes of the simulation, the top of the box was initially removed to allow the particles to fall and accumulate inside the apparatus. Walls of the box were assigned an arbitrary thickness of 0.05 meters and collision was defined between the walls and the particles such that interactions between the two bodies could occur.

When pulling the reinforcement strap out of the apparatus during a lab test, a slit is required on the front face of the box; however, for the simulation, the front wall of the virtual box had no slit as interactions between the strap and the box were not specified ensuring the strap experienced no contact with the box when being pulled out.

According to ASTM D6706, the apparatus for a pullout test should at minimum be 610 mm long, 460 mm wide, and 305 mm deep; however, the standard goes on to state that the size should be adjusted such that the width of the box is at least six times the maximum particle size or twenty times greater than the D85 of the aggregate. In addition, the standard states the length of the box should be greater than five times the maximum size of the geogrid aperture [6]. It is worth noting that ASTM D6706 contains the standard test procedure and specifications for geosynthetic reinforced pullout tests rather than steel; nonetheless, the ASTM standard was still used as a minimum threshold for the apparatus used in this research.

To correlate to the lab tests performed in [38], several properties of the simulation were set to replicate the lab setup but were scaled up by a factor of two including the length of the strap. Due to the length of the strap being doubled, the length of the apparatus was also doubled to maintain a scale factor of two for the embedded reinforcement length. The width was set such that it exceeded the specifications in ASTM D6706 so as to minimize sidewall friction. For the specific simulations discussed in this research, the box was set to a length of 3.0 meters and a width of 0.6 meters. The height of the box was arbitrarily set such that in each simulation the

particles were completely encapsulated while falling and could not escape the box. Properties of each of the walls were set to emulate a standard steel and are shown in Table 4.1 along with the box dimensions.

Table 4.1: Pullout apparatus properties and dimensions

<b>Apparatus Length (m)</b>	3.0
<b>Apparatus Width (m)</b>	0.6
<b>Apparatus Height (m)</b>	Simulation dependent
<b>Material Model</b>	Steel
<b>Wall density (kg/m<sup>3</sup>)</b>	8000
<b>Wall friction angle (deg.)</b>	24.23
<b>Young's Modulus (Pa)</b>	2.00E+08
<b>Poisson's Ratio</b>	0.3

#### 4.3 Pullout Reinforcement Creation

The reinforcement in the simulation could be generated in one of two ways. The first way was through the creation of a deformable structure and is presented in [15]. This method starts off by creating nodes which establish the general layout and shape of the strap. Following that, cylindrical elements are used to connect each neighboring node. Each triangular hole that the cylindrical elements creates can be filled in with a PFacet element if desired to create solid geometries. A visual representation of this strap creation process is shown in Figure 4.1. Using this method, normal and shear cohesion properties are provided to the elements of the strap to ensure that they remain stuck together. This method for creating a soil reinforcement is highly configurable as it allows for complex, deformable bodies such as geosynthetic grid and membrane as shown in Figure 4.2.

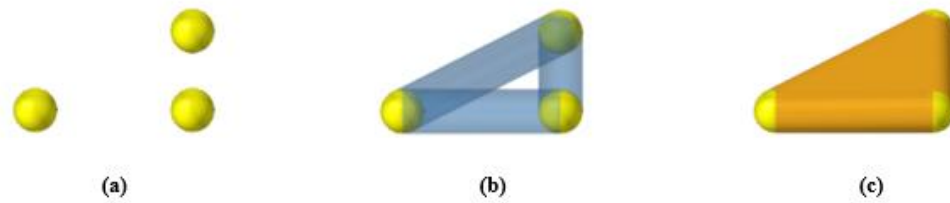


Figure 4.1: (a) Series of 3 node elements, (b) cylindrical elements that are created to tie the nodes together, and (c) PFacet elements optionally created to fill in the triangular connections

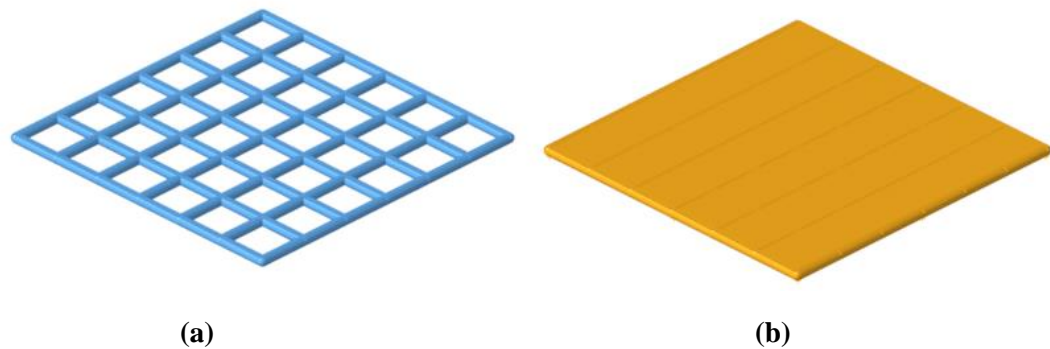


Figure 4.2: (a) Deformable grid created from nodes and cylindrical elements, (b) deformable plate created from a connected series of PFacet elements

The second method for creating the strap geometry is using a rigid wall and assigning it the appropriate material properties. This method is much easier to use and interact with but can only be used with simple shapes. For the tests performed in this research, this second method was used as the strap was a simple geometry and intended to be steel which would not experience large deformations as compared to a geosynthetic reinforcement.

The reinforcement to be matched from the lab tests in [38] was 1.5 meters long, 0.05 meters wide, and 0.004 meters thick with ribs spaced out along the length. The strap in the simulation was scaled up two times to be 2.4 meters long and 0.1 meters wide with a thickness of 0.008 meters.

Ribs were also created using rigid walls which were positioned along the length of the strap. The ribs extended through the strap with an even protrusion above and below the strap. One difference to note is that the ribs on the real strap in [38] were offset a small distance above and below the strap. The dimensions of each rib were parameterized in the simulation and set up as a function of the thickness or length of the strap as shown in Figure 4.3. The dimensions could be manipulated easily but were determined for these simulations based on measurements from a typical ribbed steel reinforcement specimen. It was assumed based on the figures shown in [38] that the strap used for the lab testing had roughly 32 ribs total (16 on the top and 16 on the bottom) embedded in the aggregate at the start of the tests. Thus, the numerical model was set to have 16 ribs protruding through the top and bottom of the strap. Table 4.2 summarizes the strap geometry along with the material properties used.

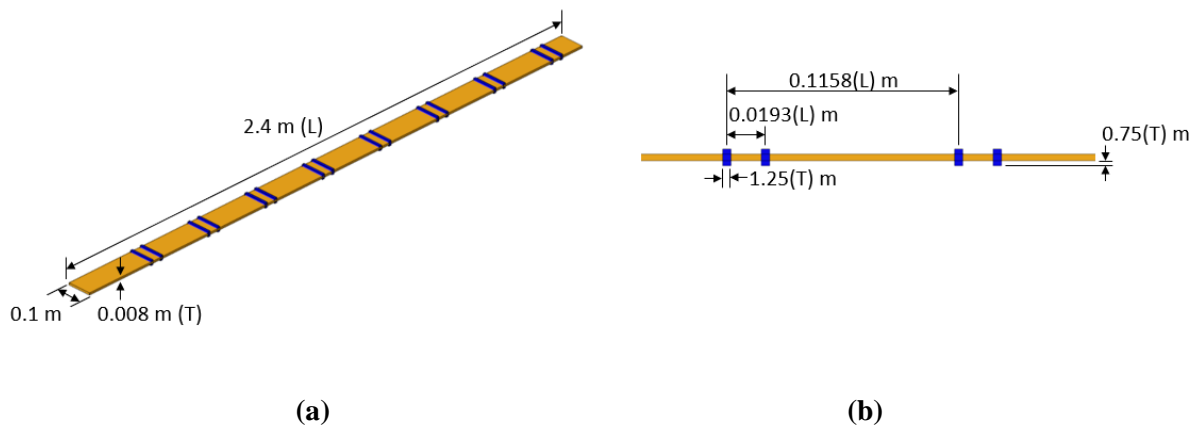


Figure 4.3: (a) Simulation strap with ribs and overall dimensions, and (b) dimensioning of ribs shown as a function of the overall length or thickness of the strap

Table 4.2: Reinforcement dimensions and properties

<b>Strap Length (m)</b>	2.4
<b>Strap Width (m)</b>	0.1
<b>Strap Thickness (m)</b>	0.008
<b>Number of Ribs</b>	16
<b>Rib Length (m)</b>	0.01
<b>Rib Width (m)</b>	0.1
<b>Rib Height* (m)</b>	0.006
<b>Material Model</b>	Steel
<b>Wall density (kg/m<sup>3</sup>)</b>	8000
<b>Wall friction angle (deg.)</b>	24.23
<b>Young's Modulus (Pa)</b>	2.00E+08
<b>Poisson's Ratio</b>	0.3

\*Rib height here is defined as the amount protruding above or below the thickness of the strap

#### 4.4 Application of Normal Load

In a typical lab test, a confining pressure is applied to the top layer of particles inside the box. This pressure application can be done in a variety of ways such as using an airbag and an actuator to apply an evenly distributed load [38]. In order to replicate this feature in the simulation, a rigid plate was created above the particle sample and dropped into the box. All degrees of freedom on the load plate were locked except for the vertical direction. Locking these degrees of freedom ensured the plate remained flat while falling and could not rotate in the occurrence of a collision. In the simulation this plate served several purposes in that it helped compress the particles into a relatively flat and compact arrangement as well as to apply the normal force.

The load plate was the same length and width of the box and applied a force over the entire area of the particle packing to give a uniform distribution of stress. The dimensions and properties of load plate are found in Table 4.3.

Table 4.3: Load plate dimensions and properties

<b>Load Plate Length (m)</b>	3.0
<b>Load Plate Width (m)</b>	0.6
<b>Load Plate Thickness (m)</b>	0.05
<b>Wall density (kg/m<sup>3</sup>)</b>	5500
<b>Wall friction angle (deg.)</b>	24.23
<b>Young's Modulus (Pa)</b>	2.00E+08
<b>Poisson's Ratio</b>	0.3

In the simulations, the particle samples of  $C_u = 1$  and  $C_u = 2$  were tested under equivalent normal stresses of 25, 41, 69, 103, and 138 kPa while the particle packing of  $C_u = 3$  was only tested at 25, 41, and 69 kPa.

#### 4.5 Pullout Particle Generation and Characteristics

##### 4.5.1 Particle Creation Script

Particle packings for the simulation were created using a separate script that was written in C++. Separating the pullout script from the particle creation allowed for additional control in creating the samples. The particle script used for the purposes of this research required several inputs including: diameters of each particle size requested, percent by number of each particle size, spacing to be enforced between each neighboring particle, and total number of particles to create.

Total number of particles was specified by inputting the amount required in each rectangular direction (x, y, and z). For example, the first particle packing used for simulations at  $C_u = 1$  was generated with 90 particles in the x-direction, 17 in the y-direction, and 22 in the z-direction for a total count of 33,660 particles in a packing.

When ran, the script would take the inputs and randomly generate a particle matrix to the specified size. Particles were spaced out at a minimum distance specified which was slightly

greater than the largest diameter particle to ensure no overlap occurred. In addition, each particle was given a small, random perturbation in the x, y, and z-directions. This offset was at maximum 20% of the spacing between particles. Therefore, the particle spacing was sufficiently big enough such that two particles of the largest diameter size could not overlap if each were to be perturbed the maximum distance closer to one another. The offset was added to stop particles from stacking perfectly on top one another during settlement and helped create an evenly distributed sample.

At each grid point, the particle generated was a random diameter that was specified in the inputs. Using the percent by numbers set for each diameter ensured that proper weighting was given to the chance of each particle size being generated. Note that the percent by number targets were usually not matched perfectly, but as the particle count increased it became more likely to obtain the exact, specified distribution. All particle packings used in this research were within 0.5% of the targeted percent by number for each diameter particle.

The final output of the script was a text file where each line was an individual particle's coordinates in virtual space and the particle's diameter. The text files for each particle packing were imported into the pullout scripts to instantly create the aggregate with appropriate size and positions.

#### 4.5.2 Particle Sample Packings and Properties

Particle samples were prepared for the simulation with the intention of duplicating the lab results presented in [38].

The first numerical sample generated was for a uniformity coefficient of one, single-sized particles, which is unobtainable in a lab test which explains why the lowest uniformity coefficient in [38] was technically  $C_u = 1.4$ . A quick examination of the gradation curve in [38] shows that the aggregate size for this test would have been around 12 mm. As stated in Section 4.1, to help reduce particle quantity, the simulation particles were doubled. Therefore, the initial particles were 24 mm in diameter and were the only size present for this packing. For a uniformity

coefficient of two, a second particle size was added in which was 12 mm. At a uniformity coefficient of three, a third particle size was added of 8 mm. A gradation curve for these samples was created and is shown below in Figure 4.4. Figure 4.5 shows a side-by-side comparison to the gradation curve from [38]. Additionally, specific characteristics relating to each sample from the numerical simulations are shown in Tables 4.4, 4.5, and 4.6.

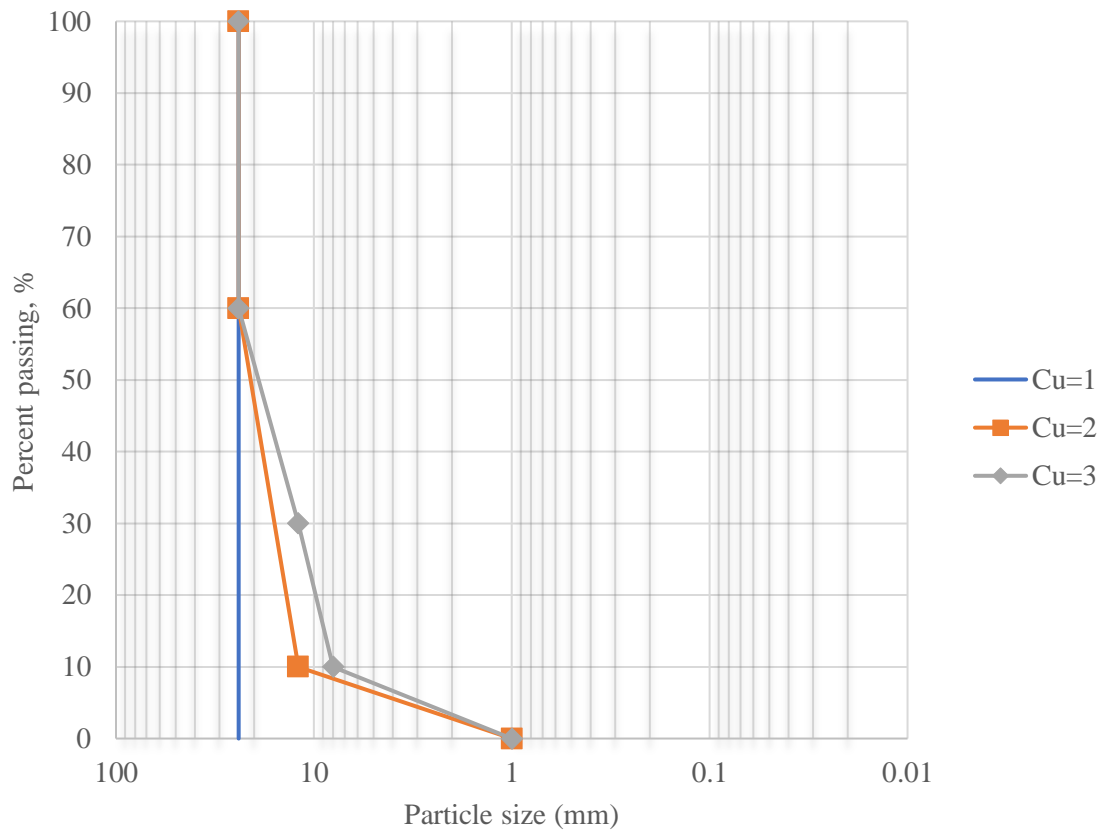


Figure 4.4: Gradation curve for samples tested

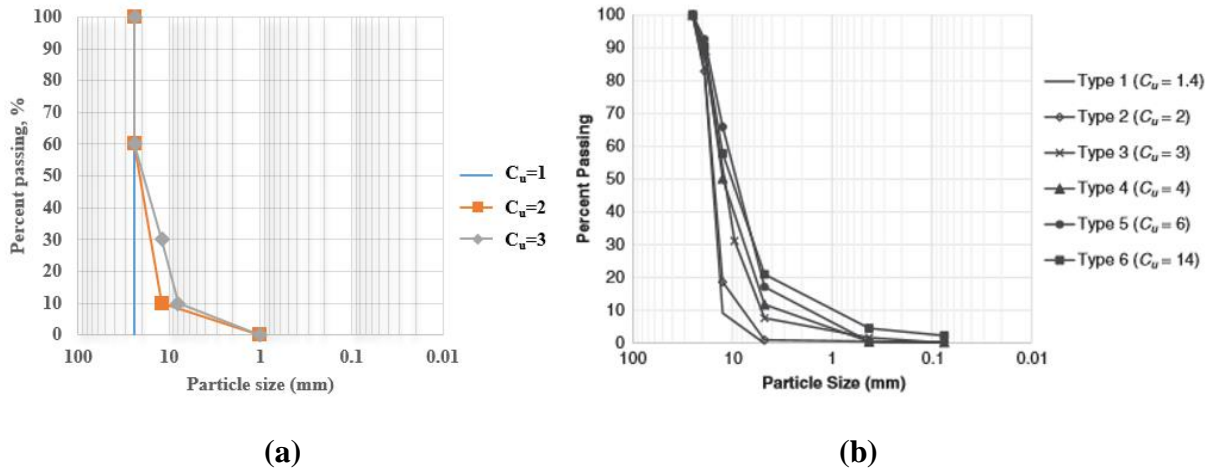


Figure 4.5: (a) Gradation curve for numerical simulation samples and (b) gradation curve for samples tested in [38]

Table 4.4: Particle sample characteristics for  $C_u = 1$

	Size 1	Size 2	Size 3
<b>Particle Size(s) [mm]</b>	24	N/A	N/A
<b>Percent by Weight [%]</b>	100	N/A	N/A
<b>Percent by Number [%]</b>	100	N/A	N/A
<b>Particle Spacing [mm]</b>	33.2		
<b>Number of Particles</b>	67,320		

Table 4.5: Particle sample characteristics for  $C_u = 2$

	Size 1	Size 2	Size 3
<b>Particle Size(s) [mm]</b>	24	12	N/A
<b>Percent by Weight [%]</b>	90	10	N/A
<b>Percent by Number [%]</b>	53.16	46.84	N/A
<b>Particle Spacing [mm]</b>	33.2		
<b>Number of Particles</b>	119,340		

Table 4.6: Particle sample characteristics for  $C_u = 3$ 

	Size 1	Size 2	Size 3
<b>Particle Size(s) [mm]</b>	24	12	8
<b>Percent by Weight [%]</b>	60	30	10
<b>Percent by Number [%]</b>	10.63	42.02	47.35
<b>Particle Spacing [mm]</b>	33.2		
<b>Number of Particles</b>	400,860		

In addition, general properties entered into the simulation attempted to replicate the limestone used in [38]. However, without the actual material, Young's Modulus, Poisson's Ratio, and density values were simply estimates and are shown in Table 4.7. In regard to the density, a reasonable range for limestone is 2,300-2,700 kg/m<sup>3</sup>. Typically, non-crushed limestone is on the higher end of this range, but the aggregate used in the lab test was crushed and so the lower end of the spectrum, 2,300 kg/m<sup>3</sup>, was selected for the simulations.

Selecting the particle friction angle was a more involved process that is discussed in more detail in Section 4.6.

Table 4.7: General particle properties

<b>Young's Modulus (Pa)</b>	5.E+06
<b>Poisson's Ratio</b>	0.3
<b>Density (kg/m<sup>3</sup>)</b>	2300
<b>Particle Friction Angle [Deg.]</b>	40

#### 4.6 Calibration of Particle Samples

Section 4.5.2 goes into the details of properties used to prepare a particle sample that replicated the crushed limestone aggregate used in [38]. The properties that were input into the simulation were microscale properties as required by the DEM formulation. In comparison, geotechnical lab testing presents macroscale properties for aggregates due to the response being

measured as a system rather than on an individual particle basis. Therefore, the microscale properties for the simulation were not directly comparable to the macroscale properties measured in lab testing. Selecting the correct particle friction angle for the simulation was critical to having comparable results, and thus it was necessary to perform a triaxial compression test with the samples to verify that the packings were properly calibrated.

In [38], friction angles are presented as 46-49° for all backfill materials; however, this value is a macroscale friction angle,  $\phi$ , that is determined from standard triaxial compression tests as defined in ASTM D7181 [7]. Therefore, a simple simulation was created using one of YADE's controllers that performed triaxial compression tests on the virtual samples.

At the start of the triaxial simulation, the particle packing was imported and given a target porosity. During phase one, consolidation occurred and a confining pressure was applied to the specimen in all directions until the mean stress was less than 0.1% different than the specified goal. Once consolidation completed, phase two began which adjusted the porosity because it would be above the target value. To do this porosity adjustment, the simulation was set up to reduce the friction angle of the material in small increments for additional compaction which, in turn, reduces the porosity. After each reduction in friction angle the porosity is checked until it reaches the target. After the porosity adjustment, the specimen was reconsolidated back to the stress goal from the first phase.

Finally, a final phase was used to handle the deviatoric loading. The friction angle of the material was reset to the initial value before phase two occurred. Then, a stress control was imposed in two directions (x and y-directions in this case) while a strain rate was imposed on the third direction (z-direction). The strain rate that was imposed was extremely small to ensure the triaxial test was quasistatic. Using the data from the triaxial test, the confining stress was plotted against the peak axial stress to yield Mohr's circle. From there, a Mohr-Coulomb failure envelope was plotted and macroscale friction angle was obtained. This strategy was used to calibrate the material and ensure that the correct microscale friction angle was used such that it correlated to

the proper macroscale friction angle found in [38]. Figure 4.6 below shows the triaxial simulation at four different stages.

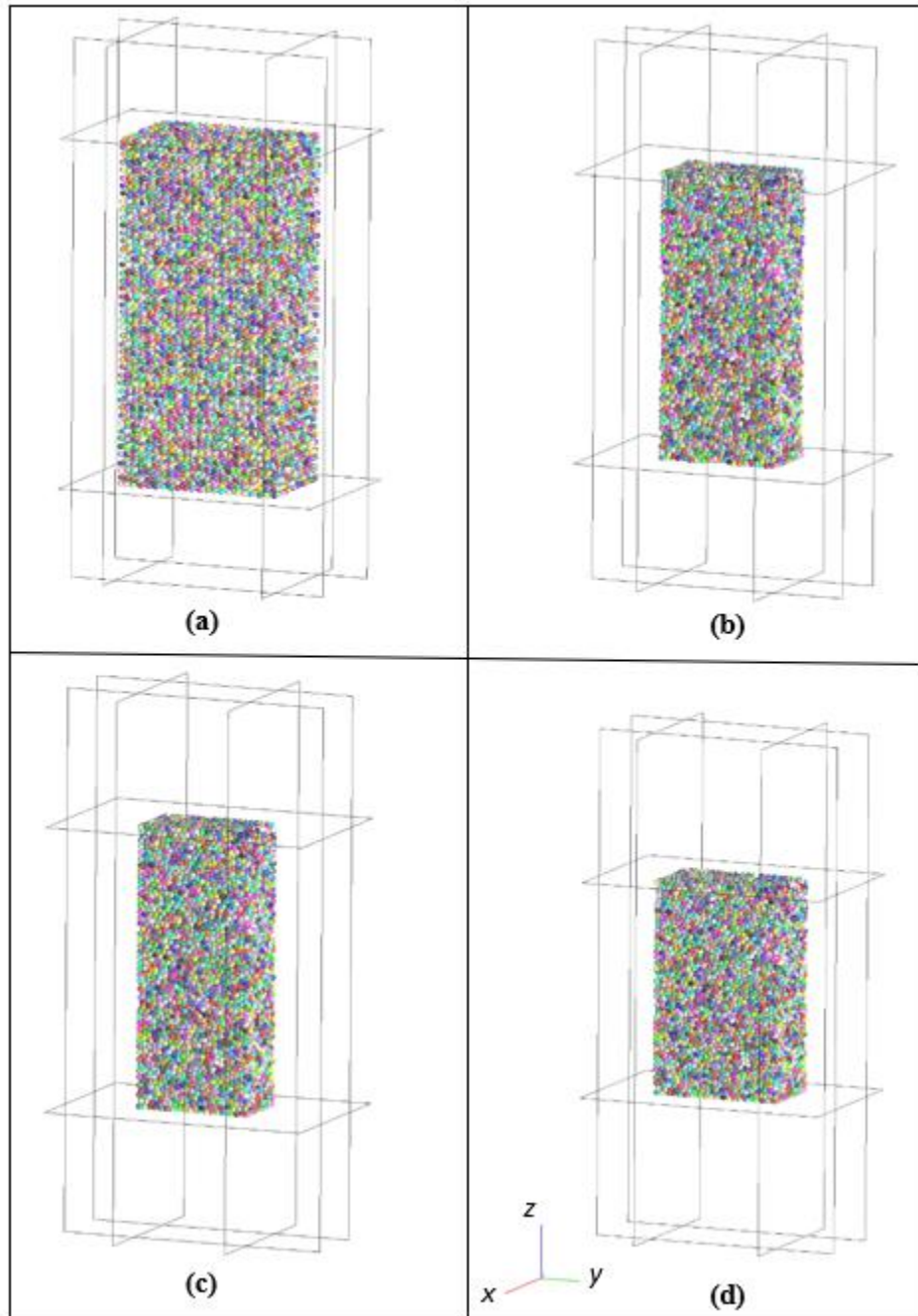


Figure 4.6: (a) Loose particle packing at initial stage of triaxial simulation, (b) particle sample after initial consolidation phase, (c) simulation after target porosity has been met and reconsolidation occurs, and (d) the final state of the particle packing after imposed strain rate

To set up the experimental simulation correctly a target porosity value was calculated out of the backfill data from [38]. The maximum dry unit weight reported for a  $C_u = 1.4$  was 15.8 kN/m<sup>3</sup>. Then, assuming a specific gravity,  $G_s$ , of 2.7 for the limestone and using Equation (4.1)

$$V_s = \frac{W_s}{G_s \gamma_w} \quad (4.1)$$

the volume of solids,  $V_s$ , was calculated out to be 0.5965 m<sup>3</sup>. This formulation uses the weight of the solids,  $W_s$ , as 15.8 kN (assumes 1 m<sup>3</sup> volume) and the specific weight of water,  $\gamma_w$ , as 9.81 kN/m<sup>3</sup>.

Equation (4.2) was then used to determine the volume of voids,  $V_v$ , assuming the material was filling up a one cubic meter box.

$$V_v = V_T - V_s \quad (4.2)$$

The porosity,  $\eta$ , was then be calculated as a ratio of the volume of voids to the total volume; Equation (4.3).

$$\eta = \frac{V_v}{V_T} \quad (4.3)$$

Therefore, the target porosity used for the triaxial simulation was 40.35%.

The simulation was run with 10 kPa as the target confinement pressure,  $\sigma_3$ , and the microscale particle friction angle,  $\varphi_m$ , was varied until the macroscale friction angle,  $\varphi$ , was found to be between the range of 46-49°.

Eventually, using a microscale friction angle of 40 degrees resulted in a peak axial stress,  $\sigma_1$ , of 65.24 kPa. Using Equation (4.4)

$$\varphi = \sin^{-1} \frac{(\sigma_1 - \sigma_3)}{(\sigma_1 + \sigma_3)} \quad (4.4)$$

the resulting macroscale friction angle was then determined as 47.24 degrees. Additionally, Mohr's Circle for the triaxial simulation is shown in Figure 4.7. Using this procedure, the samples were calibrated and a microscale particle friction angle of 40° was defined for all simulations.

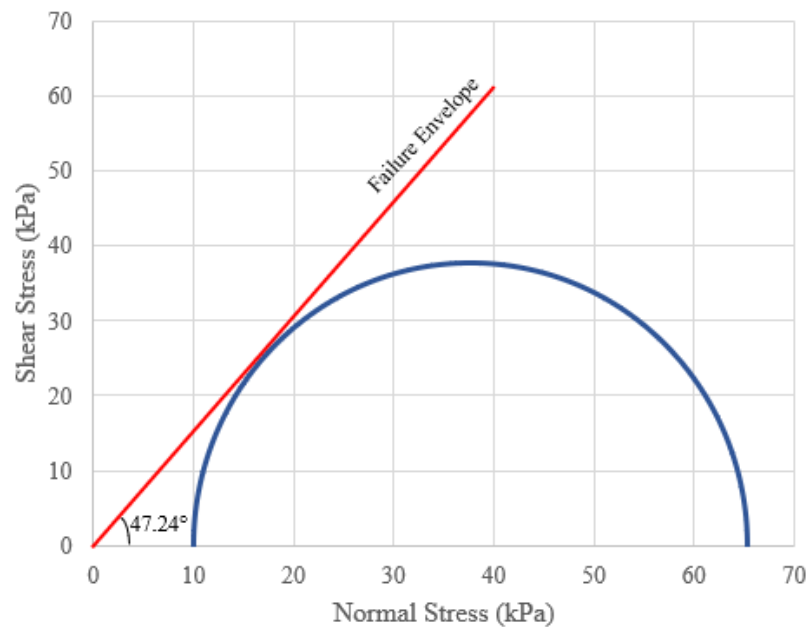


Figure 4.7: Mohr's Circle resulting from triaxial simulation results

#### 4.7 Load Correction

For each simulation, a load correction was applied to the overall normal stress in order to obtain equivalent stresses to those applied in [38]. The load correction accounts for the additional

pressure the load plate applied due to its mass and the additional pressure applied by the difference in particle size and volume.

This correction was a very rough calculation and took into consideration several assumptions. First, it assumed there was no additional load being imparted by the airbag used to apply to the normal stress in the tests from [38]. Secondly, it neglected packing arrangement and density and just assumed the particles take up a perfectly rectangular cuboid of space. The load correction,  $LC$ , was simply defined as the sum of the pressure applied by the load plate,  $P_{lp}$ , and the pressure difference between half the simulation particle packing,  $P_{sp}$ , and half the lab test particle packing,  $P_{tp}$ , as shown in Equation (4.5).

$$LC = P_{lp} + (P_{sp} - P_{tp}) \quad (4.5)$$

All these pressures were calculated in a similar way by using the assigned densities,  $\rho$ , and volumes,  $V$ , to solve for mass,  $m$ . Then, mass was multiplied by the acceleration due to gravity,  $a_g$ , to obtain a force,  $F$ , which was divided by the area it acts over,  $A$ , to obtain the pressure being applied,  $P_x$ . as expressed by Equations (4.6)-(4.8).

$$m = V\rho \quad (4.6)$$

$$F = ma_g \quad (4.7)$$

$$P_x = \frac{F}{A} \quad (4.8)$$

For the baseline simulations with a uniformity coefficient of one the load correction amounted to 8 kPa which was subtracted from the base normal stresses of 25 kPa, 41 kPa, 69 kPa, 103 kPa, and 138 kPa. To remain consistent between test sets, this same load correction was applied to the simulations done at higher uniformity coefficients.

#### 4.8 Numerical Pullout Test Procedure

The first step in setting up the DEM pullout simulation was generating the particle sample which was done according to Section 4.5. Afterwards, inputs were entered into the script via a text file of particles locations and sizes and defining dimensions and material properties.

Once the apparatus size had been decided, a packing of particles was imported and positioned a few millimeters from the base of the box. Above the first packing of particles, the strap geometry was generated followed by a second packing of particles. Everything was generated inside the enclosure of the box and initially nothing was touching to ensure there were no instabilities in the setup. With this initial setup, both particle packings and the strap fell into the box under the force of gravity ( $-9.81 \text{ m/s}^2$ ). Figure 4.8 shows a setup of the simulation before the particles and reinforcement begin to compact.

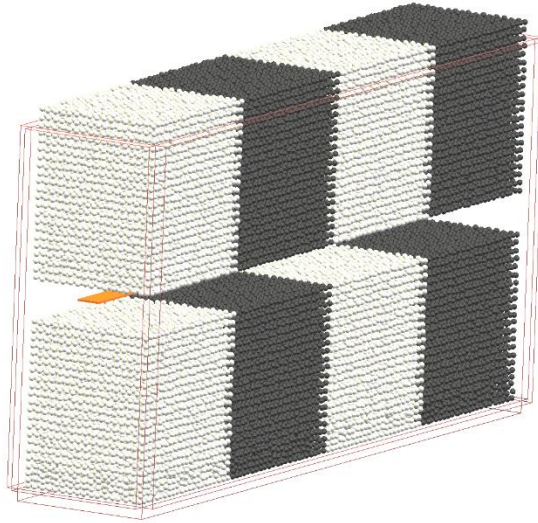


Figure 4.8: Simulation setup prior to settling

While falling, the script began running a *settling* function that checked the total kinetic energy of the system every 1,000 iterations. The kinetic energy of the simulation was calculated using a utility that is predefined in YADE and follows the formulation shown in Equation (4.9). This formulation considers the mass of each body,  $m_i$ , the velocity of the center of mass of the body,  $\mathbf{v}_i$ , the angular velocity of the body,  $\boldsymbol{\omega}_i$ , and its corresponding inertia tensor,  $\mathbf{I}_i$ . Thus, the total kinetic energy of the system,  $KE_{sys}$ , is given by:

$$KE_{sys} = \sum \frac{1}{2} (m_i \mathbf{v}_i^T \mathbf{v}_i + \boldsymbol{\omega}_i^T \mathbf{I}_i \boldsymbol{\omega}_i) \quad (4.9)$$

There were two kinetic energy thresholds defined that the *settling* function constantly checked. When the simulation fell below the first threshold, the simulation introduced a new function called *normLoad* that handled the application of the stress across the top layer of particles. At the second threshold, a third function called *pull* occurred which is responsible for pulling the reinforcement strap out of the box. In addition, the script also started tracking and

recording data when the strap was being pulled out. These thresholds were a way of making sure that the particle packing was fully settled and not still experiencing motion. Having settled particles is critical before pulling out the strap as having motion still occurring will introduce unwanted noise to the simulation and yield unreliable results.

When the normal load was applied, a wall was created above the sphere packings that fell onto the top layer and applied a constant, permanent load equal to the value input at the beginning of the simulation. After resettling with the normal load applied the reinforcement was removed from the box via a prescribed velocity. While in the pullout phase, displacement of the strap in the longitudinal direction (z-direction in the simulation) was recorded and plotted versus the resulting normal force required to pull the strap out longitudinally (force in z-direction). Additionally, all particle forces and rotations were tracked and recorded. The strap was pulled out until reaching a prescribed displacement which concluded the pullout test. Force and displacement data for the reinforcement as well as all particle data that was requested was saved upon completion which was used for post-processing results. Figure 4.9 shows the test after settling had occurred and after the pullout had completed.

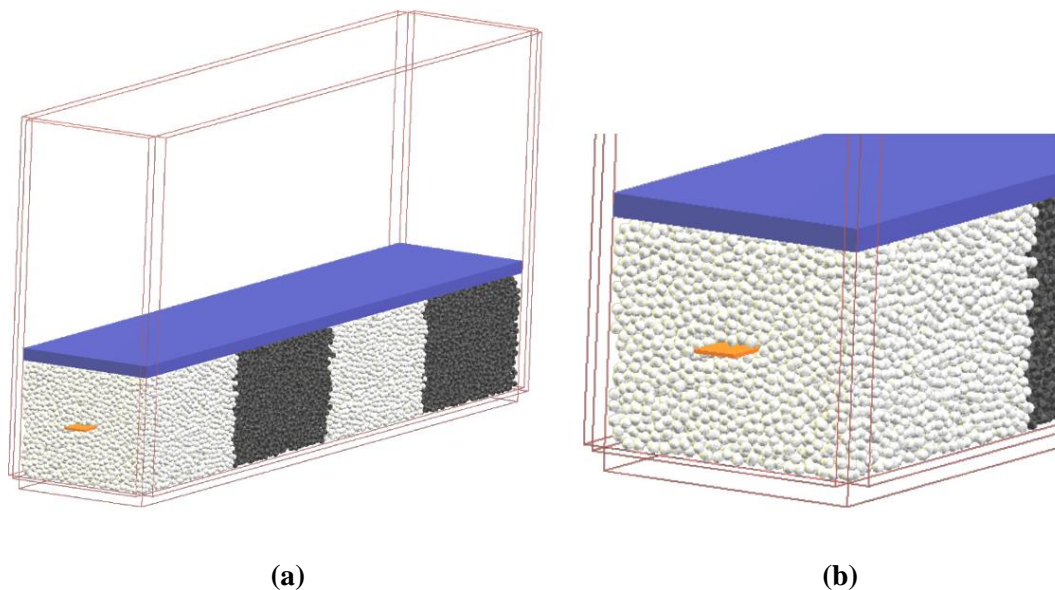


Figure 4.9: (a) Simulation after settling and strap pullout completes, and (b) zoomed in image of strap after being pulled out 80 mm

## 5. NUMERICAL PULLOUT TEST RESULTS AND DISCUSSION

### 5.1 Test Results with a Uniformity Coefficient of One

Using the particle characteristics presented in Table 4.4, a series of five numerical simulations were performed at a uniformity coefficient of one. To remove variability, the particle packing at each pressure was identical which meant particles settled identically at each pressure level. The only variation between each simulation was the normal stress which was run at 25 kPa, 41 kPa, 69 kPa, 103 kPa, and 138 kPa. Table 5.1 shows the entire list of parameters used to set up the simulation and Figure 5.1 shows the simulation after settling.

Table 5.1: Overall simulation parameters

<b>Applied Pressures (kPa)</b>	<b>25, 41, 69, 103, 138</b>
<b>Pressure Adjustment (kPa)</b>	<b>8</b>
<b>Initial Kinetic Energy Threshold* (J)</b>	<b>2</b>
<b>Final Kinetic Energy Threshold** (J)</b>	<b>0.025</b>
<b>Pullout Distance (m)</b>	<b>0.08</b>
<b>Time Step Safety Coefficient</b>	<b>0.1</b>

\*Initial kinetic energy threshold is when the load plate is introduced into the simulation environment

\*\*Final kinetic energy threshold is when the simulation is considered settled and begins pulling the strap out

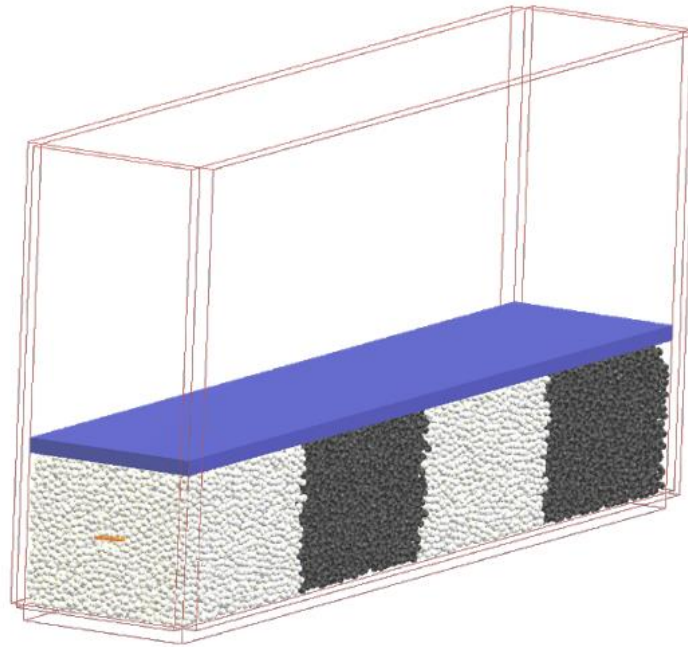


Figure 5.1: Numerical pullout test visualization for  $C_u = 1$

From the simulations, the total force the strap was experiencing in the longitudinal direction was plotted against the displacement of the strap. When plotted, the force at which the curve plateaus was considered the pullout resistance. Figure 5.2 shows the plot of pullout test results for a uniformity coefficient of one.

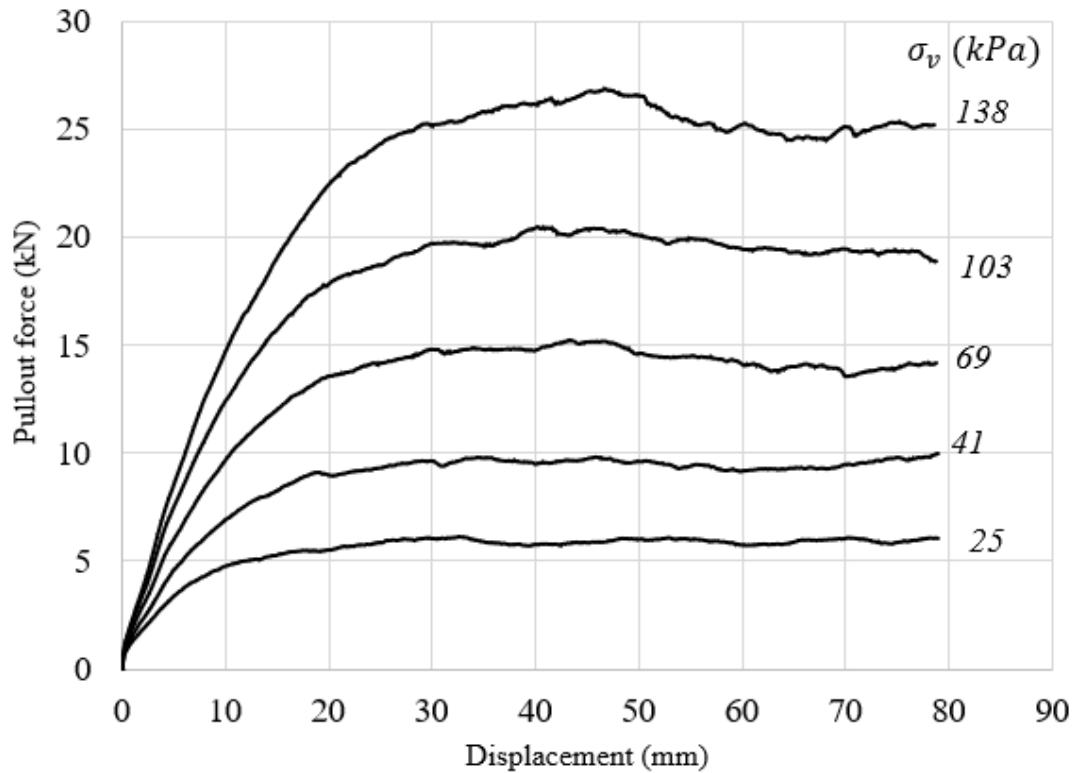


Figure 5.2: Plot of pullout force versus strap displacement for  $C_u = 1$

## 5.2 Test Results with a Uniformity Coefficient of Two

The similar spectrum of simulations was run for a uniformity coefficient of two. The only major difference being the particle packing characteristics which were previously defined in Table 4.5. The parameters specified in Table 5.1 are applicable to the simulations for a uniformity coefficient of two. As was the case in Section 5.1, the particle packing used for a uniformity coefficient of 2 was identical at each pressure.

Figure 5.3 shows a visualization of the simulation after settling and Figure 5.4 shows the pullout force versus displacement for the various normal confinement pressures.

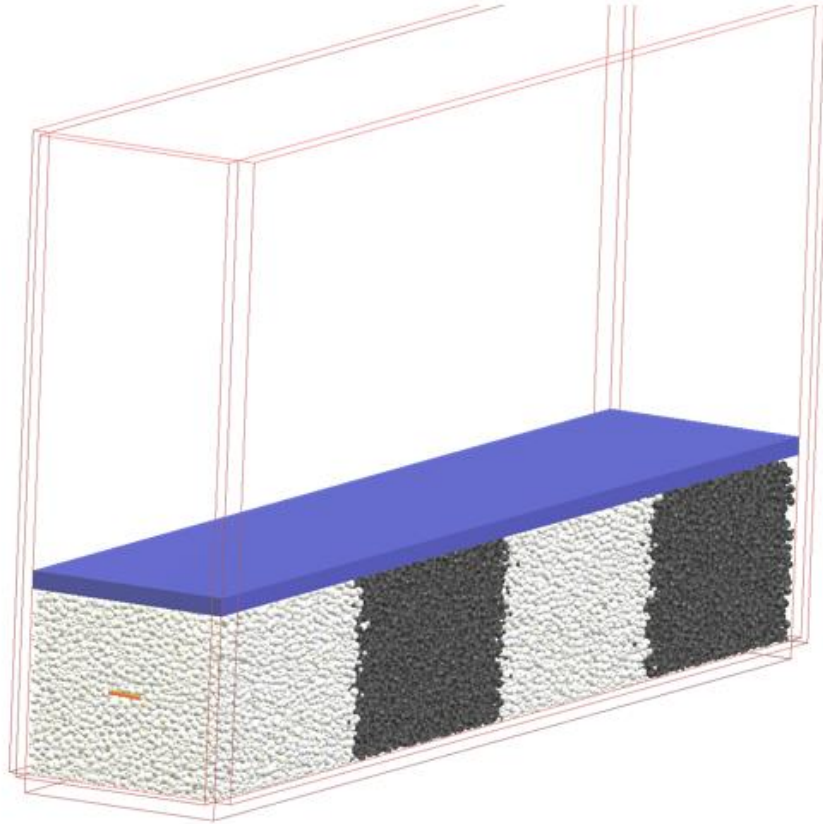


Figure 5.3: Numerical pullout test visualization for  $C_u = 2$

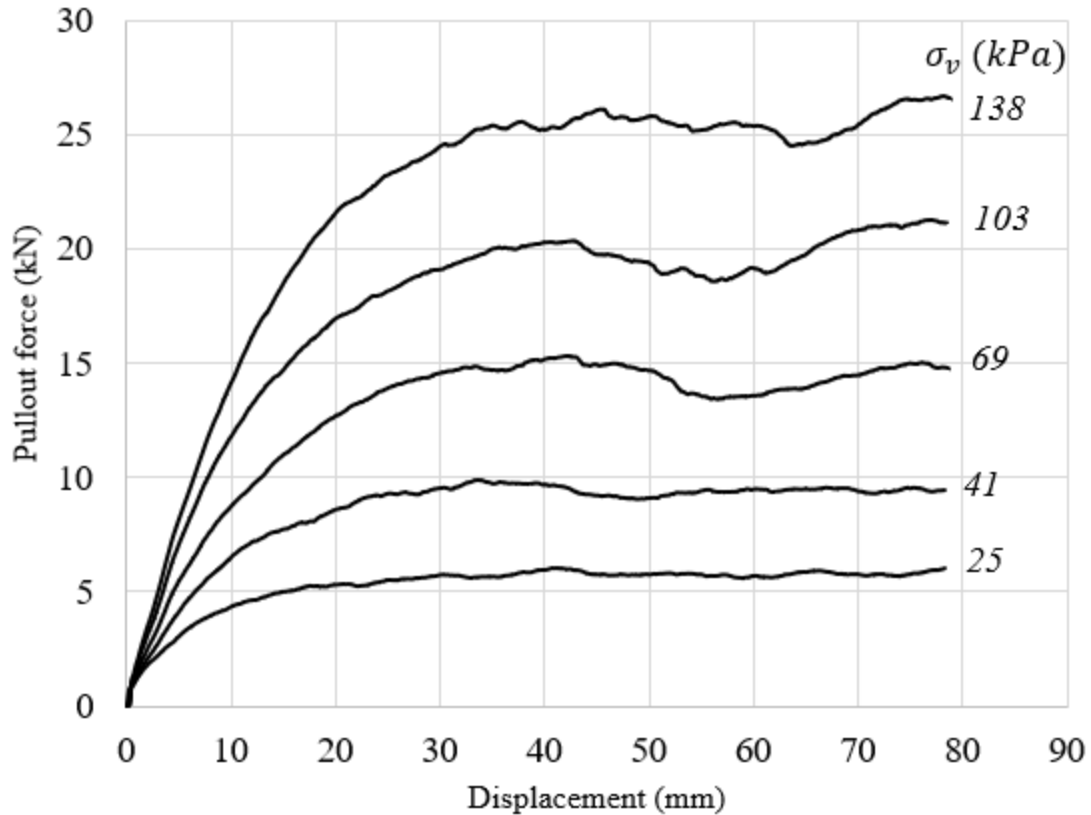


Figure 5.4: Plot of pullout force versus strap displacement for  $C_u = 2$

### 5.3 Test Results with a Uniformity Coefficient of Three

The final set of simulations ran were at a uniformity coefficient of three. The simulation setup was identical to the previous two series of results with the major change being different particle characteristics as defined in Table 4.6 previously. As stated for the other two series of tests, the particle packing was identical at each successive pressure increase and therefore there was no variability in how the particles settled at each pressure.

In addition, due to long run times with 400,000 particles, the simulations were terminated at a pullout distance of 70 mm and runs were only done at normal stresses of 25, 41, and 69 kPa. A segmentation error occurred on the virtual machine during the 41 kPa run which caused the simulation to terminate at a pullout distance around 62 mm, but this was still more than enough

distance to capture a pullout resistance trend. Figure 5.5 shows the simulation post particle settling and Figure 5.6 below shows the plot of results for these three tests.

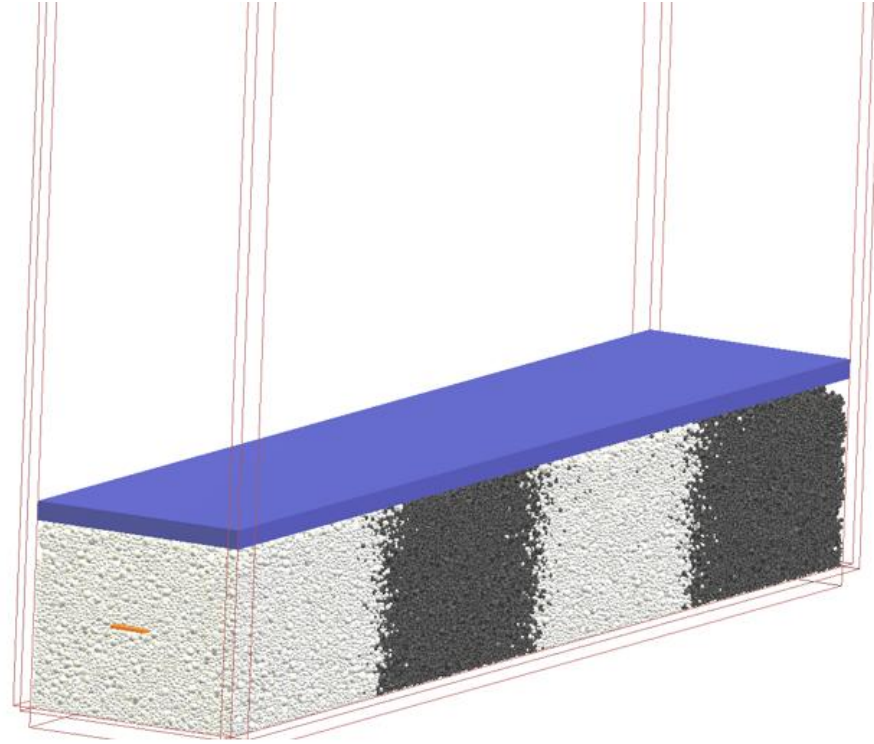


Figure 5.5: Numerical pullout test visualization for  $C_u = 3$

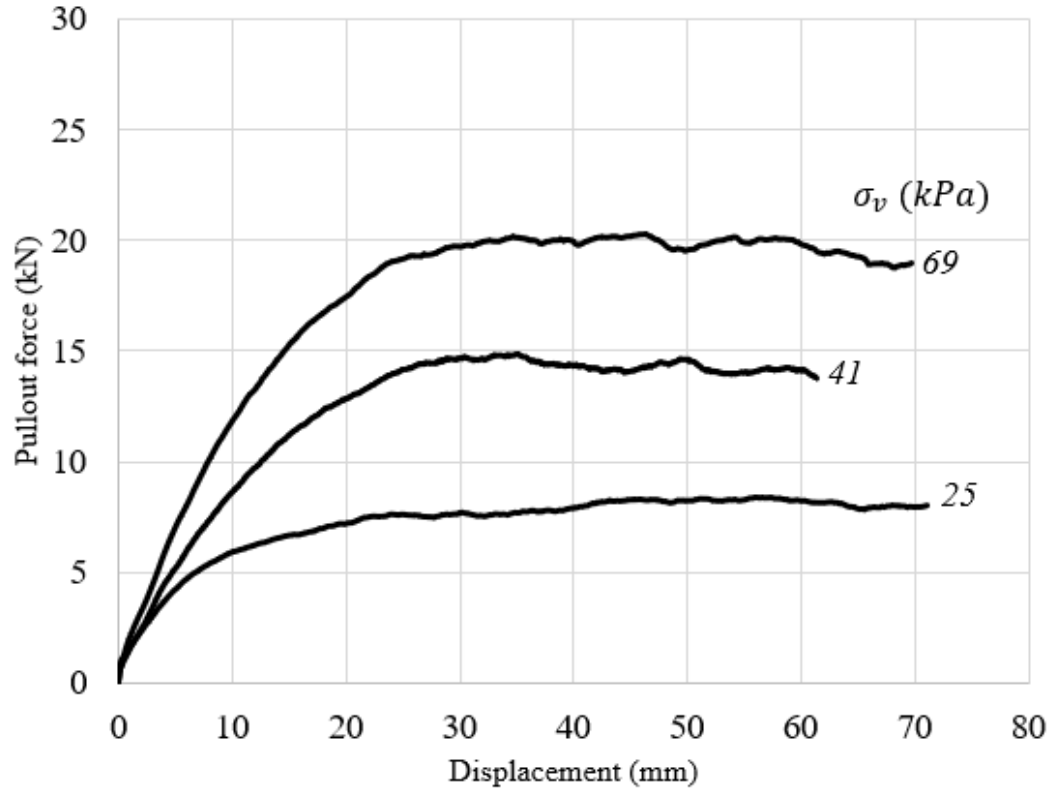
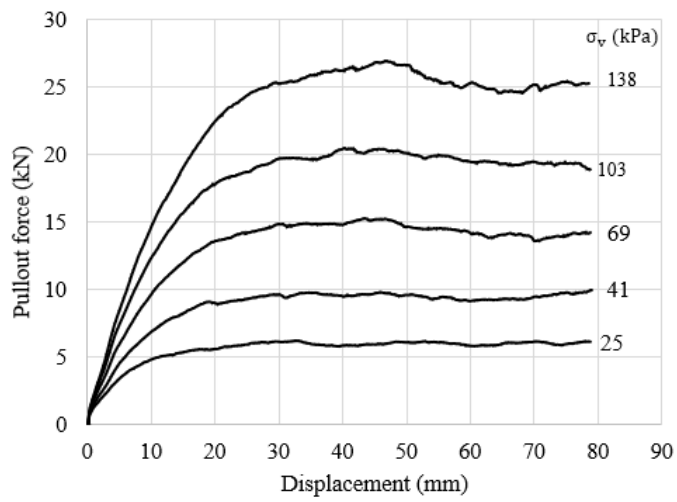


Figure 5.6: Plot of pullout force versus strap displacement for  $C_u = 3$

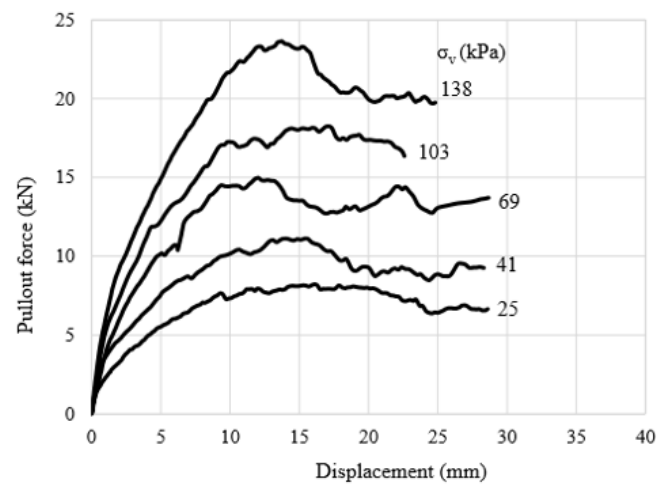
#### 5.4 Comparison to Physical Tests

The three series of simulations ran in Sections 5.1-5.3 were all set up with the goal of duplicating results found in lab tests. Figures 5.7, 5.8, and 5.9 show a side-by-side comparison of the results presented above along with the corresponding lab data collected in [38]. Note that the scales have small differences as the plots from [38] are unedited and cropping the simulation plots accordingly would result in excluding data.

One minor difference to point out is in Figure 5.7(b) the targeted uniformity coefficient was 1.0 but due to the physical limitations of the experiment only achieved an actual uniformity coefficient of 1.4. The simulation setup used the actual target of 1.0 as it is much easier to create a particle packing with one particle size in virtual space. Nonetheless, the results match up fairly well even with the minor difference and error between the two is more likely for other reasons which will be discussed more later.

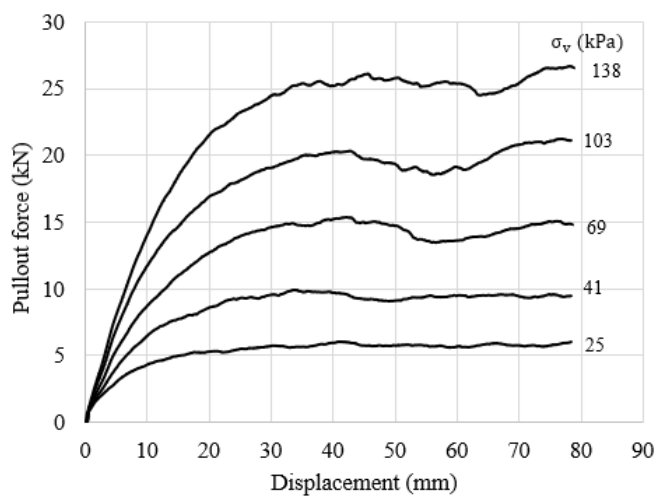


(a)

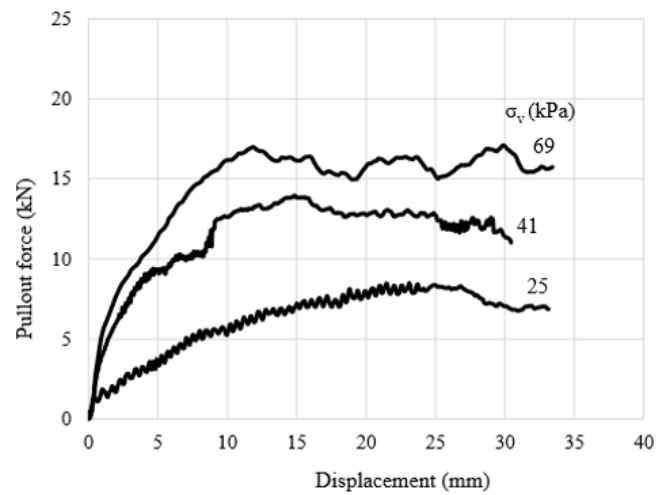


(b)

Figure 5.7: (a) Simulation pullout test results with  $C_u = 1$ , and (b) physical pullout test results with  $C_u = 1.4$  from [38]



(a)



(b)

Figure 5.8: (a) Simulation pullout test results with  $C_u = 2$ , and (b) physical pullout test results with  $C_u = 2$  from [38]

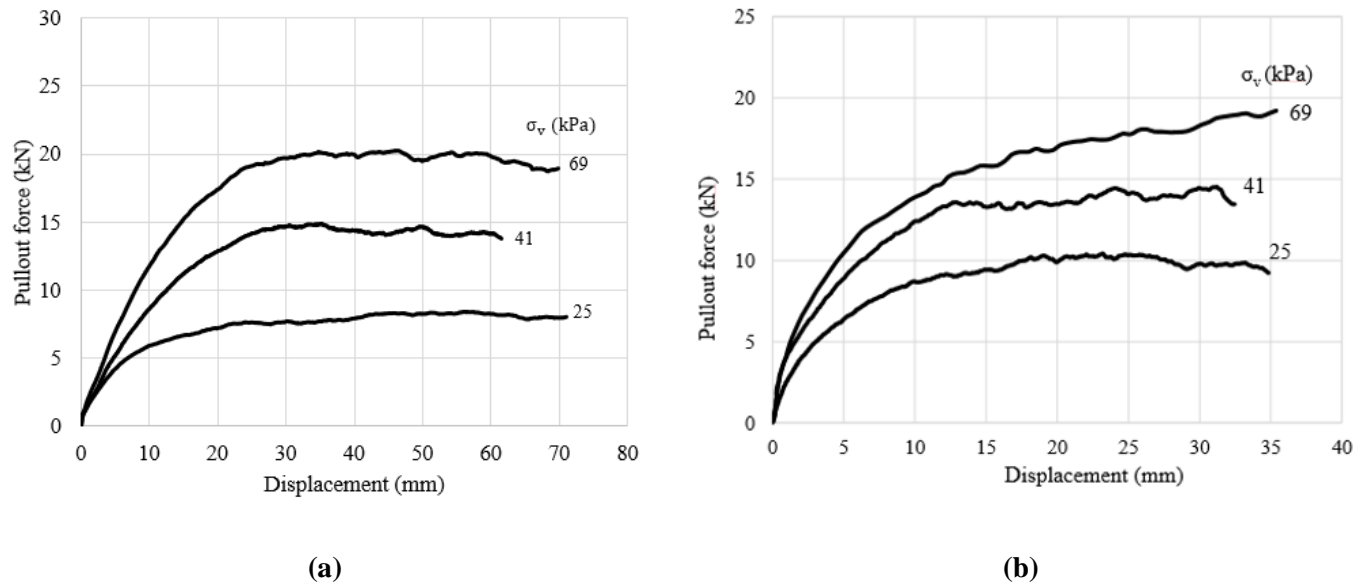


Figure 5.9: (a) Simulation pullout test results with  $C_u = 3$ , and (b) physical pullout test results with  $C_u = 3$  from [38]

Table 5.2 shows very rough percentages for the difference between the simulation and physical pullout forces. Residuals for the simulations were determined by averaging the forces after 40 mm of strap displacement while residuals for the physical tests were estimated from the curves presented above. The percent difference between these values were calculated and are presented in Table 5.2, rounded to the nearest whole percentage.

Table 5.2: Percent difference in residuals between simulation and physical pullout tests

Uniformity Coefficient	Applied Pressure				
	25 kPa	41 kPa	69 kPa	103 kPa	138 kPa
$C_u=1$ (1.4)	17%	6%	3%	17%	19%
$C_u=2$	21%	27%	6%	N/A	N/A
$C_u=3$	20%	2%	10%	N/A	N/A

The maximum difference in residuals ends up being approximately 27% while the closest measurement was about 2%. On average residuals were off by about 14%.

Looking side-by-side in Figure 5.7, the force residuals are nearly identical at 25, 41, and 69 kPa. At 103 kPa the residual for the virtual simulation is several kilonewtons above the physical test result and the same holds true for the residual at 138 kPa. Although, at 138 kPa the physical test results are difficult to interpret as the pullout resistance appears to peak at 23-24 kN but then dips back down to 20 kN.

Comparing Figure 5.7 to Figure 5.8, the simulation residuals remain largely the same at a uniformity coefficient of two. The physical results, however, show a minor increase but also appear to have significant noise. At a uniformity coefficient of three, the residual forces for the simulations and the physical tests all increase. In Figure 5.9(b), it appears the 69 kPa data does not plateau and the force was still increasing when the test was stopped making it difficult to estimate a residual from that specific data.

Figure 5.10 shows a plot of the residual forces against the applied normal pressure from the results in Figure 5.7. Both results demonstrate a linear increase in the residual force as pressure increases. The linear trendlines for both sets of data are plotted for reference and the squared value of the correlation coefficient,  $R^2$ , is calculated. In this case, the closer the coefficient was to one, the stronger the data correlated to a linear trend. Thus, both sets are strongly linear with the simulation data having a slightly stronger relationship.

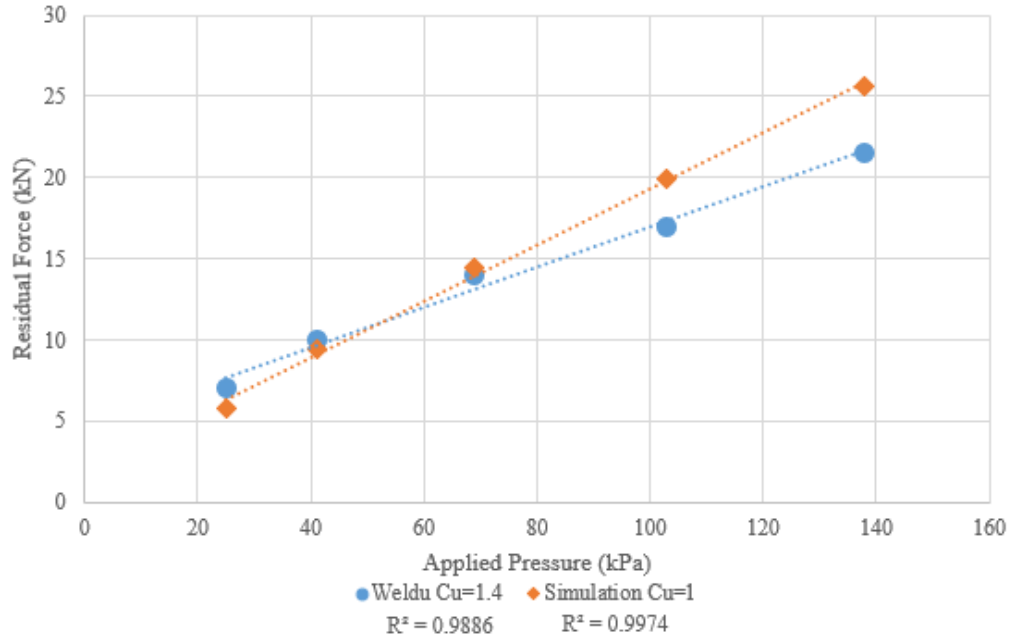


Figure 5.10: Residual force versus applied pressure (Taken from the data presented in Figure 5.7)

Overall, the virtual model correlated well to the physical tests. Some of the results plateaued and fluctuated around the same force, and all residuals from the simulations at least fell within 5 kN of the corresponding lab data.

### 5.5 Sources of Error and Examination of Differences Between Methods

One of the largest sources of error can be attributed to the load adjustment that was applied in the simulation. Without having exact measurements and seeing the setup from the physical testing it was impossible to determine the exact pressure the strap was experiencing. The load adjustment assumed the reported normal pressure for each test in [38] was exact. In addition, due to the simulation scaling, particle sizes, and packing density an educated estimate was made for the pressure applied to the strap in the physical tests via the aggregate. This estimate led to the rough pressure adjustment which was used to apply an equivalent normal pressure. Any error in this correction would have had a larger effect on the results of the simulations where less pressure was applied such as 25 kPa as opposed to 138 kPa.

Another imperfection in the simulation were the particle characteristics. For simplicity sake, all the particles used were spheres with a calibrated particle friction angle assigned to replicate the limestone used in [38]. Without having access to a sample of the aggregate, a specific gravity had to be assumed in order to achieve a porosity estimate which led to the convergence of a particle friction angle. Depending on the literature source, the value for specific gravity may vary between 2.3-2.7. The higher end of this range was used due to the uniformity of particle sizes being tested whereas a more finely crushed stone may result in a specific gravity on the lower end. In the event the specific gravity of the lab samples used was closer to a value of 2.3, the resulting porosity would have been roughly 10% lower. The exact effect this porosity difference would have on the results would need to be tested by recalibrating the particle friction angle. As an extension of this research, performing this sensitivity study would be useful to understand the effects of this parameter on the results. In addition, a sensitivity study could be performed on the particle packings in general. More than one numerical sample could be tested for each uniformity coefficient to understand the variability in the pullout tests results. Ideally, this could be done using different sized aggregates that resulted in the same uniformity coefficient. However, a simple sensitivity study could even be done by simply running the particle creation script multiple times to generate different, random packings that have slightly altered layouts but use the same particle sizes. These kinds of sensitivity studies would be useful in understanding just how much the particle characteristics can affect the pullout results.

While noise is not entirely absent from the simulations, it is primarily a concern with the physical testing. From the results in [38], there were most likely issues performing consistent tests. Some indications of this noise are shown by inconsistent trends in the pullout resistance at varying normal pressures, chatter in the systems during some tests, and large fluctuations in the pullout force when plateauing. An example of chatter can be seen in Figure 5.8(b) on the 25 kPa curve as the data appears to oscillate from point to point. Another oddity can be found in Figure 5.7(b) where the force in the 138 kPa run experiences a 4 kN drop over 5 mm before appearing to

plateau. Lastly, by looking at the change in pullout resistance from run to run against the changes in pressure, it is apparent that the physical tests have much less consistency. Figure 5.11 shows this trend by presenting the results of Figure 5.10 in an alternate way with the difference between the residual forces plotted against the difference in pressure.

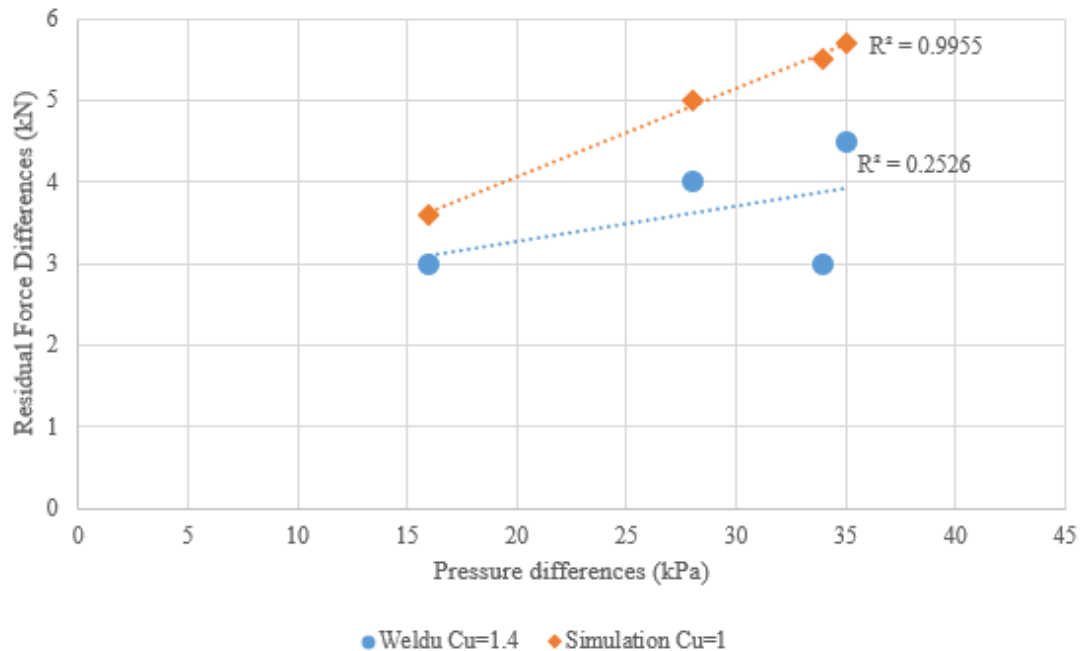


Figure 5.11: Change in residual force versus change in applied pressure (Data used from Figure 5.7)

Figure 5.11 demonstrates that the simulation results highly correlate to a linear model (which is consistent with the trend seen in Figure 5.10) whereas the physical test data lacks the same correlation. With the only change between these runs being the amount of pressure applied, a linear model would make sense as the pullout force is related to the applied load which is acting over the same area each time. In other words, pressure is linearly proportional to the force divided by the area. This situation is obviously idealized in the simulations with the particle distribution being identical in each run. If the outlying data point at (34,3) was removed from the plot in Figure 5.11, the physical data would be much more correlated to a linear model, emphasizing the

difficulty in reproducing test conditions in a physical setting from one setup to the next. The simulations certainly are not free from noise but there is less to worry about as it is a truly isolated system where the tests can be performed exactly as specified: compaction is done consistently every time, the strap pullout is done identically from run to run, applied pressures are exact, etc.

The largest percentage of error was likely due to the inaccuracies of the particle packings compared to the physical aggregate samples. Without having access to the true blends used in the lab tests, simplified packings were used that did not have a wide range of sizes or shapes and had estimated properties such as density. This lack of particle detail in conjunction with the difficult nature of quantifying the number of particles in the lab test resulted in additional uncertainty in the load adjustment to try and capture the true pressure the strap experienced. If the aggregate from the physical tests was more closely represented the percent error would likely drop substantially as it compounded the error in the load adjustment in addition to the separate inaccuracies it caused.

Outside of these sources of error there are undoubtedly other, smaller factors but these points are most likely the main influencers of discrepancies between the physical and simulated tests. With more complex aggregate samples strap geometries or test setups will have a larger effect on the results and would need to be better controlled.

## 5.6 Extraction of Additional Microscale Data

One of the major benefits to numerical simulations is the ability to output results that are very difficult (or impossible) to extract from physical systems. In the case of pullout testing, a more detailed understanding of particle interactions might be useful to designing better tests or more stable MSE walls. Using the functionality of YADE, interaction data can be captured for each individual particle throughout a simulation. For pullout testing, two useful microscale phenomena that were collected were particle rotations and force chains. The former tracks the

angular velocity of the particles which can then be contoured. Figure 5.12 shows an example of the particle rotation during a pullout test. Data such as this is useful in seeing how factors like aggregate blend, particle friction angle, and angularity prevent motion from developing and avalanching inside of an MSE wall. This test was created specifically for showing microscale data and does not correlate to any of the results presented above.

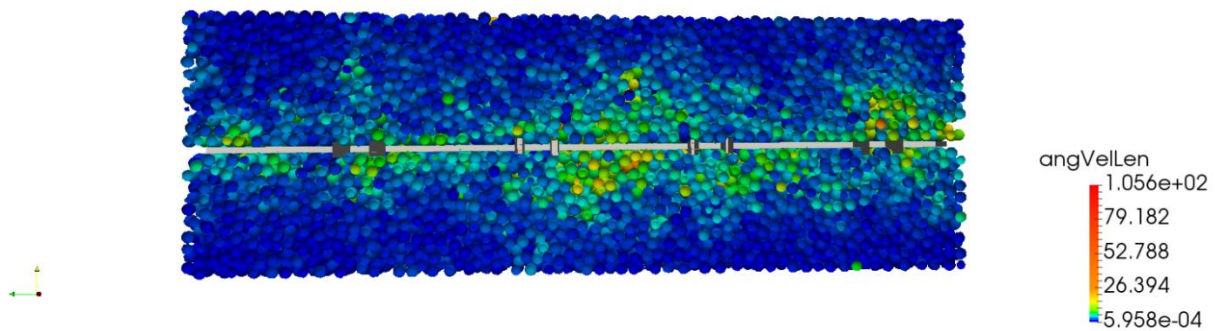


Figure 5.12: Particle rotation during a pullout test. Image created using ParaView [2, 8]

Figure 5.12 shows localized rotation near the strap and near no rotation by the edges of the apparatus. In addition, the large regions where angular velocity is observed in Figure 5.12 are near or following ribs on the strap geometry which shows that those geometric characteristics have a large effect on disturbing the particles. However, for this simulation, with a particle friction angle of  $46^\circ$  and a tightly packed specimen, the magnitude of the angular velocities is very low which implies the particles underwent minimal rolling and therefore majority of the motion was sliding. If interested, one could also view linear velocity magnitudes but in this case, it was just desired to view the angular velocities to see how particles were behaving with respect to rolling motion.

Similarly, Figure 5.13 shows an example of particle force chains during a pullout test which is useful in understanding where the structure is being stressed and how the strap geometry

influences branch development. The same simulation was used in Figures 5.12 and 5.13 to facilitate a visual comparison of particle rotation and force chain development.

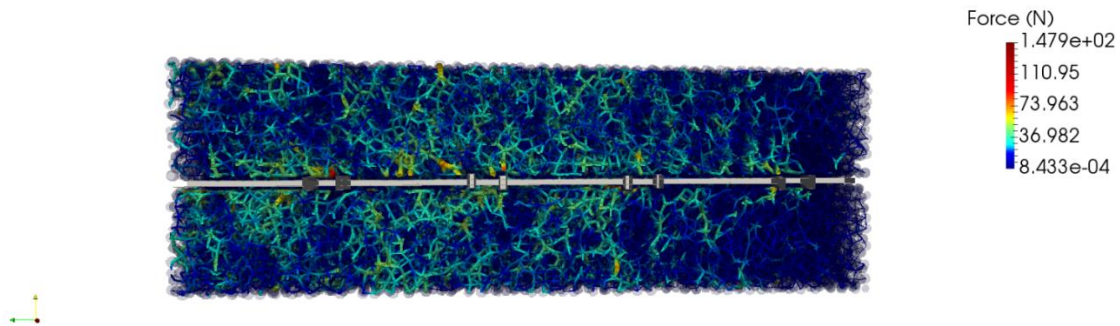


Figure 5.13: Force chains between particles during a pullout test. Image created using ParaView [2, 8]

The force chains above show patterns similar to the particle rotation; chains run along the strap and primarily branch out by ribs. Understanding how far the branches travel in a pullout simulation can be critical to minimizing edge effects from the apparatus. ASTM D6706 provides some guidelines regarding the size of the test apparatus to minimize these effects but using simulations would be one useful way to verify that wall effects are not a concern prior to physical setup.

The particle rotation and force-chain development appear to occur in complementary regions of the specimen. More force chain development is noticed where there is a lack of particle rotation, and the opposite holds true for particle rotation existing in areas where the force chains are relatively weak. This result makes physical sense as particle rotation is, in essence, what causes force chains to buckle and break. As a chain of contacting particles begin to rotate relative to one another the force chain developed along those particles collapses. Conversely, the particles are able to sustain a force chain if they do not rotate significantly relative to one another. It is evident that the ribs, as they pull out, drive force chains into the particles which collapse soon

after as the particles begin to rotate. This data could be useful in identifying and studying ideal rib spacing for different types of aggregates.

With microscale data such as above many studies could be performed to help evolve pullout testing or MSE wall design. For example, an entire study could be performed on how different parameters of the aggregates or changes in the strap geometry affect particle rotation. Force chain data could be used to guide designs for MSE walls by influencing how far away adjacent reinforcement straps should be placed.

Ultimately, microscale information from simulations could help reduce the uncertainty in MSE wall design significantly, but more detailed research should be performed to understand and link microscale phenomenon to physical systems.

## 6. CONCLUSIONS, LEARNINGS, AND FUTURE WORK

The purpose of this research was to demonstrate the capability of performing numerical pullout tests. To achieve this goal, a simulated environment for testing was developed using the open-source framework of YADE. Three series of tests were performed with aggregates at different uniformity coefficients in which the data was compared to physical test results captured in previously published research. In addition, a simple triaxial simulation was created for the purpose of calibrating the particles against the aggregate used in the physical testing research. Data from the numerical environment was also captured to show the capability of examining microscale phenomenon such as rolling and force chains within the particles.

### 6.1 Conclusions and Learnings

Overall, pullout simulations produced results and trends that correlated well to results collected in physical testing. The closest numerical pullout residuals were roughly within 2% of the physical residuals and none of the residuals were greater than approximately 27% different. However, the residual differences were sensitive to rounding on the physical pullout resistances. In addition, numerical simulations followed a highly linear model as the normal force on the strap increased. Scaling the particle sizes, strap dimensions, and box length up by a factor of two from the physical test did not appear to produce any major difference in results except for the pullout force plateauing at about double the pullout distance. In general, numerical pullout residuals under the same applied pressure increased as the uniformity coefficient increased. The increase in pullout force was minimal from  $C_u = 1$  to  $C_u = 2$  but increased roughly 27-34% from  $C_u = 2$  to  $C_u = 3$ . This suggests that as the aggregate becomes more well graded, the pullout resistance increases but more tests would need to be done to confirm this trend. Capturing all these results required proper characterization and calibration of the aggregate which was done so through linking numerically evaluating microscale parameters such that they produced a macroscale

response roughly equivalent to the physical aggregate. Linking the microscale friction angle to the macroscale friction angle of the aggregate helped ensure proper behavior of the particles.

Beyond the tests, viewing microscale data showed strong patterns of force chains developing from ribs and branching out towards the front face of the pullout box. Conversely, large amounts of particle rotation were observed in the wake of buckled force chains. The capability to extract, view, and learn from this data has the potential to help influence the MSE wall design process. Qualitatively, these microscale results can be used to understand how far force chains and particle rotations are propagating inside of the system which can then be used to guide reinforcement placement. Alternatively, microscale data can be used to perform extensive investigations into how different materials and aggregate samples interact with one another.

Compared to physical testing, the numerical models appeared much easier to isolate from noise than physical systems which makes them a good candidate for quick answers or holding variables constant during testing. Setup for a simulation is based on user-specified commands and therefore the virtual environment will contain exactly what is input. Setting up a physical test as specified in [6] requires a variety of different equipment which greatly increases the chance of introducing a large amount of noise into the system and may require detailed troubleshooting before believable results are collected. As an example, ASTM D6706 specifies “To maintain a uniform normal stress, a flexible pneumatic or hydraulic diaphragm-loading device which is continuous over the entire pullout box area should be used and capable of maintaining the applied normal stress within  $\pm 2\%$  of the required normal stress”. Whereas, a simulation can apply the normal stress exactly as desired and perfectly over the entire pullout box area with a weightless plate. After the initial setup of the simulation, tests were easily repeatable which makes them ideal for determining how specific parameters might affect results. For example, performing a study on strap geometry would be easy to evaluate as the rest of the simulation can be held constant including the exact particle packing.

An additional benefit was that virtual testing, such as what was done in this research, is extremely cost-effective. Material costs to set up a test are zero and the only costs that might be considered are computation resources or software packages. For the purpose of MSE wall construction, if companies plan to perform some type of pullout testing then simulations will almost definitely save money in the long run. For the time being, however, computation time is a drawback to setting up simulations of this fidelity. As the quantity of particles increases, the computation time increases significantly. Therefore, either a lot of processing power is required or simplification of the problem is necessary to obtain results in a reasonable timeframe.

Lastly, depending on the software package used, it may be difficult or impossible to truly capture the level of fidelity that is desired in a simulation. Additional complexity will make setup and controlling a simulation more difficult not to mention introducing additional stability concerns. For example, to create truly angular particles with various shapes and sizes blended throughout a packing would require additional software functionality and has a greater potential to cause interaction singularities depending on the contact algorithm. Not having a highly accurate particle packing was likely the largest source of error as it tends to compound error in other areas.

Performing a sensitivity study with different particle packings and different properties would have been useful for understanding just how much of an effect these parameters could have had on the numerical results. Each of the numerical pullout results shown were performed with only one particle packing and therefore lacked variability. An easy study to follow-up the results presented in this paper would be recreating multiple particle packings for the same uniformity coefficient and testing those at the same normal pressures to understand the variability in the results.

## 6.2 Future Work

As a result of this research and previous studies, some potential expansions of this field are listed below:

1. Perform a more in-depth study, still based on [38], with more complex particle packings that include more particle sizes and larger quantities. Increasing uniformity coefficient and introducing more size variation in this research tended to make results less similar to the physical tests. It could be argued that this dissimilarity was mostly due to noise in the system or a lack of having the proper characteristics modeled in the simulation, but nonetheless, more simulations will help paint a better picture of the trends.
2. Use a numerical pullout test to evaluate the exact effect different parameters have on the test results and MSE walls as a whole. This is where a sensitivity study would be critical for understanding the variability in the results. For example, rerunning with different aggregate packings that result in an identical uniformity coefficient. The use of a virtual environment allows for the possibility of much more quantitative results as almost any piece of data can be requested as an output. A Monte Carlo style method would be an ideal choice for canvassing all the different factors that play a role in pullout test simulations. Some parameters that would be intriguing to investigate further are features such as: strap geometry (length, width, grid, rib size and shape, rib quantity, rib spacing), strap material, rolling resistance, particle friction angle, particle depth and width, packing density, etc.
3. Develop a method to quantitatively evaluate the importance and effects of microscale interactions within pullout tests such as force chain development and particle rotation. As presented in this research, requesting microscale results is possible and reveals how particles are behaving at different points during a test. Being able to better understand

this behavior and counteracting negative interactions can be useful in minimizing failures or collapse inside MSE walls.

4. Implement a FEM/DEM multiscale method such as the one presented in [18] for performing pullout tests. Two of the biggest drawbacks to simulations are computation time and capacity. Creating a simulation with 100 million particles is not feasible in terms of run time and being able to manipulate the setup. However, an FEM/DEM approach would allow for the critical particles that are interacting with the strap to be modeled in detail while particles beyond an effective boundary are captured by representative volume elements (RVE). Simulations that may have required 100 million particles would then only require a couple hundred thousand and the rest would be captured in finite elements. Detailed calibration would need to be done to ensure the RVE is adjusted to act like the simulated aggregate and work would need to be done to ensure proper behavior at particle-to-RVE transition boundaries. Things like force chains and rolling characteristics may become important when deciding where to transition to RVEs such that detailed interactions are not omitted.
5. Depending on the backfill being tested, adding in more complex particle modeling techniques to capture aggregate behavior overall such as rolling resistance and deformable particles may be beneficial to simulating an accurate test. Rolling resistance was tested in limited fashion for this research but was ultimately left out as it could have been its own in-depth study.

## BIBLIOGRAPHY

- [1] *AASHTO LRFD Bridge Design Specifications*. American Association of State Highway and Transportation Officials, 2017.
- [2] Ahrens, James, et al. *ParaView: An End-User Tool for Large Data Visualization, Visualization Handbook*. Elsevier, 2005.
- [3] Ai, Jun, et al. "Assessment of Rolling Resistance Models in Discrete Element Simulations." *Powder Technology*, vol. 206, no. 3, 2011, pp. 269-282.
- [4] Alzamora, Daniel, and Richard J Barrows. "Mechanically Stabilized Earth Walls on the Interstate Highway System: Thirty Years of Experience." *TR News*, no. 249, 2007, pp. 32-33.
- [5] ASTM E11-17. "Standard Specification for Woven Wire Test Sieve Cloth and Test Sieves." *ASTM International*, 2017.
- [6] ASTM D6706-01. "Standard Test Method for Measuring Geosynthetic Pullout Resistance in Soil." *ASTM International*, 2013.
- [7] ASTM D7181-11. "Method for Consolidated Drained Triaxial Compression Test for Soils." *ASTM International*, 2011.
- [8] Ayachit, Utkarsh, et al. *The ParaView Guide: A Parallel Visualization Application*. Kitware, 2015.
- [9] Baraff, David. *Dynamic Simulation of Non-Penetrating Rigid Bodies*. PhD thesis. Cornell University, 1992.
- [10] Bligh, Roger P. *Design of Roadside Barrier Systems Placed on MSE Retaining Walls*. Transportation Research Board, 2010.
- [11] Bourrier, Franck, et al. "Discrete Modeling of Granular Soils Reinforcement by Plant Roots." *Ecological Engineering*, vol. 61, 2013, pp.646-657.

- [12] Chang, J. C., et al. "Pull Resistance and Interaction of Earthwork Reinforcement and Soil." *International Journal of Rock Mechanics and Mining Sciences & Geomechanics Abstracts*, vol. 16, no. 3, 1979, p. 68.
- [13] Cundall, P. A., and O. D. L. Strack. "A Discrete Numerical Model for Granular Assemblies." *Géotechnique*, vol. 30, no. 3, 1980, pp.331-336.
- [14] Donzé, F. V., et al. "Modeling Fractures in Rock Blasting." *International Journal of Rock Mechanics and Mining Sciences*, vol. 34, no. 8, 1997, pp.1153-1163.
- [15] Effeindzourou, Anna, et al. "Modelling of Deformable Structures in the General Framework of the Discrete Element Method." *Geotextiles and Geomembranes*, vol. 44, no. 2, 2016, pp. 143-156.
- [16] Fleischmann, Jonathan A. *Micromechanics-Based Continuum Constitutive Modeling of Isotropic Non-Cohesive Particulate Materials, Informed and Validated by the Discrete Element Method*. Dissertation. University of Wisconsin-Madison, 2013.
- [17] Fukumoto, Yutaka. *Particle Based Multiphysics Simulation for Applications to Design of Soil Structures and Micromechanics of Granular Geomaterials*. Dissertation. Kyoto University, 2015.
- [18] Guo, Ning, and Jidong Zhao. "A Coupled FEM/DEM Approach for Hierarchical Multiscale Modelling of Granular Media." *International Journal for Numerical Methods in Engineering*, vol. 99, no. 11, 2014, pp.789-818.
- [19] Gurung, N., & Y. Iwao. "Pull-out Test Analysis for Geo-reinforcement." *Geotextiles and Geomembranes*, vol. 17, no. 3, 1999, pp.157-170.
- [20] Hertz, H. R. "On Contact Between Elastic Bodies." *Collected Works*, 1895.
- [21] Hu, Guoming, et al. "On the Determination of the Damping Coefficient of Non-Linear Spring-Dashpot System to Model Hertz Contact for Simulation by Discrete Element Method." *2010 WASE International Conference on Information Engineering*, May 2011, p. 984.

- [22] Iwashita, Kazuyoshi, and Masanobu Oda. "Rolling Resistance at Contacts in Simulation of Shear Band Development by DEM." *Journal of Engineering Mechanics*, vol. 124, no. 3, 1998, pp. 285-292.
- [23] Koerner, Robert. "'Koerner's Korner' on MSE Wall Failures." *Geosynthetic.net*, 2013.
- [24] Kozicki, Jan, et al. "Discrete Simulations of a Triaxial Compression Test for Sand by DEM." *International Journal for Numerical and Analytical Methods in Geomechanics*, vol. 38, no. 18, 2014, pp. 1923-1952.
- [25] Lawson, William D., et al. "Pullout Resistance Factors for Inextensible Mechanically Stabilized Earth Reinforcements in Sandy Backfill." *Transportation Research Record: Journal of the Transportation Research Board*, vol. 2363, no. 1, 2013, pp. 21-29.
- [26] Mindlin, R. D., and H. Deresiewicz. "Elastic Spheres in Contact Under Varying Oblique Forces." *Journal of Applied Mechanics*, vol. 20, 1953, pp. 327-344.
- [27] Mitra, Emon. *Development of Discrete Element Models to Predict the Behaviour of Blocky, Angular Ceramic Materials Under Uniaxial and Triaxial Compression*. MS thesis. UNSW Canberra at ADFA, 2017.
- [28] Mohiuddin, Ather. *Analysis of Laboratory and Field Pull-out Tests of Geosynthetics in Clayey Soils*. MS thesis. Louisiana State University, 2003.
- [29] O'Sullivan, Catherine. *Particulate Discrete Element Modelling: A Geomechanics Perspective*. Routledge, 2017.
- [30] Rathje, Ellen M., et al. *Evaluation of Crushed Concrete and Recycled Asphalt Pavement as Backfill for Mechanically Stabilized Earth Walls*. Texas Department of Transportation, 2006.
- [31] Schwartz, E. G., and A. S. Weinstein. "Model for Compaction of Ceramic Powders." *Journal of the American Ceramic Society*, vol. 48, 1965, pp. 346-350.

- [32] Shiu, Wenjie, et al. "Discrete Element Modelling of Missile Impacts on a Reinforced Concrete Target." *International Journal of Computer Applications in Technology*, vol. 34, no. 1, 2009, p. 33.
- [33] Šmilauer, V., et al. "Yade Documentation 2nd Ed." *The Yade Project*, 2015.
- [34] Suits, L David, et al. "Laboratory Evaluation of Pullout Capacity of Reinforced Silty Sands in Drained and Undrained Conditions." *Geotechnical Testing Journal*, vol. 28, no. 4, 2005, pp. 370-379.
- [35] Thoeni, Klaus, et al. "A 3D Discrete Element Modelling Approach for Rockfall Analysis with Drapery Systems." *International Journal of Rock Mechanics and Mining Sciences*, vol. 68, 2014, pp. 107-119.
- [36] Tran, V.D.H., et al. "A Finite–Discrete Element Framework for the 3D Modeling of Geogrid–Soil Interaction under Pullout Loading Conditions." *Geotextiles and Geomembranes*, vol. 37, 2013, pp. 1-9.
- [37] Wang, Xiaoliang, and Jiachun Li. "Simulation of Triaxial Response of Granular Materials by Modified DEM." *Science China Physics, Mechanics & Astronomy*, vol. 57, no. 12, 2014, pp. 2297-2308.
- [38] Weldu, Mehari T. *Pullout Resistance of MSE Wall Steel Strip Reinforcement in Uniform Aggregate*. MS thesis. *University of Kansas*, 2015.
- [39] Weldu, Mehari T., et al. "Effect of Aggregate Uniformity on Pullout Resistance of Steel Strip Reinforcement." *Transportation Research Record: Journal of the Transportation Research Board*, vol. 2579, no. 1, 2016, pp. 1-7.
- [40] Wendland, Steve. "When Retaining Walls Fail." *Consulting Specifying Engineer (CSE)*, 2011.

## APPENDIX

### Appendix A. Notes on Rolling Resistance and Friction Angle

While rolling resistance was not utilized for the bulk of this research, some early simulations did incorporate this effect. YADE does have the functionality to set up rolling resistance inside a simulation, which is done by using a specific property card wherein the user may then manipulate a coefficient of rolling friction and rolling stiffness.

Ultimately, the primary conclusion was that capturing the particle friction angle, normal stress, and strap geometry were more critical to the outcome of the results. Adding in rolling resistance and varying these parameters ended up resulting in minimal changes to some of the early results. In addition, it was difficult to calibrate rolling resistance to any meaningful quantities such that it was accurately aiding in modeling the limestone aggregate from the physical testing. Some of these early results can be found in Appendix D.

Minimal effects were noticed with rolling resistance enabled in pullout simulations and thus contact tracking simulations were run with rolling resistance to ensure it was working properly and to better understand the inputs. These simulations were all just modified versions of the contact tracking presented in Section 3.5 but with rolling resistance enabled. With one particle rolling down the strap the friction angle between the strap and the particle were varied from 1-80 degrees in 10-degree increments. At each of those friction angle increments the coefficient of rolling friction and the rolling stiffness were ramped up. Both the linear and rotational displacements of the particle were tracked to compare the effects of these parameters. Some conclusions and takeaways are listed below:

1. A low friction angle of  $1^\circ$  resulted in near zero rolling. Almost all the displacement was linear and therefore the particle was sliding and thus rolling resistance parameters were not even investigated.

2. As the friction angle ramped up to approximately  $20^\circ$  with no rolling resistance the rotational displacement was roughly 50% of the linear displacement (some sliding and rolling). Once the friction angle reached  $40^\circ$ , the rolling displacement was very nearly equal to the linear displacement (i.e., fully rolling).
3. With full rolling, the rolling stiffness was varied up to a value of 1000 while the coefficient of rolling friction was left at zero. At each value the rotational displacement was not affected and remained equal to the linear displacement.
4. Varying the coefficient of rolling friction while there was no rolling stiffness resulted in both displacements being equal.
5. Setting the coefficient of rolling friction to a value of one and the rolling stiffness to any positive value resulted in pure sliding which verified that the coefficient of rolling friction should be set between 0-1.0 to effectively implement rolling resistance.
6. The rolling stiffness was arbitrarily set to a value of five while the coefficient of rolling friction was ramped between 0 and 1.0. As the coefficient was very close to zero (0.001 for example) the particle was near pure rolling. Once the value was greater than 0.1 substantially less rolling was noticed implying the rolling resistance was having an effect.

Figure A.1 shows the rotational displacement of the particle versus the linear displacement in select contact tracking simulations. Three data sets show how the rotational and linear displacements vary when only the particle friction angle,  $\phi$ , is changing. The other three data sets have a constant friction angle of  $40^\circ$  and vary the coefficient of rolling friction,  $\eta$ .

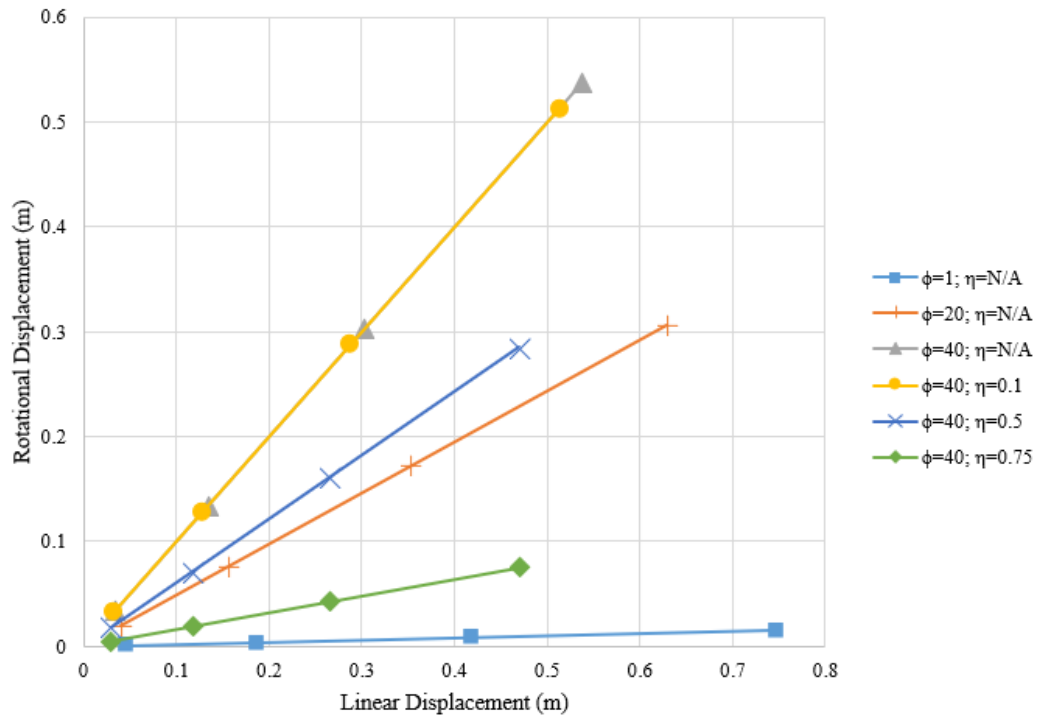


Figure A.1: Rotational displacement versus linear displacement of a particle during contact tracking simulations

The graph shows that as the particle friction angle increases the linear displacement becomes equal to the rotational displacement. Adding in the coefficient of rolling friction had no effect at a small value ( $\leq 0.1$ ) however as the value approached 1.0 the rotational displacement was nearly gone.

Rolling stiffness is still a parameter that should be tested and understood with regards to pullout tests. Still, with the knowledge gained from the contact tracking study, pullout simulations could be run and studied with rolling resistance enabled. However, the point still stands that it would be difficult to put accurate, numerical values to these rolling parameters without a detailed understanding of the aggregate properties.

## Appendix B: Material and Pullout Tests for Airsoft BB Pellets

Early into the research, some physical testing was performed in Marquette's Engineering Materials Structural Testing Lab (EMSTL); by Videkovich. These tests were conducted with the purpose of being able to correlate the results to DEM simulations. The aggregate in use for the physical tests were airsoft BB pellets which were approximately 6 mm in diameter and near perfect spheres. The uniform shape and size all throughout the physical test made it ideal for correlating to virtual simulations due to ease of modeling the particle packing. An additional benefit to doing this simplified testing was the luxury of being able to characterize the BBs and calibrate them more easily inside the simulation. To that end, detailed material testing was done to understand the composition of the aggregate better.

### **Material Testing Summary**

In regard to the material testing, flattening the balls on a hot plate with a piece of aluminum showed that they were thermoplastic. Following that, an FTIR spectrum from a flat specimen further showed that the pellets contained some level of polystyrene which can be seen in Figure A.2. As a further examination, several balls were vaporized in a furnace at 400°C to test for inorganic filler. Some residue remained after removal from the furnace and FTIR spectrums were captured for the flattened specimen and residue which are shown in Figures A.3 and A.4 respectively.

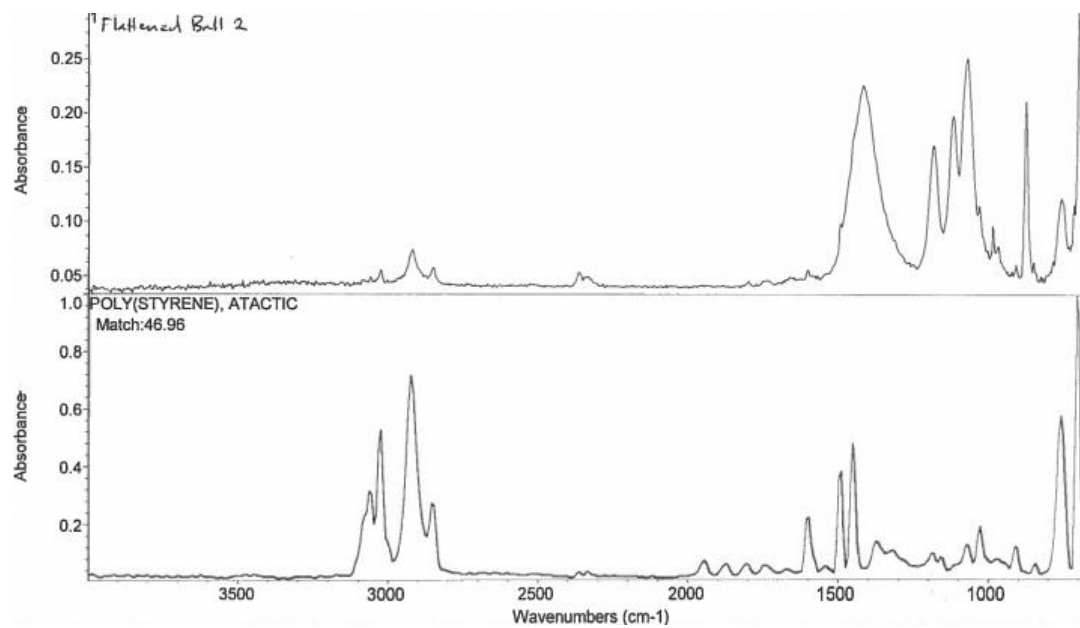


Figure A.2: FTIR spectrum from flattened pellet specimen

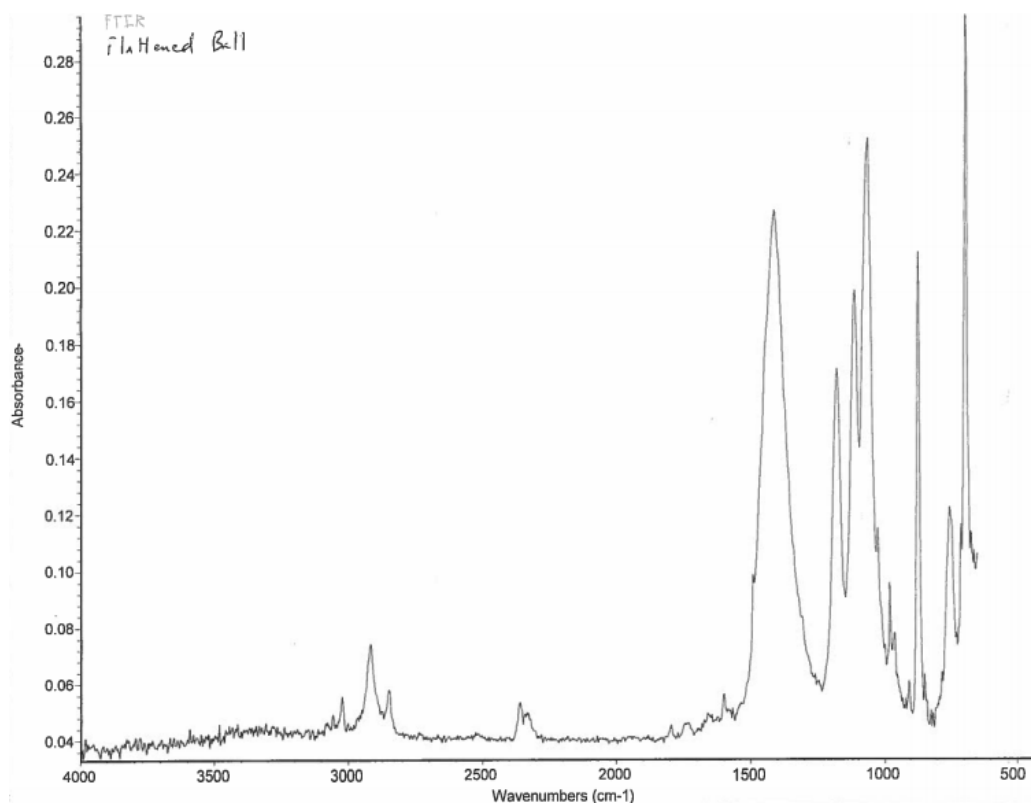


Figure A.3: FTIR spectrum from flattened pellet specimen post vaporization

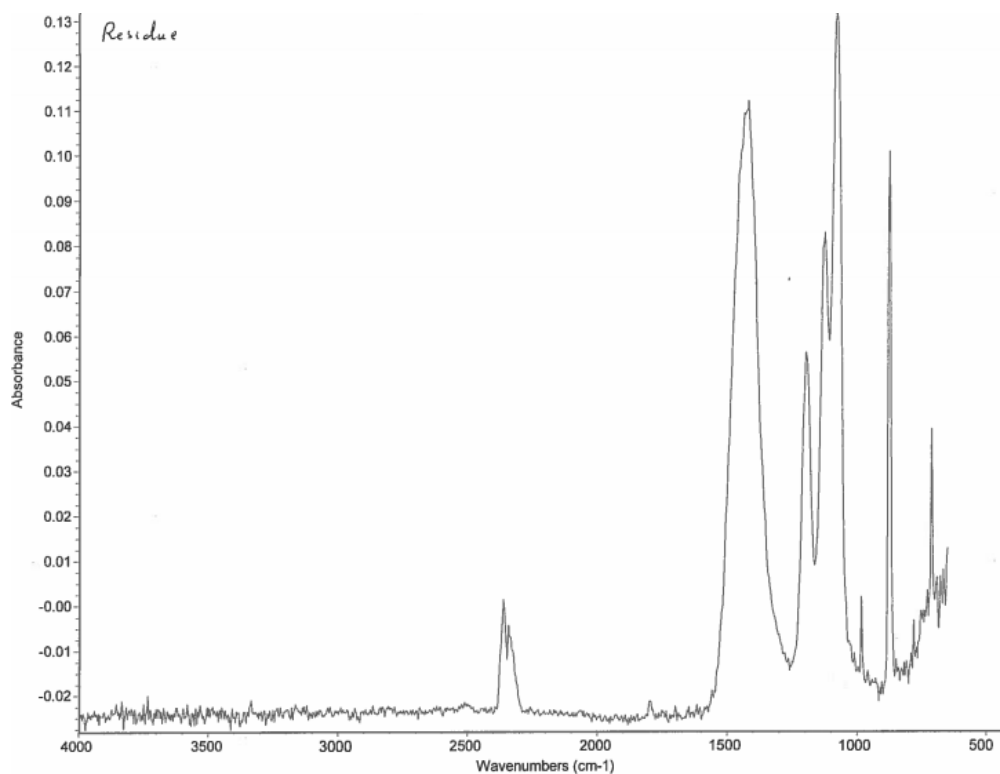


Figure A.4: FTIR spectrum from pellet residue post vaporization

One pellet cross section was mounted in fast cure acrylic then ground and polished to be examined using a SEM. Figures A.5 and A.6 show two of the high magnification images captured. Using SEM-18-2-4-6, EDS spectrums were obtained by shooting different points in the microstructure which exhibited calcium, barium, sulfur, oxygen and carbon peaks as shown in Figure A.7. An EDS spectrum was taken from the vaporized residue but it did not offer new insights as it mostly just comprised of a variety of particulate matter.

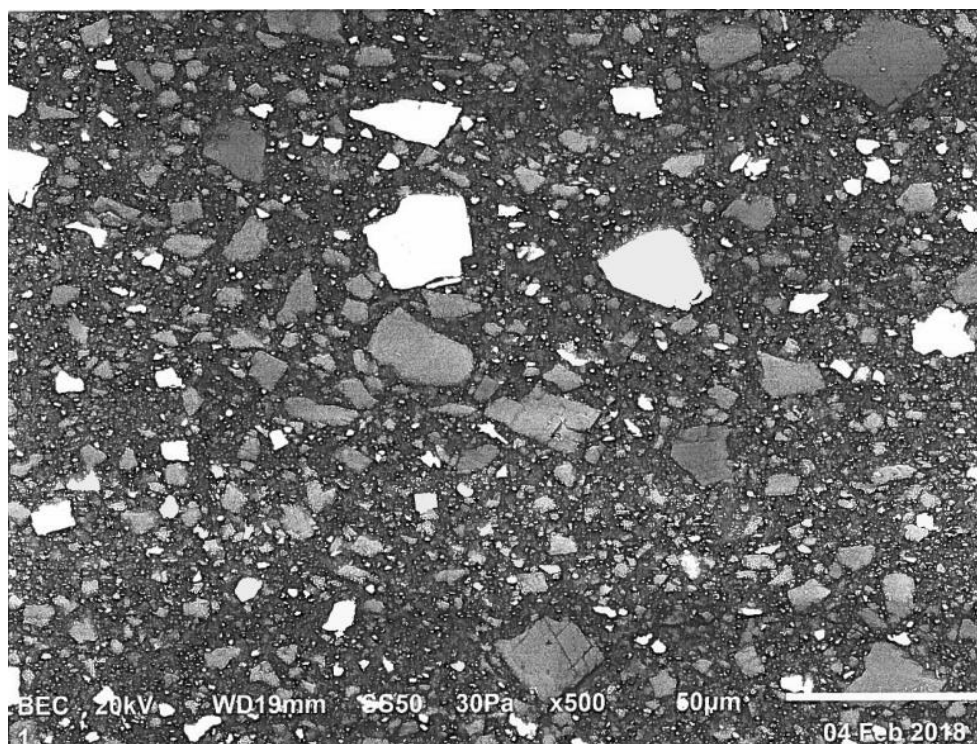


Figure A.5: SEM-18-2-4-5; High magnification (x500) of BB pellet specimen

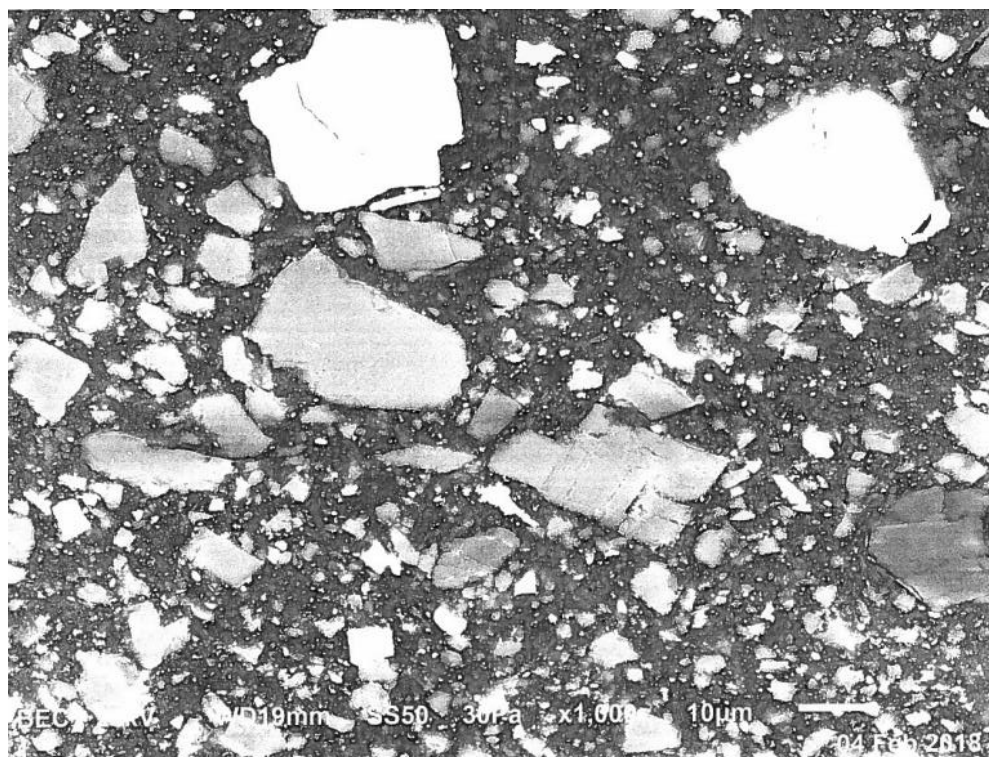


Figure A.6: SEM-18-2-4-6; High magnification (x1000) of BB pellet specimen

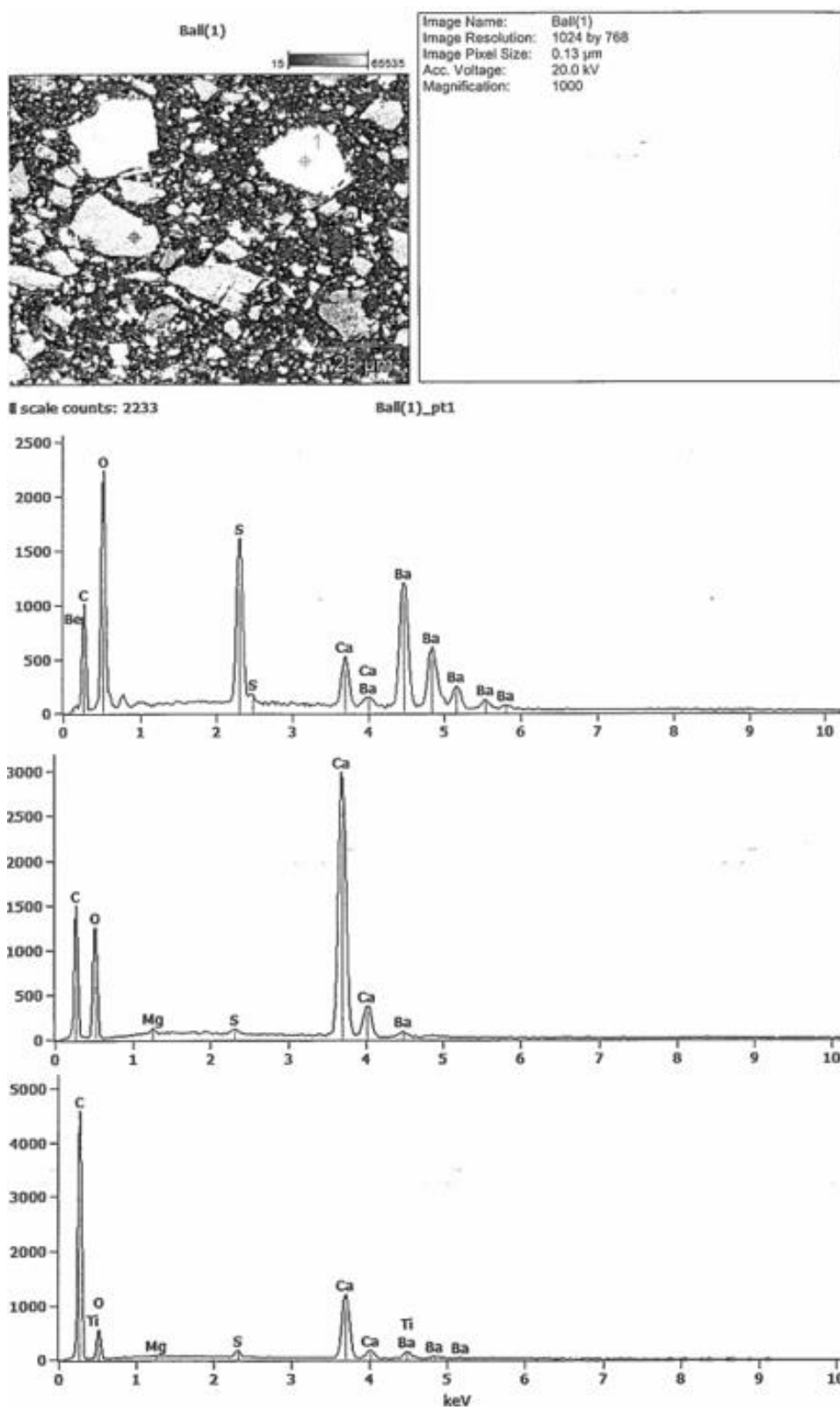


Figure A.7: EDS spectra capture from examination of the pellet microstructure

In addition, the density of the airsoft BBs was calculated in two different ways and recorded as the average between the two methods. For each method, three different balls were used to account for some variance across the samples. Density was first determined by measuring the weight of the pellets in air and water and then calculating via Equation (A.1).

$$\rho_{BB,avg1} = \frac{m_{air}}{m_{air} - m_{water}} \quad (A.1)$$

A scale accurate to  $\pm 0.001$  grams was used to measure the weight. The end result was an average density of  $1.810 \pm 0.0012$  g/cm<sup>3</sup>. The second method involved three different samples and was simply measuring the diameter of the spheres with a Vernier caliper and measuring the mass to the nearest 0.001 gram and finally calculating using Equation (A.2)

$$\rho_{BB,avg2} = \frac{m_{BB}}{V_{sphere}} \quad (A.2)$$

where the volume of a sphere is given by Equation (A.3).

$$V_{sphere} = \frac{1}{6} \pi d^3 \quad (A.3)$$

The end result of this method was an average density of  $1.853 \pm 0.023$  g/cm<sup>3</sup>. Based on the results of each method the end density was recorded as  $1.83 \pm 0.02$  g/cm<sup>3</sup>.

Finally, the volume percent of plastic in the BB pellets was calculated using measured weights before and after vaporization. The pellet mass was measured prior to entering the furnace as 0.2071 grams and the weight of the residue remaining after the plastic was vaporized was

0.1355 grams. Therefore, the weight of the plastic,  $m_{plastic}$ , was 0.0716 grams by simple subtraction which resulted in a weight percent of 34.6%. Assuming a polystyrene plastic density,  $\rho_{poly}$ , of 1.05 g/cm<sup>3</sup> the approximate volume percent of plastic was determined as 62.1% by Equation (A.4).

$$V\%_{plastic} = \frac{m_{plastic}}{\rho_{poly} V_{sphere}} \quad (A.4)$$

It is worth noting that direct shear tests were conducted with the BB pellets, but the results were ultimately unreliable and not meaningful to the simulation, as a microscopic friction angle is required as input as opposed to a macroscopic friction angle which is the result of the direct shear test. However, using research conducted by Fleischmann in [16], a microscopic friction angle for spheres can be correlated to a macroscopic friction angle via Figure 6.26 (Figure A.8 below) in his paper. Therefore, the angle of repose was measured for the pellets which resulted in a friction angle of 25°. Using the figure mentioned, this results in a micro friction angle of 15-20 degrees without rounding for the spheres.

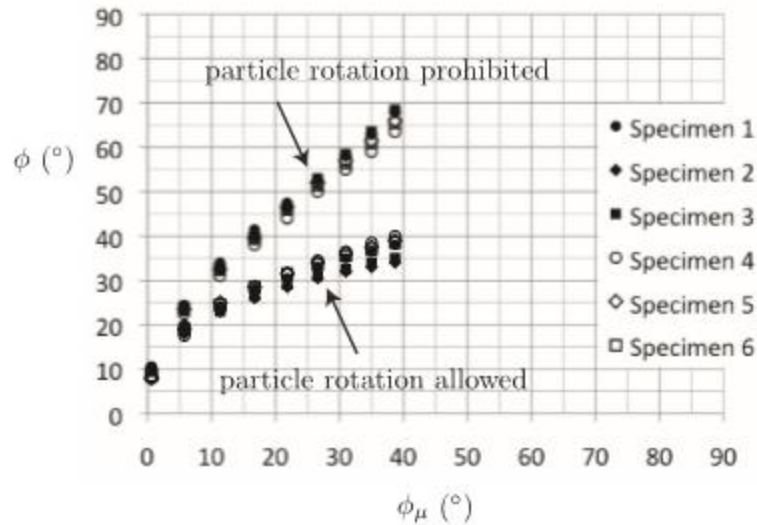


Figure A.8: Plot of the macroscopic friction angle,  $\phi$ , versus the microscopic friction angle,  $\phi_\mu$ . Taken directly from Figure 6.26 in [16]

This level of detail could not be done for the primary aggregate used in the simulations for this research, but if available, similar testing should be done to fully characterize the sample being replicated in simulations if the purpose is to correlate to physical results.

### **Pullout Testing Summary**

Several physical pullout tests were setup and conducted in Marquette's EMSTL lab, by Videkovich, with the goal of correlating simulations to the pullout force results. The parameters shown in Table A.1 are general details used for both the virtual and physical test setup. The pullout box was filled with the airsoft BB pellets as the aggregate and tests were done using a ribbed and smooth steel strap. Figures A.9 and A.10 show two of the physical results gathered from Marquette's EMSTL lab.

Table A.1: General pullout parameters for pullout tests conducted in Marquette's EMSTL lab

<b>BB Pullout Test Parameters</b>	
<b>Pullout Box</b>	
Length (mm)	1800.0
Width (mm)	290.0
Height (mm)	610.0
<b>Strap</b>	
Length (mm)	2628.9
Width (mm)	50.3
Thickness (mm)	5.1
Material	Galvanized Steel
Young's Modulus (GPa)	200
Poisson's Ratio	0.3
Density (g/cm <sup>3</sup> )	7.86
<b>BB Pellets</b>	
Diameter (mm)	5.95
Young's Modulus (GPa)	0.05
Poisson's Ratio	0.45
Density (g/cm <sup>3</sup> )	1.83
Friction angle (degrees)	17.5
<b>Normal Loads</b>	
Pressure 1 (kPa)	6.15
Pressure 2 (kPa)	8.14
Pressure 3 (kPa)	10.15
Pressure 4 (kPa)	14.12

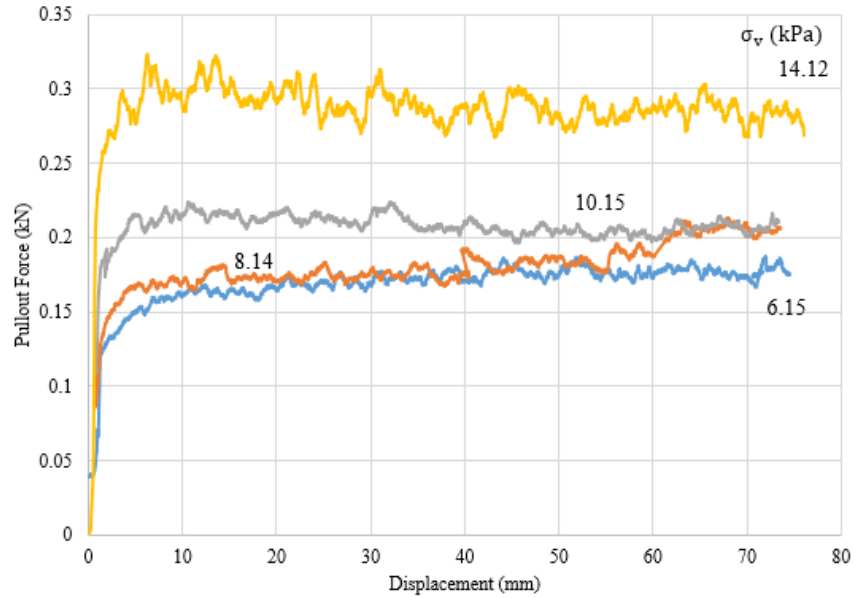


Figure A.9: Pullout results from physical tests with a smooth strap

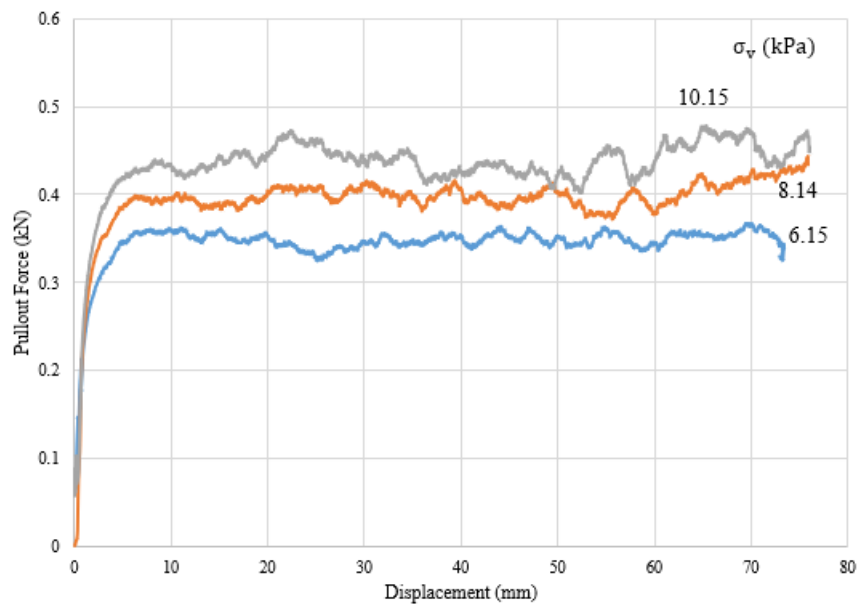


Figure A.10: Pullout results from physical tests with a ribbed strap

Attempts were made to duplicate these results via simulation, but ultimately this was not feasible. One major reason was the total amount of BBs being used would have resulted in extremely long simulation times at true scaling. Scaling up the particles was attempted but

capturing the applied load and transferring that into the model did not work well. However, one of the larger concerns was the force required to pull the strap out of the box was low (maximum of about 100 lbs) with a minimal range of roughly 30 lbs. As a first attempt, correlating in such a narrow window of values and then being able to potentially extrapolate trends would have been a very difficult task.

Even if a reasonable level of correlation was achieved it would have been much less believable with noise from the physical system and the simulation both having a heavy influence on the results. As an example, with normal loads ranging from roughly 6-14 kPa, the equipment used to apply the normal pressure in the physical test was unpredictable at times and had some error which would have made it very difficult to derive a reasonable load adjustment for the simulation if scaling was used. Any error in the load adjustment for the simulation could contribute largely to undershoot or overshoot in the pullout force results with the applied pressure being low from the start. One early example of results is shown in Figure A.11 which was an attempt to match the results of the smooth strap run with 14.12 kPa applied. The pullout force ends up being about a full factor of 10 off. Reasons for these results vary and likely compound but largely the applied force may have been incorrect. The simulation pertaining to the results in Figure A.11 was scaled up by a factor of 4 (strap and particles).

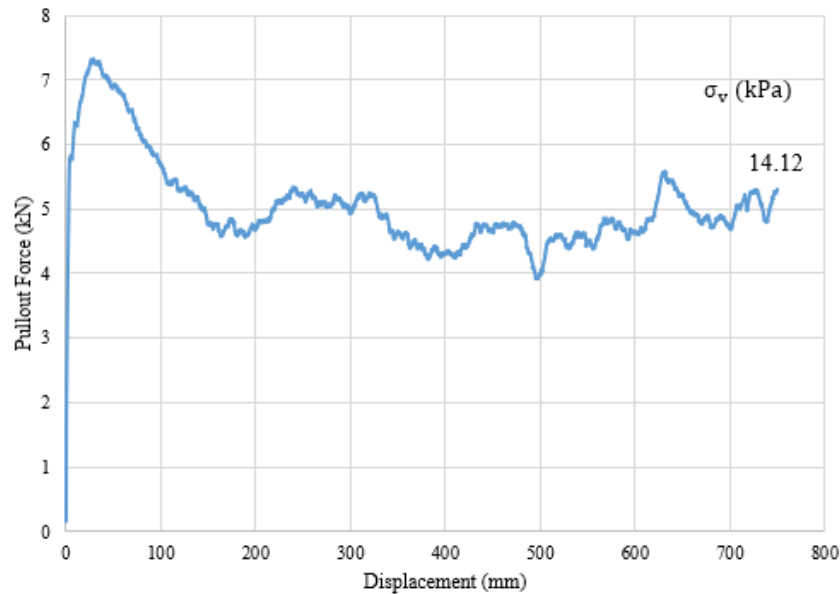


Figure A.11: Early attempt at pullout simulation with 4x scaled up BBs and strap

Interestingly, the spheres quickly show a large transient peak which then settles into a pullout residual. This peak makes physical sense as when the initial displacement begins it is expected that perfect spheres will lock with one another which is why a large load is observed at the beginning. As the spheres begin to shift and roll over one another a more steady-state response is observed. Oddly, the physical tests did not demonstrate this phenomenon despite the BBs being nearly perfect spheres.

In addition, contours of angular velocity were created to check how particles were behaving and ensure some rolling was being observed. Occasionally, in some steps, there were particles that experienced very large rotations in random locations throughout the pullout apparatus where no neighboring particles had large angular velocities. These particles were deemed to be ‘rattlers’ which is a term used to describe a particle that may be briefly hovering in a small void after some previous contact [29].

Nonetheless, it would be interesting to backtrack and apply the simulation setup used for correlation in the main body of this research to these BB pellet results. The correlation that was

achieved by comparing the simulation data to the physical results presented in [38] provides confidence that it would now be feasible to achieve correlation with other pull-out test setups.

### Appendix C. Particle Distribution Generator

Creating a proper particle distribution for the simulations employed here involved a guess and check approach to ensure that particles were all spaced out properly when the packings were imported and that they would not collide with any unwanted objects. For the purpose of this research a particle distribution aid was created that served to limit the guess and check process by giving rough estimates for the particle packing dimensions or by estimating the size of the pullout apparatus and strap features. The functionality of the spreadsheet is in no way perfect and uses a lot of assumptions to generate an initial, educated guess for the requested inputs.

The primary way in which the spreadsheet was used was to generate the percent by number of each particle size needed for a simulation and provide a suggested grid size (x, y, z) of particles. The bulk of the first half of the spreadsheet served as a conversion tool to change between the percent by volume/weight of a particle size into the equivalent percent by number. This feature was useful as the code used for making the particle packings required percent by number as an input but often particle distributions are presented as percent by volume/weight in geotechnical engineering.

To get a valid output, the user inputs the pullout box dimensions, the desired particle diameter sizes with their percent by volume, and optionally a packing density. The spreadsheet calculates the volume of the box and will decrease it accordingly by taking into account any specified packing density to get a volume that the spheres should take up when packed. This estimate does not account for volume of voids and therefore is a very rough approximation. A volumetric breakdown is determined for each particle size by multiplying the total volume allotted for the spheres by the percent by volume allowed for each aggregate size. These volumetric breakdowns are divided by the volume of an individual particle of the specified size to

achieve a quantity of how many particles is necessary to fill the volume allotted. Adding all these quantities yields a final count of the particles needed to fill the box which when divided by the particles needed of a specific size returns the percent by number of particles required.

Additionally, the spacing between particles is determined as 30% greater than the largest particle diameter which ensures no particles will overlap even after random perturbations occur. The number of particles needed longitudinally (direction of the length of the strap) is approximated as the length of the box divided by the particle spacing. The particles needed horizontally (perpendicular to the strap) is done similarly by taking the width of the box and dividing it by the particle spacing. Then the vertical stack of particles is whatever is remaining to achieve the total number of particles estimate. The percent by number values along with the longitudinal, horizontal, and vertical particle estimates serve as initial guesses for a first particle packing.

The three directional guesses can be further refined by making manual adjustments to the packings until the longitudinal and horizontal directions fit in the box correctly. Entering those corrected values back into the spreadsheet will automatically adjust the vertical direction to the closest value to maintain the same total number of particles.

The spreadsheet is also capable of the reverse functionality similar to what was just discussed. However, it works to estimate the necessary box and strap dimensions provided the user inputs the total number of particles and the percent by numbers for each particle size.

#### Appendix D. Miscellaneous Simulation Results and Notes

Presented below are a select few results from other simulation performed throughout the research that have some significance and could potentially be explored more in-depth or are just interesting notes.

Figure A.12 shows a plot of pullout force versus displacement with varying particle sizes starting at 6 mm and increasing in 6 mm increments up to a maximum of 36 mm. A constant

normal load of 41 kPa was applied for these tests and the strap was smooth, i.e. no ribs. The number of particles used varied from simulation to simulation but rather than keep the particles constant, the same volume was filled.

For the most part, the pullout resistance trends towards roughly 9 kN for all the simulations. However, curiously the 36 mm simulation undershot slightly and the 12 mm simulation overshot slightly. It is possible the volume filled was not perfect but it is also possible that if the pullout continued these may ultimately all resolve around 9 kN.

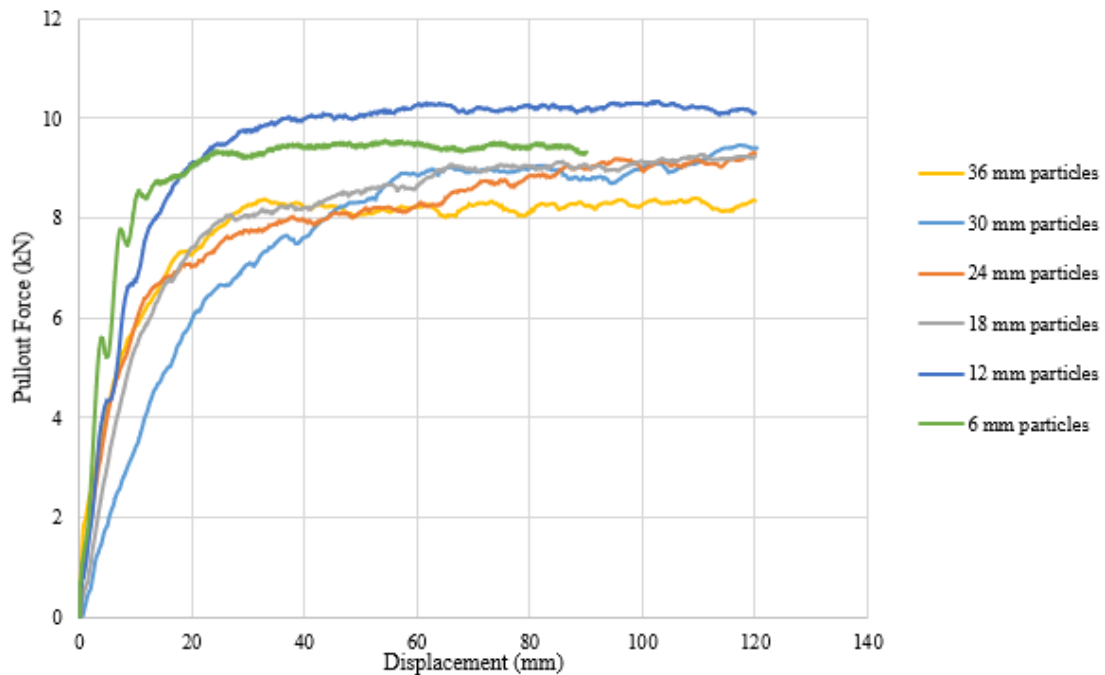


Figure A.12: Plot of pullout force versus displacement while varying particle sizes

Figure A.13 and A.14 show two sets of results investigating the effects of rolling resistance on pullout tests. For each of these, all properties of the simulations were held constant except for either the coefficient of rolling friction,  $\eta_{roll}$ , or the rolling stiffness  $\alpha_{kr}$ . Similar to testing the varying particle sizes, the normal load was 41 kPa and the strap had no ribs. For

reference a run was done where rolling resistance was not used at all and is plotted on both figures.

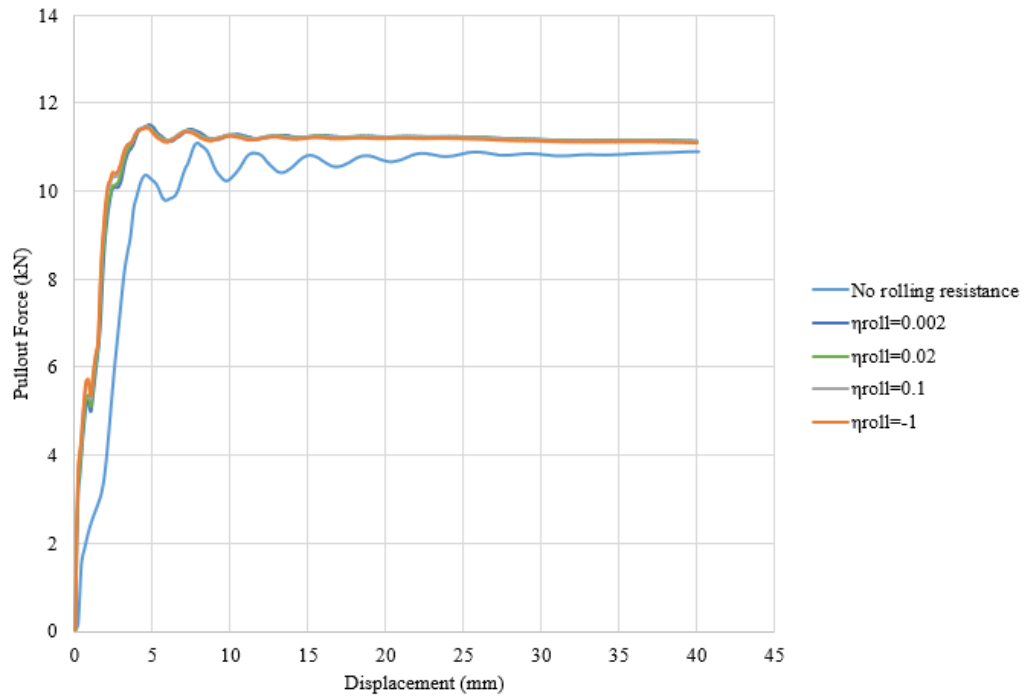


Figure A.13: Varying coefficient of rolling friction,  $\eta_{roll}$ , during a pullout test

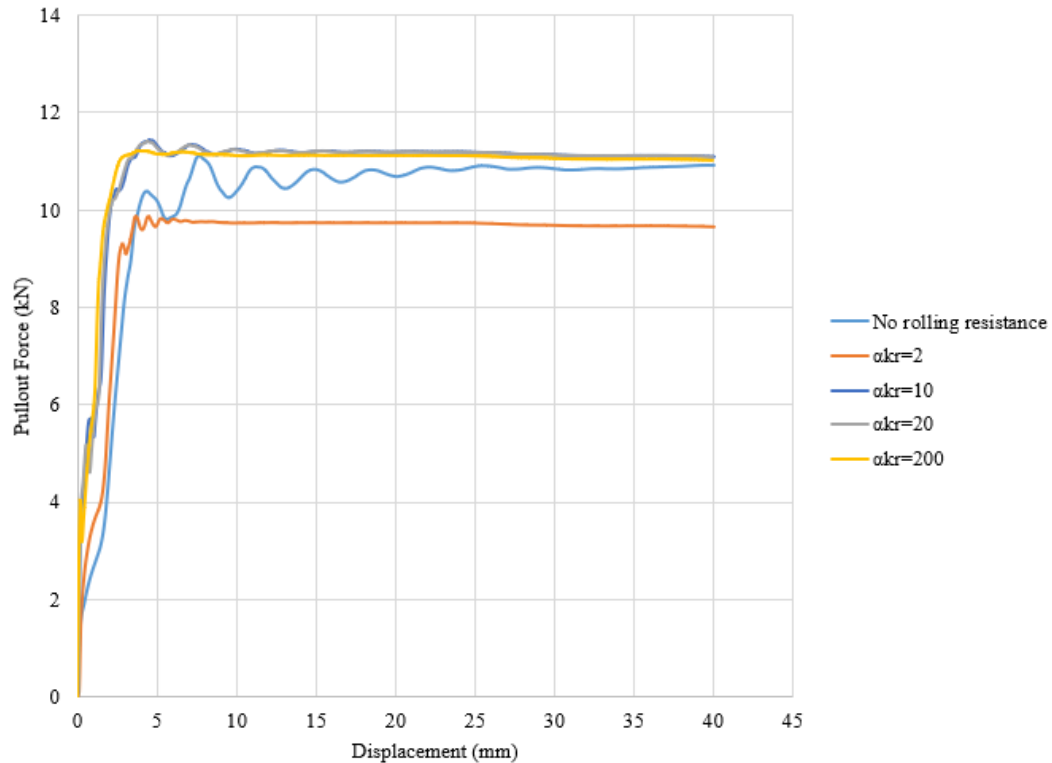


Figure A.14: Varying rolling stiffness,  $\alpha_{kr}$ , during a pullout test

Viewing both of these figures relating to rolling resistance shows that there ultimately was not significant difference in the resulting pullout force from the values tested. The one outlier in all this testing was with the rolling stiffness set at a value of two. Knowing that this specific stiffness value resulted in a lower pullout force it would be worth wild to test stiffness values smaller than two to see if the trend continues. An initial hypothesis was that as the rolling stiffness changed, only the elastic portion of the curve would change however that does not seem to be the case which could be explored more.

Zooming in on plateaued regions of Figure A.13 showed minor differences of up to 200 Newtons which argues the rolling resistance was present but had little effect. Note that these simulations were performed prior to doing the detailed contact tracking study discussed in Appendix A. Therefore, the coefficient of rolling friction values used were most likely not large

enough to introduce a lot of rolling resistance into the system or the majority of motion was already particle sliding. It would be interesting to explore more values for the coefficient of rolling friction to see if any meaningful change can be extrapolated.

Brief viewing of the angular velocity contours for some of these simulations with rolling resistance also revealed more rattling particles compared to simulations without rolling resistance. While an observation, it is important to note that this effect has been seen in other studies, and the increase in rattlers is thought to be an effect of more interlocking particles when under the effects of rolling resistance [17].

At any rate, the rolling resistance was ultimately removed from the simulations because there was no way to define values for the particles that was justifiable for the aggregate being tested. If one were able to accurately set up and characterize rolling resistance, it would be expected to have a greater effect on simulation results.

The following two figures demonstrate the effect that changing the strap size had on pullout results with uniformly sized particles. The simulation results in Figures A.15, A.16, and A.17 are identical except for changes to the strap width and thickness. All were set up to duplicate pullout results with a coefficient of 1.4 from [38]; however, the model was not fine-tuned at that point and strap size was being investigated as to how much of a role it contributed to the pullout force. Each simulation contained 29,700 particles that were 24 mm with a particle friction angle of  $40^\circ$ .

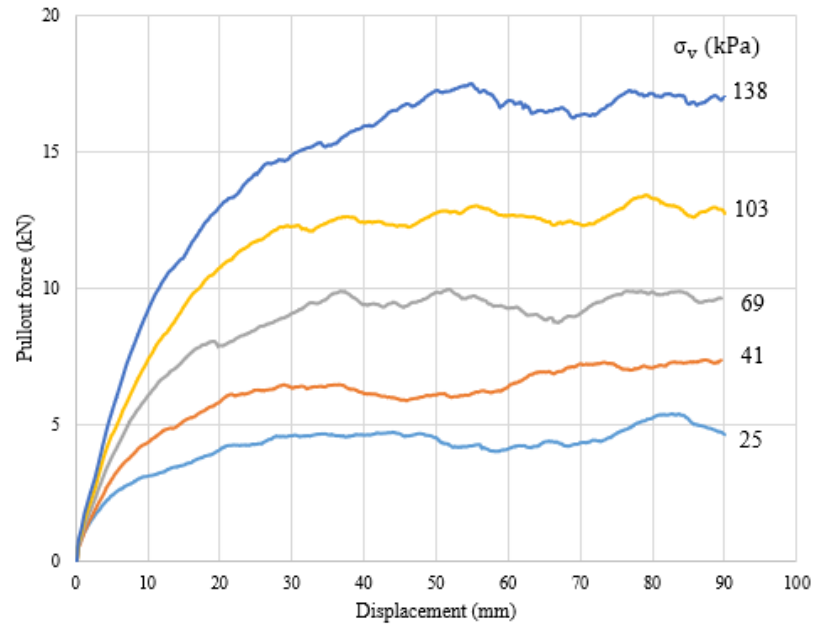


Figure A.15: Pullout force vs displacement when strap size was set to 1.5m x 0.10m x 0.008m (LxWxT)

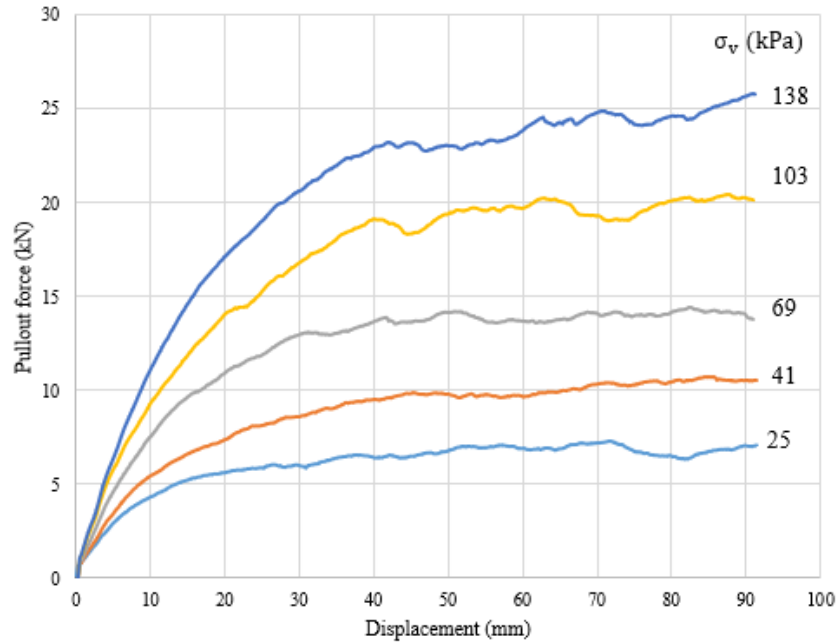


Figure A.16: Pullout force vs displacement when strap size was set to 1.5m x 0.15m x 0.012m (LxWxT)

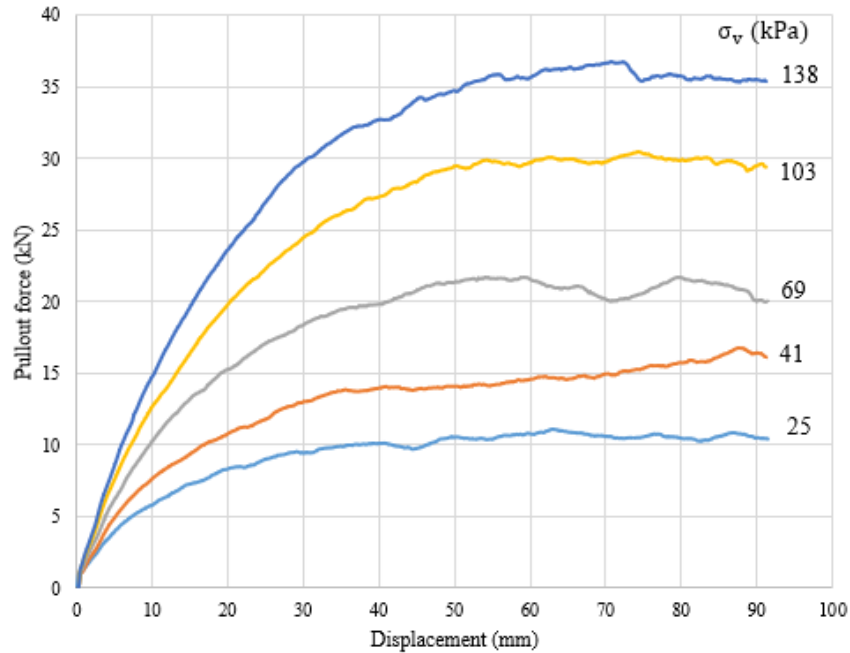


Figure A.17: Pullout force vs displacement when strap size was set to 1.5m x 0.2m x 0.016m (LxWxT)

As was expected, a wider and thicker strap led to higher pullout forces. This higher pullout force was thought to be a result of additional particles being in contact with the strap which therefore applied additional pressure and in turn the strap required a larger force to pullout. All the sets trend linearly with respect to one another, as is shown in Figure A.18. However, the plot shows that the changes in the residual forces tended to get larger as the applied pressure increased (i.e., the slopes of the lines increased).

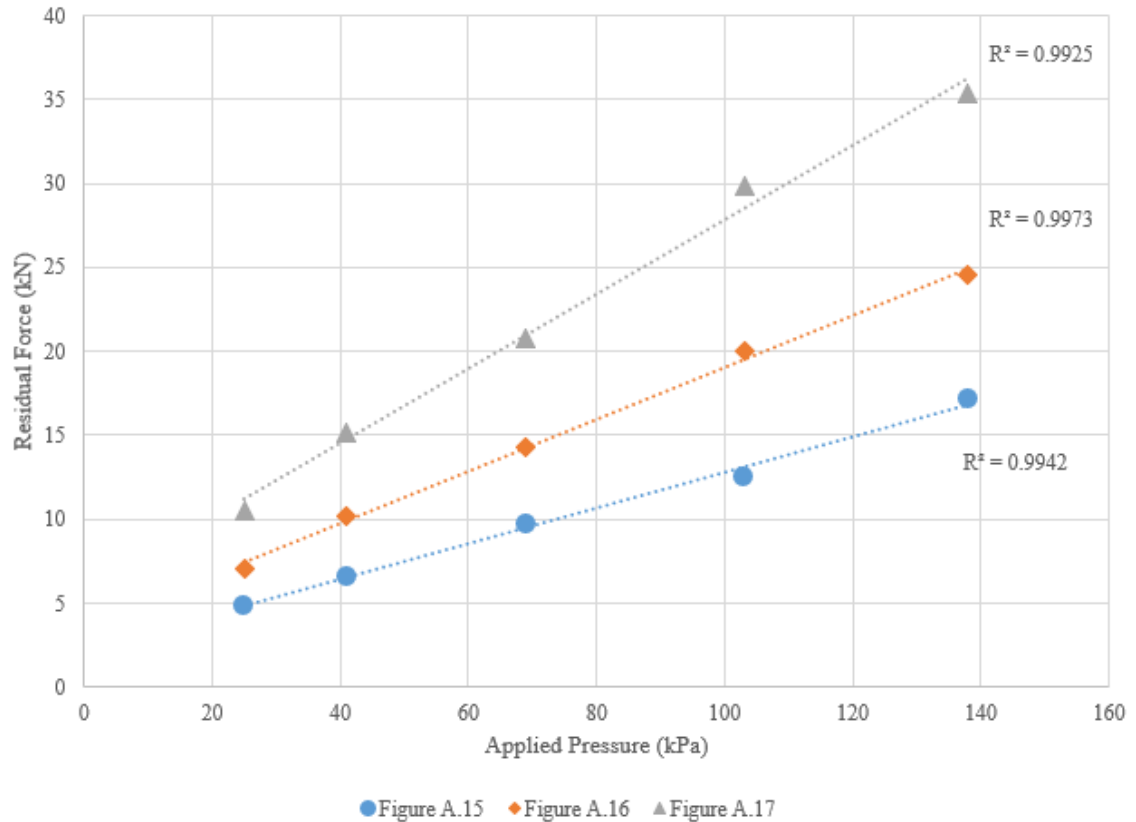


Figure A.18: Residual force vs applied pressure for Figures A.15-A.17

It would be interesting to follow up on these simulations and perform a designed experiment regarding the width and thickness. Ideally this setup would isolate which of these parameters has a larger effect on the pullout resistance or if they contribute about the same amount. This result likely would vary depending on the size of the aggregate relative to the size of the strap. A strap that is equally as thick as it is wide, would contact roughly the same number of particles along the width as it would along the thickness and therefore both would potentially contribute equally to the force. Whereas, in the situation here the width would be suspected to affect the pullout resistance more as it is in contact with a larger number of particles across.

## Appendix E. Notes on Computer Core Usage and Parallel Processing

The majority of the simulations for this research were run using only four cores despite having access to up to twenty most of the time. A benchmark pullout simulation with roughly 30,000 particles was ran multiple times early on in the research with a varying number of cores. The time elapsed for each simulation was tracked and it was determined around four cores was optimal. Figure A.19 shows the increase in simulation time with respect to how many cores were in use.

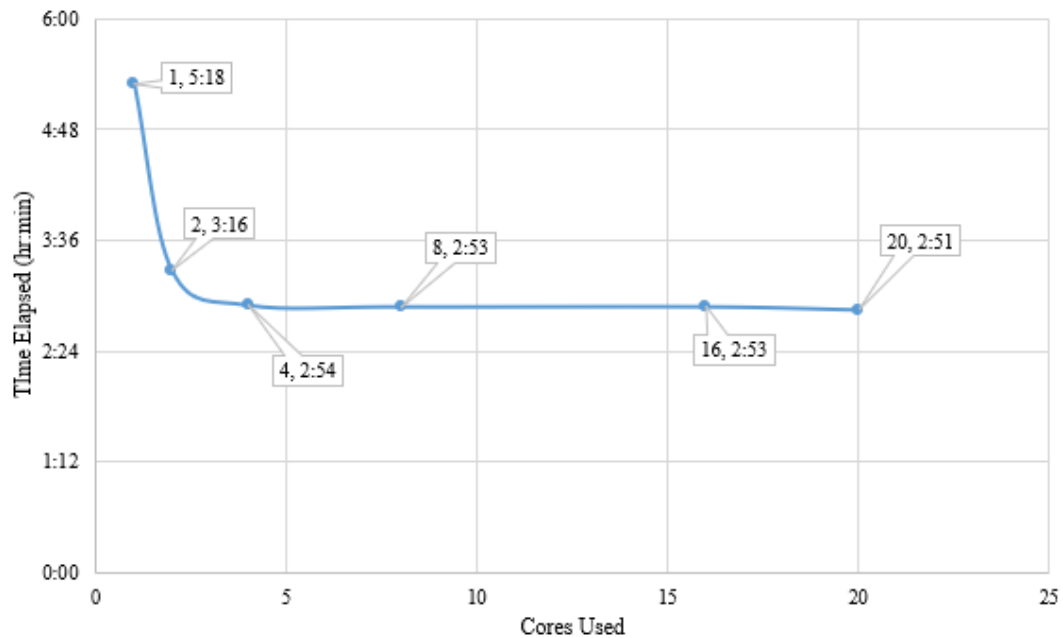


Figure A.19: Simulation time elapsed vs core usage for a 30,000-particle pullout simulation

The diminishing effects of parallel processing in DEM are well-know, although there could have been some additional problems with how the computer interacted with YADE. Core dumps would occur at random points in a simulation and it would happen more often when more cores were assigned to the simulation. This crashing is another reason only four cores were used as requesting additional cores increased the chance for spontaneous core dumps.

To speed up the process five virtual machines were set up with clones of YADE to allow for up to five simulations to be run at the same time. The virtual machines increased the overall output of results significantly and a full set of simulations at the specified normal pressures could be run at the same time.